THE MARTIAN ENVIRONMENT

P.L. Read, M. Collins, S.R. Lewis, F. W. Taylor, O.Talagrand, F. Forget and F. Hourdin

THE MARTIAN ENVIRONMENT

P.L. Read, M. Collins, S.R. Lewis, and F. W. Taylor

Atmospheric, Oceanic and Planetary Physics,

Clarendon Laboratory,

Parks Road,

Oxford,

UK,

OX1 3PU.

Tel: 44 1865 272933

Fax: 44 1865 272923

Email: P.Read1@physics.ox.ac.uk, M.Collins1@physics.ox.ac.uk,

S.Lewis1@physics.ox.ac.uk, F.Taylor1@physics.ox.ac.uk

O.Talagrand, F. Forget and F. Hourdin

Laboratoire de Météorologie Dynamique du CNRS,

Ecole Normale Supérieure,

24 rue Lhomond,

75 231,

Paris Cedex 05,

France.

Tel: 33 1 44 32 22 47

Fax: 33 1 43 36 83 92

Email: talagran@lmd.ens.fr, forget@lmd.ens.fr, hourdin@lmd.ens.fr

Report on the Martian Environment, ESA Environmental Models, WP1.

Contents

1 INTRODUCTION

This report presents the first stage of results of a study of the atmospheric environment on Mars. The purpose of the study is to combine existing knowledge derived from measurements, theoretical studies and numerical general circulation models into a single model which can be used to specify conditions such as temperature, pressure, wind, humidity, and dust loading over a wide altitude range at any location, time of year, and time of day on Mars. This environmental model is intended for use in the design of future missions to land on the surface of Mars, such as the 'InterMarsNet' project being studied by the European Space Agency.

The conditions prevailing in the atmosphere clearly are a major factor to be taken into account in designing hardware which can land safely and then function for an extended period on Mars. Other aspects to be studied with the aid of the model include the accuracy with which a particular design of vehicle can be brought down at a specific landing site, chosen primarily for its scientific interest and relevance to the mission objectives. The model therefore has to include not only the most probable description of the key atmospheric parameters, but also reliable estimates of the uncertainty in, and natural variance of, these quantities.

The following sections contain a review of the existing knowledge of Mars and its atmosphere, and of how this knowledge was acquired. Section 2 provides, by way of introduction, some discussion of the main factors which design engineers need to take into account in planning a mission to land safely and accurately small instrument packages of vehicles onto the surface of Mars. The gross properties of the Martian system are reviewed in Section 3, making appropriate comparisons with the other terrestrial planets, while sections 4-6 review in more detail the surface environment, atmosphere and polar regions respectively. Some background information on model formulation and presentation of outputs is also presented in Section 7 as a basis for the next stage of the study, the production of a new and improved model.

2 SPACECRAFT ENVIRONMENTAL FACTORS

This section discusses environmental factors which may be of importance in planning a spacecraft mission which involves landing on the surface of Mars. These fall into three categories: (1) factors which affect the design of the entry system, such as entry angle and parachute size, etc.; (2) factors which affect the landing itself, such as surface pressure and wind speed; (3) factors which affect the long-term survival of the landers following deployment, and the implementation of the scientific experiments on the surface, such as the diurnal temperature cycle. These are considered in turn in the following sections.

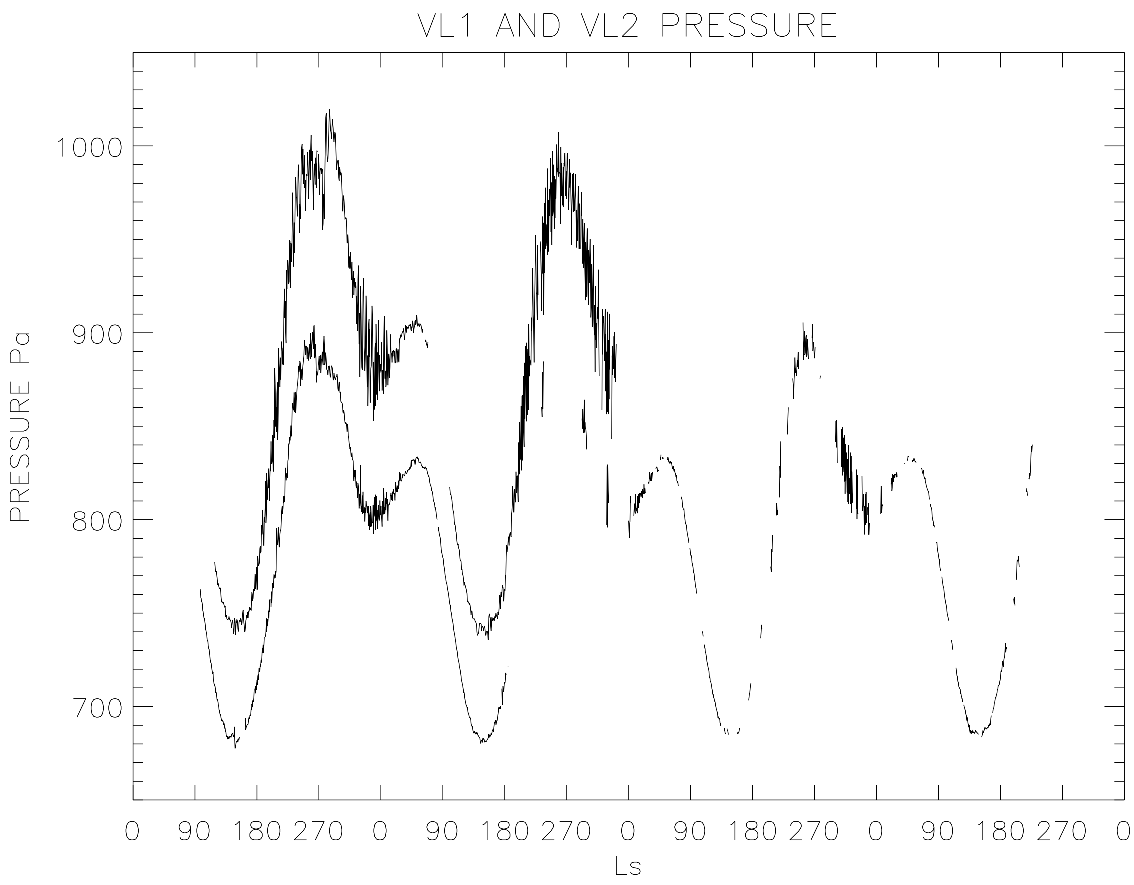

Figure 1: Sol averaged pressure for the Viking Lander Mission.

2.1 ENTRY AND DESCENT PHASE

To perform a detailed entry and descent trajectory analysis will require vertical profiles of atmospheric temperature, pressure and wind as a function of height at all geographical locations under consideration for landing. During the entry, a lander module experiences hypersonic, transonic and subsonic flight, starting out at a velocity likely to be in the range 4 to 9 km s^{-1} (the velcotiy was 4.4 km s^{-1} for the Viking landers). A key parameter in designing the entry trajectory is determining the sonic altitude, or height above the surface where the entry vehicle decelerates through the sound barrier. This is likely to be in the range from 7 to 14 km.

The primary factors controlling behaviour on entry for a given set of conditions are the shape of the module itself (and factors such as its mass distribution) and the design of the parachutes. The former is likely to be a basic sphere-cone configuration with a cone angle in the region of 60°, for maximum drag and high stability against tilting or tumbling during descent. The detailed design of the entry module must also take into account factors such as the heating effects of atmospheric drag, which affects the amount of insulation and ablative material which must be carried, and the constraints imposed by the accommodation available for the landers on the launch and interplanetary cruise vehicles.

The flow field around the module must be known in order to compute the heating rates and the pressure distributions, which are needed to design the heat shield and the structure. In studies carried out for the NASA MESUR project, entry was assumed to commence at a height of 125 km. Three different numerical methods were used to solve the Navier-Stokes equations. In order of increasing complexity and accuracy these were (i) a constant effective specific heat ratio, (ii) atmospheric gases in thermodynamic equilibrium, (iii) finite chemical reaction rates and a non-LTE thermodynamic model with different translational and vibrational temperatures. The three methods yielded significantly different shock-layer temperatures at high speeds, but roughly similar pressure distributions.

Parachute design is likely to use first a drogue and then a main parachute. For Marsnet, the drogue was proposed to be a disc-with-gap design 3.8 m in diameter, deployed at Mach 1.8 when the rate of deceleration is calculated to be about 17.5 m s^{-2}. A cruciform main parachute was to be deployed at around Mach 0.8, sized to achieve a vertical velocity of 20 m s^{-1} at the landing site pressure. The size obviously depends on the site chosen; very high sites (elevation more than about 5 km) such as the tops of volcanoes are excluded as the parachute size required would be prohibitively large.

Studies carried out so far suggest that two of the most important considerations so far as the atmospheric variables are concerned are the wind shear and the presence or absence of dust storm conditions. The former can alter the angle of attack of the probe during descent and tend to destabilise its flight. Dust storms radically alter the characteristics of the atmosphere, including its temperature/pressure profile and wind gust frequency, and the dust itself could damage the module and its equipment and/or the parachute. In particular, landing during or after a major dust storm would result in significant extra ablation of the heat shield during entry. The effect of dust impact on shield materials has been calculated and in one case led to a 30% increase in total shield mass relative to the dust-free entry condition.

2.2 LANDING

The current concept for the InterMarsNet landing system uses parachutes, a surface sensing radar and retro-rockets, similar in concept to the larger Viking landers of 1976. The main parachute is shed some time before landing, and is assumed to be carried away by the wind so that it lands some distance away from the surface station itself. The simplest design of retro-rocket has a fixed total impulse and is ignited at a precalculated height above the ground. However, this presupposes an accurate knowledge of the pressure and height of the landing site, and in practice the terminal velocity of the lander is estimated to be as high as $+10$ m s^{-1} at the end of a burn commenced at a velocity of 40 m s^{-1}. If this is unacceptable then a more complex system in which the rocket thrust is controlled in response to a knowledge of the altitude, descent rate, and horizontal velocity, is required. This in turn requires a more complex radar system, greater computing capability, and actuators to steer the rockets, but a contact velocity of 1 m s^{-1} or less is achievable.

An additional benefit of the more expensive system is that it offers the possibility to reduce the considerable hazard posed by the surface roughness, especially if the probe velocity has a component parallel to the surface. The latter is determined mainly by the wind speed near the ground, and if large represents a risk that the module may overturn or drift sideways into an obstacle. An active landing system can control the horizontal component, also to better than 1 m s^{-1} for moderate wind speeds. If high wind speeds are expected, the system has to be correspondingly more powerful and complex or the risk of landing failure increases.

2.3 SURFACE OPERATION

Once landed, the vehicle will need to survive the ambient conditions, including the large diurnal and seasonal temperature cycle which may well involve frost formation. Windblown dust represents a hazard to the systems on-board. An extreme case which can be imagined is that in which the lander is buried under an accumulation of dust, especially if it lands in a relatively enclosed space of some kind, or on a slope. More probable, and only slightly less disastrous, would be the situation where the solar cell arrays, which may be of the flexible type rolled out on the surface, are covered by enough dust to prevent their proper functioning. Large amounts of airborne dust may also affect the energy falling on the array sufficiently to create a power budget problem. Similar problems may occur near the poles in winter; the southern polar CO_2 ice cap can grow to within 40° of the equator and may bury a lander.

3 GLOBAL CHARACTERISTICS OF MARS

As a prelude to the more detailed discussion of the Martian atmospheric and surface environment, we present in this section a brief review of the main planetary parameters and characteristics of Mars and the other terrestrial planets.

3.1 ORBIT AND PLANETARY PARAMETERS

Mars orbits the sun at a distance of 227.9 million kilometres (c.f. 57.9, 108.2, and 149.6 million km for the other three terrestrial planets, see Table 1). The orbits of Earth and Venus are nearly circular, but those of Mercury and Mars are significantly eccentric. The biggest single factor affecting surface and atmospheric conditions on any planet is the sunfall; Venus receives almost twice as much energy per unit area as Earth and nearly four times as much as Mars. However, by an interesting example of atmospheric feedback processes at work, all three planets have developed reflective cloud coverings, and in the case of the two outermost, reflective ice-covered regions, to such an extent that the solar energy actually absorbed is not very different, with Earth retaining the most and Mars second. It is intriguing to note that the surface conditions on frozen Mars and baking Venus are both sustained by roughly equal amounts of net heating, due entirely to differences in their atmospheres.

Mars is considerably smaller than Venus or Earth, which are of nearly identical size and density, having a diameter a little more than half that of the other two. Concentrating on surface features which have an important effect on the atmosphere, the principal things to note are the extreme topography on Mars with its high volcanic mountains and deep canyons, particularly in relation to its smaller size overall. Olympus Mons, an extinct volcano, is more than three times as tall as Everest, and parts of the Valles Marineris are nearly four times as deep as the Grand Canyon of Arizona. On Mars the pressures and temperatures are too low to sustain liquid water, though there is probably a lot of frozen water in the polar caps and below the surface soil at other latitudes. A particular property of Mars is that the principal constituent of the atmosphere, carbon dioxide, is caused by the low temperatures to condense at the winter pole during the period of perpetual darkness [6, 5.4.2]. Billions of tons of the gas leave the atmosphere as snow in the winter, to evaporate when the spring comes, resulting in a large swing of nearly a third in the mean surface pressure all over the planet. This has a dramatic effect on the general circulation which is as yet little studied in the absence of the necessary comprehensive observations, some of which may be gained from Mars Surveyor, Pathfinder, and other new missions due to launch in the 1990s and early 2000s.

Next to the solar heating, and the degree of availability of large reservoirs of volatiles, the most important atmospheric boundary condition is the rotation rate of the solid planet. Mars and Earth have almost the same period, and hence nearly the same length of day; on Mars the length of day is only about 37 minutes longer than on Earth.

The inclination of the planetary rotation axis, and the eccentricity of the orbit, give rise to the seasons. Mars has a fairly large axial tilt (or 'obliquity') of 24 degrees and enough eccentricity to change the solar constant by as much as 18 % during the year. Earth has almost the same obliquity as Mars and a smaller, but still significant, eccentricity of 0.0167. The year, or time taken to orbit the Sun once, naturally varies with heliocentric distance and is 87.97 (Earth) days for Mercury, 224.7 days for Venus, 365.3 for Earth and 687.0 days for Mars.

3.2 COMPOSITION

The atmospheric composition is not the same on each of the inner planets, nor should we expect it to be. This is likely to be due to a number of factors, such as gradients in the composition of the solar nebula from which the planets condensed, different escape rates for gases leaving the planet as a result of the different rates of heating of the upper atmosphere, the differences in gravitational attraction, and physical and chemical processes which depend directly or indirectly on distance from the Sun and which govern the exchange of material between the atmosphere and the crust; life on the surface of Earth is a special case of this.

It is thought that the primary atmosphere of Mars (i.e. that which formed with the solid bodies themselves) was lost in the distant past and that the present atmospheres of all of the inner planets (Table 2) are secondary, that is to say produced by outgassing from the crust or by influx of cometary and meteoritic material. The commonest gases which might accrue in this way are carbon dioxide, water vapour and nitrogen. The amounts of each, and the admixture of other gases, depends on the initial composition of each planet and its subsequent evolution, particularly its thermal history. Moderately large amounts of some gases, such as argon, are produced by the decay of radioactive materials and form a significant component of the present day atmospheres of Venus, Earth and Mars.

The basis for our current understanding of the composition of the Martian atmosphere comes primarily from the Viking landers, which were equipped with gas chromatographs and mass spectrometers [Owen et al. 1977]. The measured abundances provide a constraint for theoretical studies of the formation and evolution of the atmosphere (for a review, see Pollack and Yung [1980]). Mars has an extremely low abundance of atmospheric water vapour, because of the temperatures which are so low that even saturated air has a low absolute humidity. Again it seems likely that this was not always the case, since many of the surface features on Mars were apparently shaped by liquid water. The low temperatures now prevailing there have locked some of the water permanently in the polar caps and, probably, much of the rest as 'permafrost' below the surface at most other latitudes. Since we cannot measure or even estimate accurately how much water exists as ice on Mars at present, it is not possible to say whether the total budget is anomalous, like that of Venus seems to be. Obtaining measurements of polar and sub-surface water on Mars remains one of the most important objectives for future planetary exploration.

	Mercury	Venus	Earth	Mars
Oribital and Rotational Data				
Mean distance from Sun (km)	5.79×10^7	1.082×10^8	1.496×10^8	2.279×10^8
Eccentricity	0.2056	0.0068	0.0167	0.0934
Obliquity (deg)	0	177	23.45	23.98
Sidereal period (days)	87.97	224.701	365.256	686.980
Rotational period (hours)	1407.5	5832.24	23.9345	24.6229
Solar Day (days)	115.88	117	1	1.0287
Solar Constant (kW m^{-2})	see text	2.62	1.38	0.594
Net heat input (kW m^{-2})	see text	0.367	0.842	0.499
Solid Body Data				
Mass (kg)	3.303×10^{23}	4.870×10^{24}	5.976×10^{24}	6.421×10^{23}
Radius (km)	2439	6051.5	6378 to 6357	3398
Surface Gravity (m s^{-2})	3.70	8.60	9.78	3.72
Atmospheric Data				
Composition	He, Na	See Table 2	See Table 2	See Table 2
Mean molecular weight	-	43.44	28.98 (dry)	43.49
Mean surface temperature (K)	~ 400	730	288	220
Mean surface pressure $10^5(Nm^{-2})$	$< 10^{-12}$	92	1	0.0061
Mass (kg)	-	4.77×10^{20}	5.30×10^{18}	$\sim 10^16$

Table 1: Physical Constants for the Terrestrial Planets

The isotopic ratios of carbon and oxygen are approximately the same on Venus, Mars, and Earth, but different for nitrogen . The ratio of 15N to 14N in the Martian atmosphere is about 1.7 times that on Earth. If it is assumed that the ratio was the same in all of the planets at formation and models are constructed which represent the preferential loss of the lighter isotope from the exosphere, then these require that the nitrogen was initially much more abundant on Mars than it is now. McElroy et al. [1977] find that the partial pressure of nitrogen on Mars must have been at least 2, and perhaps as much as 30 hPa; 20 to 300 times as much as it is now. Owen et al. [1977] independently estimated that nitrogen and carbon dioxide were at one time at least 10 and 20 times more abundant, respectively, and that the initial outgassing of water was enough to produce a layer about 10 m deep on Mars. As noted above, some or all of this may still be present as ice and permafrost.

	Venus	**Earth**	**Mars**
Carbon dioxide	.96	.0003	.95
Nitrogen	.035	.770	.027
Argon	.00007	.0093	0.16
Water Vapour	$\sim$.0.001	$\sim$.01	$\sim$.0003
Oxygen	.21	.0013	~ 0
Sulphur dioxide	.00015	.2 ppb	~ 0
Carbon monoxide	.00004	.12 ppm	.0007
Neon	5 ppm	18 pmm	2.5 ppm

Table 2: Composition of the Terrestrial Plane Atmospheres: Values are given as fractional abundances by mass or parts per million (ppm)

	Venus	**Earth**	**Mars**
Fractional coverage	1.00	0.40	0.05 (cloud) 0-1.0 (dust)
Typical optical depth	25-40	5-7	0.2-6 (dust)
Composition	H_2SO_4, H_2O	H_2O	Magnetite etc. (dust) H_2O, CO_2
Number density (cm^{-3})			
-liquid	50-300	100-1000	
-solid	0-50	0.1-50	30-1000
Typical mass loading (g m^{-3})	0.01-0.1	0.1-10	.0002-0.1
Main production process	chemistry	condensation	windblown (dust)
Equivalent depth (mm)	0.1-0.2	0.03-0.05	1-100
Effective radius (μm)	2-4	10	0.4-2.5 (dust)
Main forms	Stratiform	stratiform, cumulus	stratiform, mixed (dust)
Temporal variability	slight (haze) high (deep)	high	high

Table 3: Properties of clouds and dust in the terrestrial planet atmospheres. The equivalent depth is the estimated thickness of the cloud material if it were deposited on the surface. The effective radius is the radius of the spherical particles having most nearly the same scattering properties as the cloud at visible wavelengths. After Esposito et al., 1983, with changes and additions.

4 SURFACE PROPERTIES

In this section the surface of Mars is reviewed, with two main goals : namely, its influence on (i) climate and large-scale atmospheric circulation, and (b) on local atmospheric conditions for small lander packages and probes.

4.1 TOPOGRAPHY

4.1.1 Definition of Topographic Heights

The Martian topography (or, in meteorological terminology, the *orography*) is one of the most impressive feature of the planet Mars. It shows a marked north-south asymmetry, the heavily cratered southern hemisphere being much lower on average relative to the mean geoid than the younger northern hemisphere. The Tharsis plateau dominates the surrounding reference surface, by more than 8 km, and extends over about one fourth of the longitudes in equatorial regions. The largest volcanoes are particularly impressive, culminating in altitudes of up to 25 km. The huge canyon Valles Marineris is more than 4000 km long and about 500 km wide.

The elevations are referenced to the zero elevation reference surface as outlined in Wu [1981]. This is a gravity level surface described in terms of spherical harmonics of fourth degree and fourth order combined with a 610 Pa surface with a mean radius of 33.82 km.

4.1.2 Three Different Datasets

Although the main features of the Martian orography have been extensively surveyed, due in large part to the Viking orbiter cameras, the accurate determination of the Martian orography is still remarkably controversial. Three datasets representing the surface topography are currently available:

Consortium : The first orographic dataset (Fig. 2) was derived from the Mariner 9 radio occultations and gravity field measurements [Christensen 1975, Lindal et al. 1979]. It has a theoretical accuracy of about 1 km relative to the mean geoid, and a reasonable horizontal resolution. Its main weakness is absence of coverage of the polar regions.

Digital Terrain Model or DTM: was derived completely independently of the Consortium dataset by digitizing contour levels of a map which was constructed using a variety of data, including the stereographic imaging of the surface by the Viking orbiters (JPL, personal communication). Although this dataset accounts for very fine structures not visible in the Consortium dataset, it seems to suffer from substantial biaises on large scales. For instance, the location of the landing site of Viking 2 in the

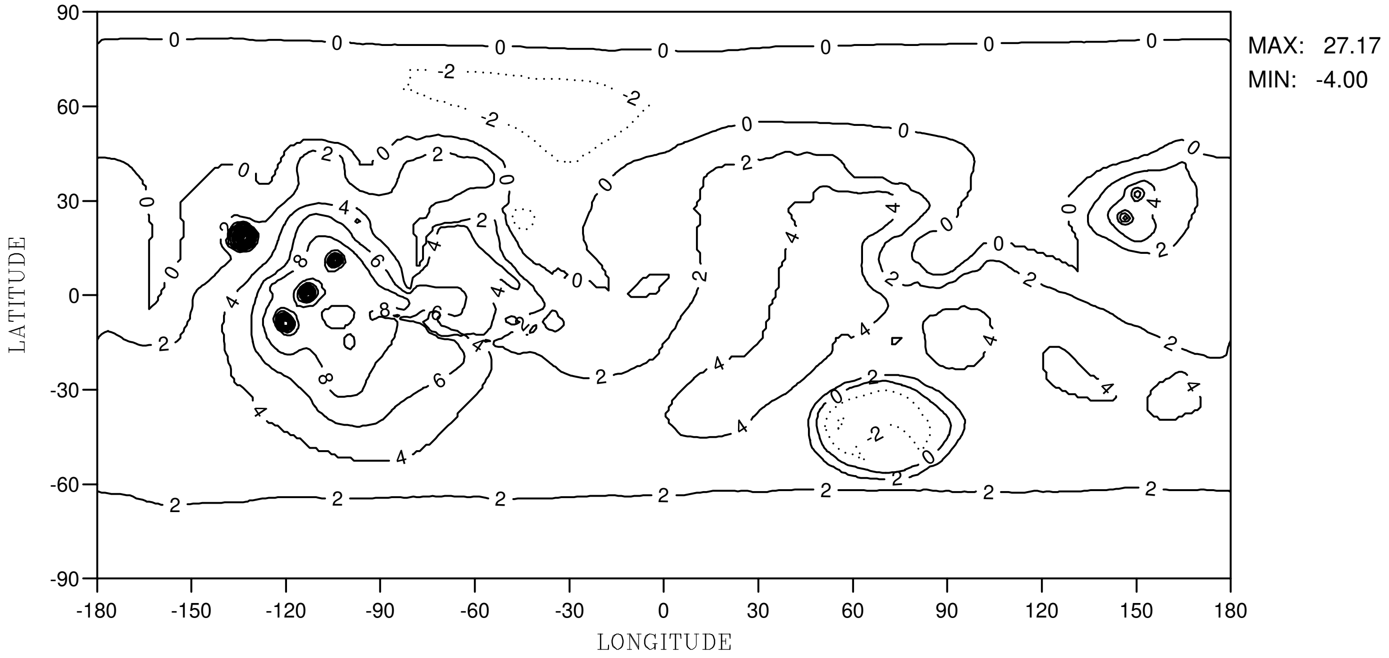

Figure 2: The surface altitude of Mars (in km) based on the Consortium dataset.

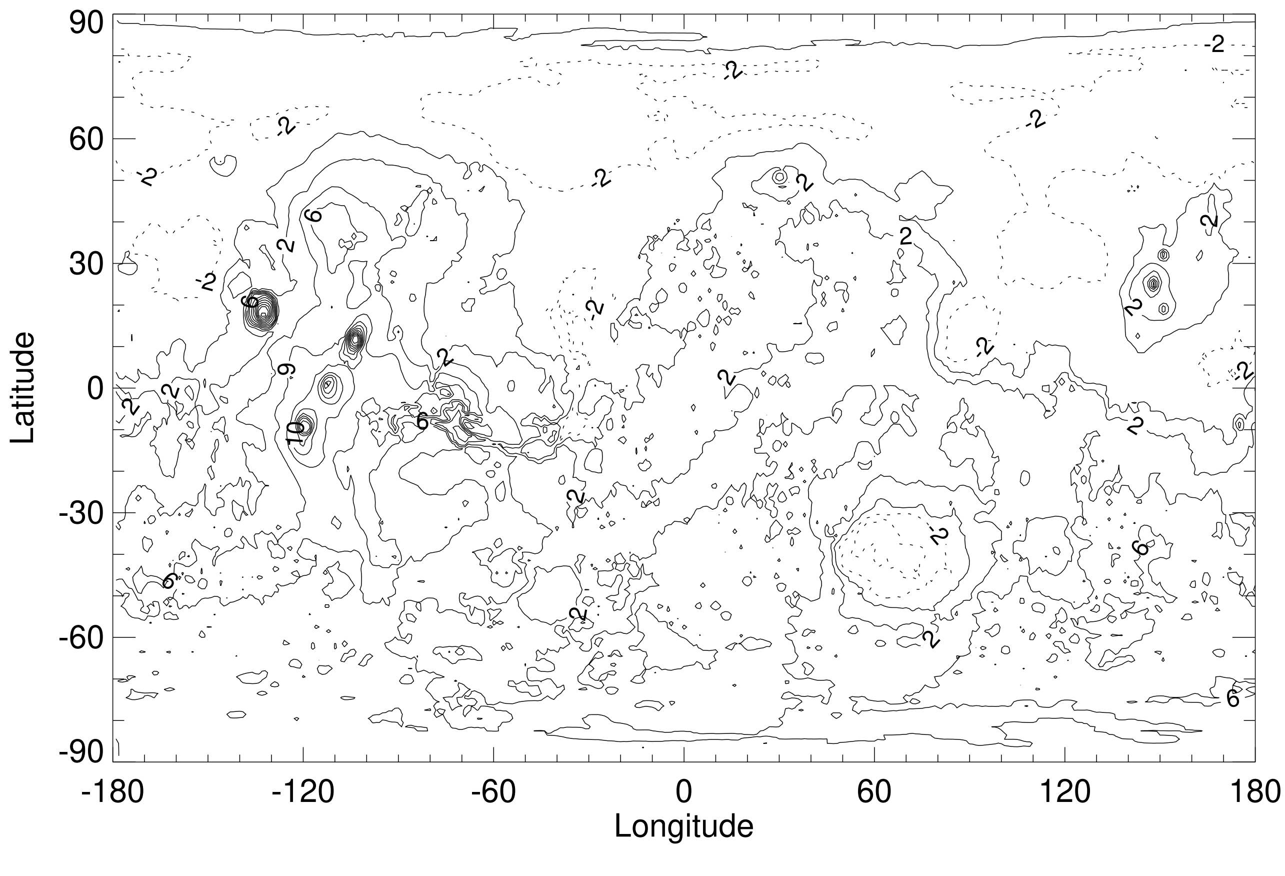

Figure 3: The surface altitude of Mars (in km) based on DTM dataset.

Consortium TOPOGRAPHY

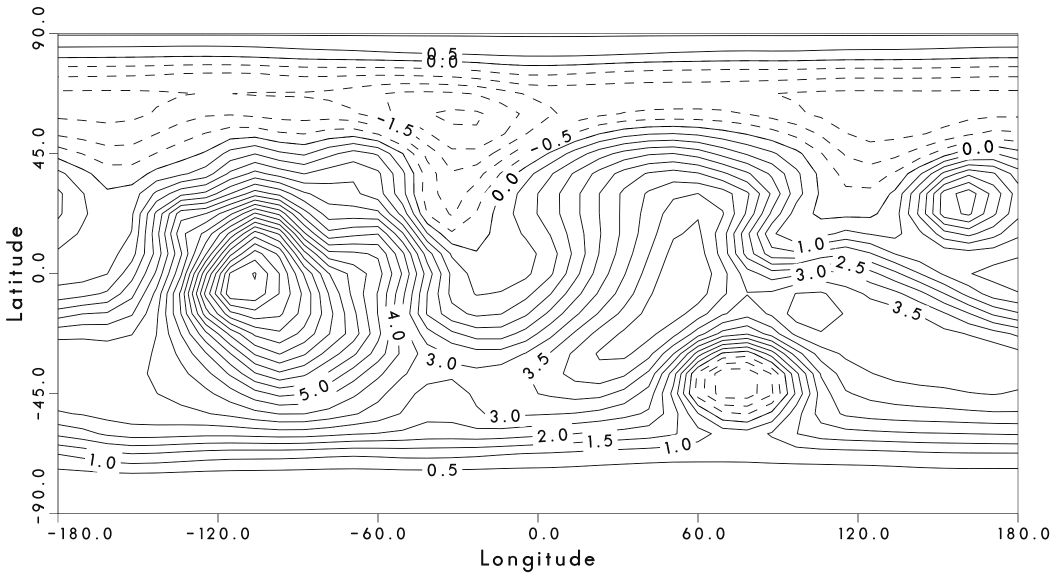

DTM TOPOGRAPHY

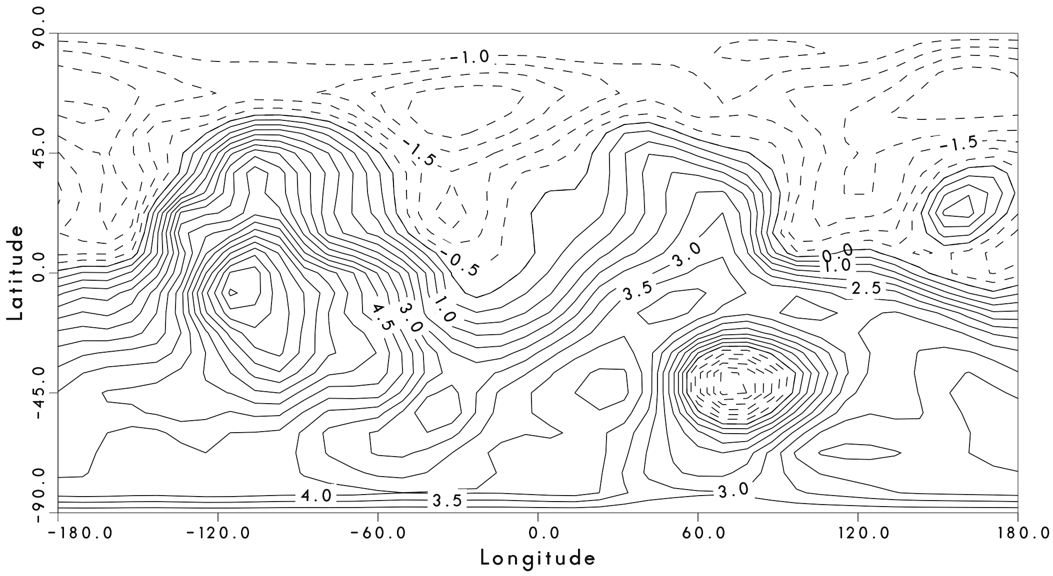

Zuber-Smith TOPOGRAPHY (5X5)

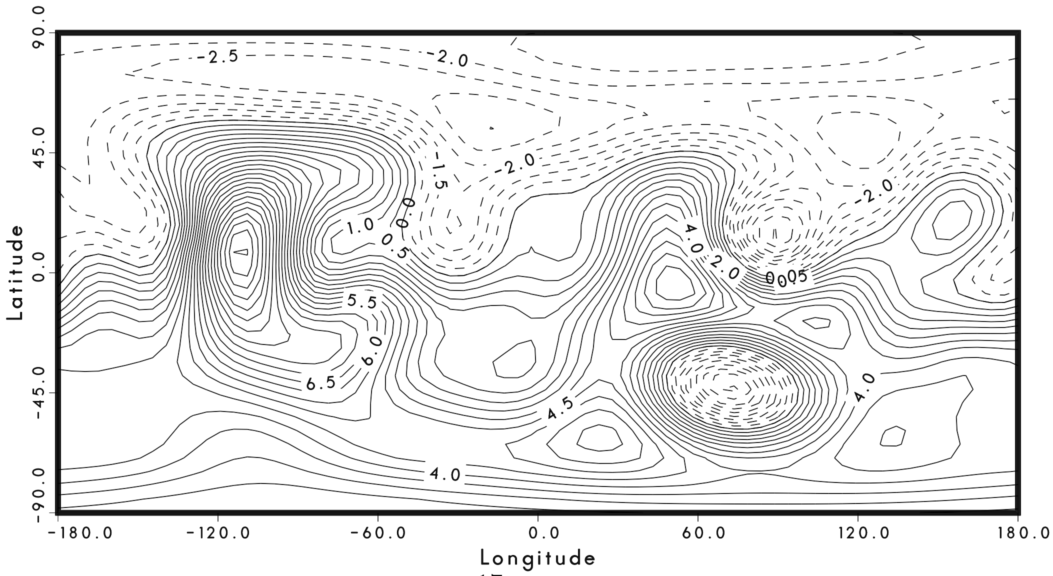

DTM is at a higher altitude than that of Viking 1, although Viking 2 is generally believed to lie about 1 km below Viking 1 from the mean pressure differences between the two sites.

Zuber-Smith : The most recent dataset was constructed by using only the Viking occultations and the estimated altitude difference between the two Viking landing sites. This data has a very low horizontal resolution, however.

From these descriptions, it would appear that none of the current orographic datasets is well suited for climate simulations (see the large differences between them in Fig. 4). The consortium orography is perhaps the best choice to date, except for the polar regions. In fact, the temperature above the polar caps derived from IRTM observations by Forget et al. [1995] indicates that recent estimates of the orography of the polar regions could be strongly underestimated), particularly in the southern hemisphere (above the icy caps, the temperature is directly related to pressure because of the solid-vapor phase equilibrium).

To conclude, although a number of data sources provide some direct information on the orography of Mars, none of the available datasets have so far made use of all those observations jointly. The construction of such a dataset would be a real improvement for the simulation of the Martian climate.

4.2 ALBEDO AND THERMAL INERTIA

The two main characteristics of the surface required for climate model studies are the variations of the visible albedo and thermal inertia. Surface albedo is a key parameter for climate, especially on Mars, where a large part of the insolation directly reaches the surface. It is known, for instance, that thermal gradients resulting from albedo contrasts can produce significant local circulations analogous to 'sea breeze' circulations on Earth [Siili 1994]. The thermal inertia of the surface is defined as $I = \sqrt{\lambda C}$ (where λ is the thermal conductivity of the soil, and C its volumetric specific heat), and characterizes the efficiency of the response in the temperature of the surface to an imbalance between the net surface atmospheric fluxes of heat and those due to conduction in the underlying soil.

Both parameters have been extensively mapped on Mars, largely based on the results of the Viking IRTM measurements which included, in addition to the infrared channels, a bolometric visible channel. The albedo was recovered directly from the visible observations, whereas the thermal inertia was indirectly retrieved by fitting models of the diurnal surface temperature variations to observations. Early studies concentrated on the low and middle latitudes [Kieffer et al. 1977, Palluconi and Kieffer 1981, Pleskot and Miner 1982], but the mapping was later extended to cover the polar latitudes [Paige et al. 1994, Paige and Keegan 1994]. The complete datasets (which form part of the DTM) are shown in Fig. 5. Both albedo and thermal inertia show strong spatial variations, ranging from 0.1 to 0.32 with a mean value of about 0.25 for the albedo, and 100 to 550 J m^{-2} $s^{-1/2}$ K^{-1} for thermal inertia.

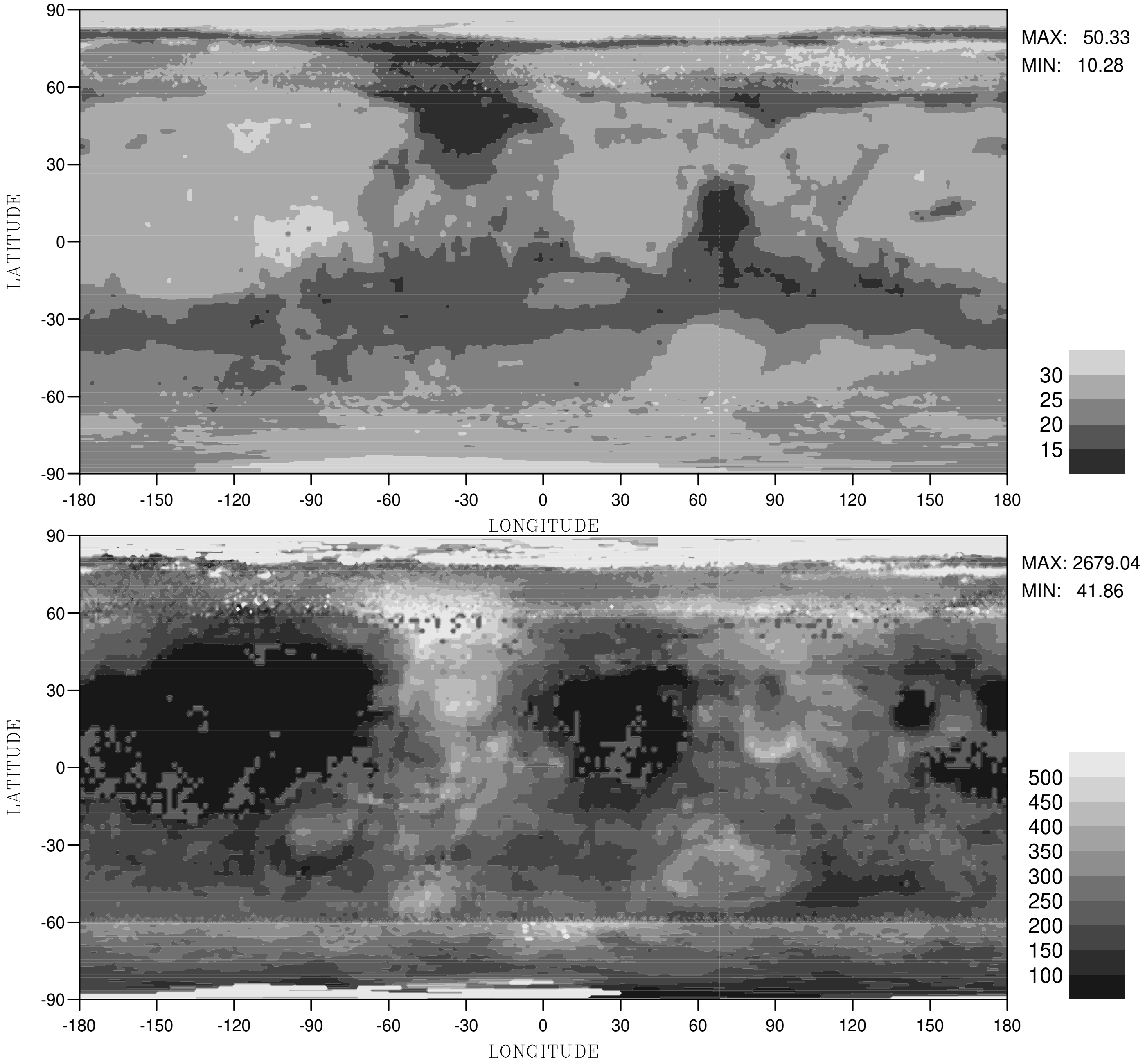

Figure 5: Visible bolometric albedo (%) and thermal inertia (J m^{-2} $s^{-1/2}$ K^{-1}) of the Martian surface. See text for references.

More recent studies have focussed on several weaknesses in the assumptions of the models used to retrieved the thermal inertia. In particular, in preliminary studies the atmospheric downward infrared (?) flux was fixed arbitrarily to 2% of the insolation. By using more sophisticated models which include explicit representation of radiative transfer in the atmosphere (with dust), Haberle and Jakosky [1991] have deduced that the true thermal inertias should be larger by about 50 J m^{-2} $s^{-1/2}$ K^{-1} on average.

It is important to note that, in these maps of albedo and thermal inertia, all the properties have been derived for the Martian surface when it is not covered by CO_2 ice. The radiative properties of CO_2 ices are presented extensively in an independent part of the review (6. Note also that the emissivity of the surface in the thermal range is an additional important parameter for radiative calculations. Thermal emissivity in general is a very difficult parameter to retrieve. Santee and Crisp [1993], however, claim that infrared temperature retrievals lead to a better fit with an assumed thermal emissivity of 0.95 for the bare soil.

4.3 SURFACE "ROUGHNESS" AND ROCK ABUNDANCE

A knowledge of the abundance of rocks and boulders at the surface is, of course, crucial for the safety of a landing on the planet. However, a comprehensive discussion of that subject lies well beyond the scope of the present review. Rock abundance also has a significant climatic impact, however, since it directly determines the surface roughness, and hence the character of the interaction and coupling between the atmosphere and surface.

Except at the Viking sites, there are only two sources of information on the abundance of rocks and the roughness of the surface. The first set of information comes once again from IRTM. Christensen [1986] have estimated that the entire Martian surface is covered by a 1 m thick layer of dust, with a rocky abundance which is never zero, but in which rocks and boulders are found with a mean areal coverage of about 6% and whose abundance never exceeds $30-35\%$. All this is extensively reviewed by Christensen and Moore [1992]. The other major source of information on the surface roughness is provided by Earth-based radar observations. This topic is reviewed by Simpson et al. [1992].

The derivation of a surface drag coefficient deduced from the available data on the rock abundance would be an interesting and useful enhancement for a Martian climate model, even if it turns out that this coefficient does not affect too strongly the atmospheric circulation Hourdin and Talagrand [1994].

4.4 CHEMICAL PROPERTIES OF SURFACE MATERIALS

The primary goal of the chemical analysis experiments performed by the Viking landers was to look for the possible existence of life. Although chemical activity was observed, no organic materials were found. This has been interpreted to result from the presence of oxidants in the Martian soil [Klein 1978 1979]. Suggestions have been made that these oxidants could be produced, at least in part, by the action of ultra-violet radiation [Chun et al. 1978, Oro and Holzer 1979].

4.5 DIELECTRIC CONSTANTS

Values of dielectric constants averaged over large areas ($\sim$ 600 km) at low latitudes can be estimated from reflectivity measurements performed with Earth-based radars. This gives, at 12.6-cm wavelength, an overall average dielectric constant of the Martian surface of 3.0, but with considerable spatial variations (from about 2.3 to about 7) [Downs et al. 1973 1975]. Tang et al. [1977] have used the lander-orbiter relay links in order to obtain more local measurements (on scales $\sim$ 10m) of the dielectric constant at the Viking lander sites. This has given a value of 3.3 ($\pm$ 0.7), in agreement with the value of 3.0 obtained for the same general area from terrestrial measurements. Local measurements at the VL-2 site (inaccessible to terrestrial-based radars) cover too wide a range to be considered as providing useful information. Under the assumption that Martian soil is derived from basaltic rocks with specified properties, Moore et al. [1987] have used the Rayleigh mixing formula Campbell and Ulrichs [1969] for relating the dielectric constant of the soil to its bulk density. For the VL-1 landing site, the abovementioned values of the dielectric constant and the independently measured bulk densities are in agreement with the Rayleigh mixing formula. For the VL-2 site, the measured bulk densities lead to a value of 3.2 for the dielectric constant, slightly smaller than the value at VL-1.

5 ATMOSPHERIC PROPERTIES

In this section we review current knowledge of various aspects of the Martian atmosphere, including its vertical temperature structure, circulation, and various physical processes such as radiative transfer, boundary layer effects and clouds.

5.1 STRUCTURE

In this first subsection, we consider the processes which determine the mean vertical structure of the Martian atmosphere.

5.1.1 Temperature structure

Significant amounts of solar energy reach the ground on all of the terrestrial planets, even for Venus with its thick cloud cover. The basic process whereby short-wavelength solar radiation penetrates lower atmospheres

Figure 6: Mean temperature retreived from Mariner 9 IRIS observations. The period, $L_s = 43{-}54$ correponds to the northern mid-spring. At that time, the polar cap extends from the south pole up to about 60S.

more easily than the longer thermal wavelengths is known as the greenhouse effect, and its result is to raise the surface temperature significantly above that which would apply on an airless planet. The effect is particularly extreme for Venus, where the surface temperature must rise to 730 K in order to force enough infrared cooling to balance the incoming sunlight, about 500K higher than an airless body with the same albedo and heliocentric distance. The corresponding values for Earth and Mars are $\sim$ 40 K and $\sim$ 10 K respectively. Early attempts to compute model temperatures in a Martian pure CO_2 atmosphere failed to give the correct solution because the important contribution of airborne dust had been omitted.

The thermospheres of Venus and Mars are cooler than that of the Earth, because of the greater abundance of carbon dioxide in the former, which is very efficient at radiating heat to space. Above altitudes of about 150 km, the temperature on these two planets is approximately constant with height on the dayside at about 300K.

5.1.2 The observed thermal structure

There are essentially four types of information available on the thermal structure of the Martian atmosphere,each of which provides very different spatial and temporal coverage.

In-situ measurements by the instrument aboard the Viking landers give a fine description of the vertical structure, but at two points of the planet only and for a particular date and time [Seiff and Kirk 1977, Seiff 1982].

Radio-occultations provide very good vertical resolution (about 1 km) at a somewhat larger number of locations. Mars 2, 3 and 5 and Mariner 9 and Viking orbiter conducted such observations but no real synthesis, usable for atmospheric purposes, seem to have been carried out until now (see e. g.Lindal et al. [1979]for the Viking radio-occultations.

The Infrared Interferometer Spectrometer (IRIS) aboard Mariner 9 produced the most useful dataset on the atmospheric structure, since it combined substantial spatial and time coverage (21,000 spectra over the whole duration of the mission) with a rather fine spectral resolution in the CO_2 15-μm band giving access to the vertical thermal structure up to about altitudes of 45 km with a one-scale-height vertical resolution [Hanel et al. 1972]. Inversion of the IRIS observations in a season corresponding to northern spring is shown in Fig. 6.

The InfraRed Thermal Mapper (IRTM) aboard the Viking orbiters provided the best overall spatial coverage (the whole of the planet was covered during a period of almost two martian years), but in only five broad-band infrared channels centered at 7, 9, 11, 15 and 20 μm [Kieffer et al. 1977]. Four of those five channels were essentially insensitive to the molecular absorption by the atmosphere, and thus provided a direct signature of the emission by the surface. Only the 15 μm channel gave any information on the mean atmospheric temperature, covering the 20-35 km altitude range [Martin 1981, see e. g.,]. The four other channels, however, also contain useful information on the dust amount in the atmosphere Martin [1981] and on the possible presence of snow in the atmosphere or on the surface during the polar night Forget and Pollack [1995].

Because the atmosphere is thin, and because the thermal inertia of the Martian surface is small (a major difference with Earth comes from the very large thermal inertia of the oceans on the latter), the surface temperature is never usually very far from radiative equilibrium with the incoming solar radiation. In particular around the solstices, when the diurnally-averaged insolation is at a maximum on the pole of the summer hemisphere, this pole also corresponds to the maximum temperature. The latitudinal temperature gradients in the summer hemisphere are rather weak, as may be seen in Fig. 6. In the polar night, the temperature falls to values around the condensation temperature of carbon dioxide, which is about 145 K for the typical pressure at the martian surface in the polar regions. Between the summer hemisphere and the polar night, there is a region of strong latitudinal temperature gradient.

In the summer hemisphere, the temperature decreases slowly in the first 40 km reaching a value of about 160 K (see Figs. 7 and 6). Above that height, the atmosphere probed by the Viking landers exhibits a constant temperature with a large-amplitude wave superimposed (not included in the standard profile shown in Fig. 7). Note that there is no equivalent to the Earth's stratopshere where the heating by the ozone layer produces a warm atmospheric layer above the tropopause.

In the winter hemisphere, some strong temperature inversions have been observed both by the IRTM 15-μm temperature and Viking radio-occultation measurements. The latter are consistent with an atmosphere which is warmer than the underlying icy surface, the temperature of which is regulated by the vapor-solid phase equilibrium. A typical spring polar profile showing a strong inversion, constructed by Lindal et al. [1979], is shown in Fig 7.

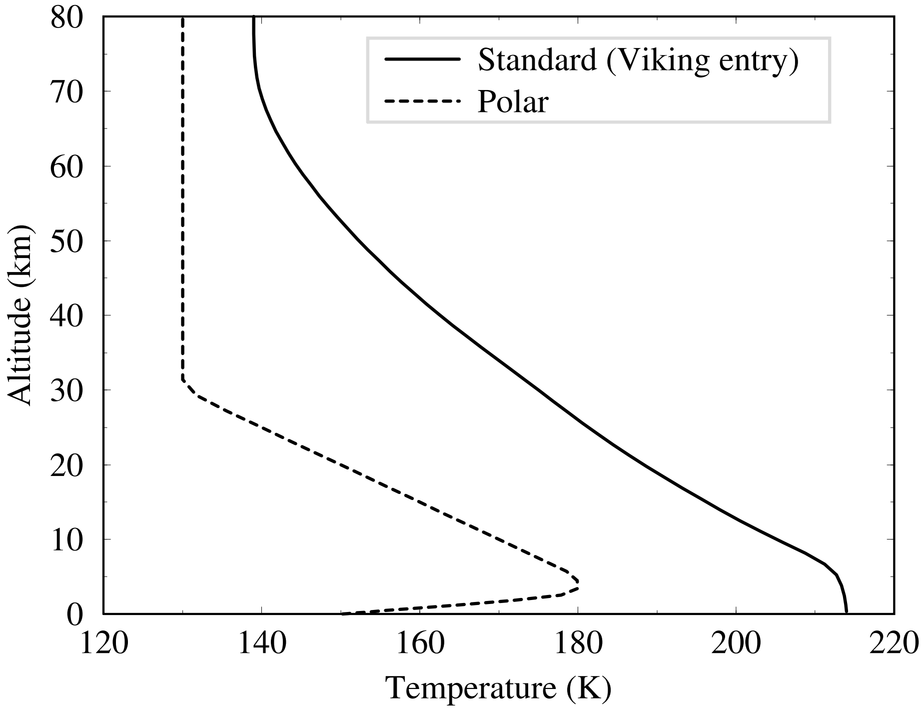

Figure 7: Two typical synthetic temperature profiles. Which were used by Hourdin (1992) to study radiative transfer on Mars.

The low thermal inertia of the martian surface and atmosphere is also responsible for a strong diurnal cycle of the surface and near-surface temperature. This large diurnal cycle was observed at the Viking sites (where, for instance, the peak-to-peak diurnal amplitude was of the order of 80 K for the surface and about 50 K for the air at 1.6 m above the surface at the begining of the Viking 1 mission) and in the IRTM and IRIS observations. The heating of the surface during the day produces strong convection which extends up to altitudes of a few kilometers, whereas the cooling of the surface during the night produces a very sharp temperature inversion close to the ground.

5.1.3 CLOUDS

Convective activity in the tropospheres of the planets raises moist air from near the warm surfaces to cooler upper levels, where the volatile content can condense to form clouds. On Mars, clouds occur much less frequently than on the Earth and the mean cover is only a few percent. Nevertheless, analogues to all the common terrestrial types occur on occasion. Martian convective clouds tend to occur near local noon over high ground, where the surface is strongly heated. The atmosphere, heated from below, can become unstable; the resulting clouds have been observed at heights from 4 to 6 km above the surface.

Hazes of ice crystals are seen over the Martian poles in autumn and spring. The autumn 'polar hood' in the north is particularly pervasive and extends as far south as 50oN . It clears in early winter as the crystals precipitate out of the atmosphere. Orographic clouds form both as extensive layers over large-scale topography and as lee clouds behind tall features such as the giant volcanoes. The latter frequently show the structure of buoyancy waves caused initially by the cooling of the air mass as it rises to cross the obstacle; it then falls on the other side, warms by adiabatic compression, and begins to rise again. Moisture tends to condense at the highest excursions;the train of clouds thus formed can extend for hundreds of kilometres.

Low-level hazes of condensed water vapour are common on Mars, especially at dawn and dusk and over low areas. These are produced by the rapid cooling of the surface as the solar heating drops off towards nightfall; they can persist all night and several hours into the morning before dispersing, often accompanied by a light surface frost. Although most of the clouds on Mars are composed of water, at times CO2 crystals are also present. It is not always possible to say unambiguously whether a cloud is H2O, CO2 or both, at times or places where the local conditions are cold enough to permit CO2 condensation. The high hazes (up to 50 km altitude) which can be seen in many photographs of the limb of Mars, and certain other wispy clouds which apparently form at high altitudes at night, vanishing quickly after daybreak, are most probably CO2.

In energy balance and hence climatological terms, it is not clouds which are most important on Mars - unlike Venus and Earth - but rather airborne dust. The atmosphere appears always to contain a considerable load of dust, mixed through the lower 20 or 30 km. The lowest value of the vertical optical depth observed by either of the Viking landers during their first year of operation was 0.18 at one site and 0.36 at the other [Pollack et al. 1977]. This amount of dust is enough to modify the atmosphere temperature profile substantially, and hence to affect the dynamics. Under certain circumstances, these modifications can be such that the resultant winds raise more dust, leading eventually to a dust storm which can blanket the entire planet. Major storms tend to occur annually, when Mars is close to perihelion, and to originate in approximately the same part of the southern hemisphere. A model for their formation has been proposed by Leovy and Zurek [1979].

5.2 RADIATIVE TRANSFER IN THE MARTIAN ATMOSPHERE

Direct heating and cooling by infrared and visible radiation is by far the most important source of diabatic heating in the Martian atmosphere. CO_2, which represents about 95% of the mass of the Martian atmosphere, is the most important gaseous molecular absorber by a large factor (although dust is even significant at visible wavelengths; see below). Its total column abundance is of the order of 150-200 kg m^{-2} (around 30 times that on Earth). The second but much more variable component is dust, which has been observed in significant amounts at all latitudes and seasons during various spacecraft missions [see the climatology by , Martin 1986, constructed from the IRTM measurements]. Other radiatively active species of possible significance considered in this review include CO_2 and H_2O ice clouds, water vapor and ozone.

5.2.1 CO_2

CO_2 is an absorber in both the visible region, through absorption in its near infrared bands, and in the thermal infrared in the 15-μm vibrational band. The absorption by the near infrared bands reduces the incoming surface flux by less than 1% Savijärvi [1991], however, and this generally negligible compared to the absorption by atmospheric dust, even for relatively clear conditions.

The most important contribution of CO_2 gas to radiative transfer in the Martian atmosphere is associated with the emission and absorption of thermal radiation by the very strong 15-μm vibrational band. Radiative transfer in the CO_2 15-μm band has been investigated by a number of authors using a variety of more or less sophisticated band models [Gierasch and Goody 1968, see e. g.,]. A brief review is given by Zurek et al. [1992]. Although non-LTE effects should become apparent above 50 km altitude, where the frequency of collisions decreases, Bougher and Dickinson [1988] have shown that it can, in fact, be neglected up to altitudes around 90 km, due to the strong opacity of the band. The Doppler effect should also be taken into account, since the Doppler broadening of the lines becomes larger than the Lorentzian width due to collisions at pressures around 5 hPa. However, because of the saturation of the Doppler core of the lines, this effect can also be neglected up to about 50 km for the computation of fluxes and cooling rates in the CO_2 15-μm band [Hourdin 1992].

Two recent systematic studies must be mentioned here. First Savijärvi [1991] tested a series of published emissivity or band models for the representation of the CO_2 15-μm band on standard and isothermal profiles of the Martian atmosphere. These calculations did not include the Doppler effect, however, and were restricted to the lower atmosphere. Hourdin [1992] developed a series of models, including (a) line-by-line computation with a full Voigt (Doppler+collisions) line profile, (b) some narrow band models with various formulations, including in particular sophisticated parametrizations for the Voigt line shape, and (c) a faster parametrization well suited for GCM calculations. Some of the results of this last study are shown in Fig 8. Comparison of results from both studies shows some differences in the radiative fluxes (typically of the order of 10%) which can be attributed to the use of two large spectral intervals in the CO_2 15-μm band for the narrow band model used by Savijärvi [1991] (not published), and probably also to the use of different spectral data-naks for the computations of the band parameters. In any event, it would appear that the results are essentially consistent at the degree of accuracy required for modeling of the Martian climate at the present level of sophistication.

The CO_2 15-μm band is responsible for a significant greenhouse effect on Mars. This effect is classically estimated from the difference between the surface emission σT_s^4 and the upward fluxes at the top of the atmosphere (which are theoretically in balance over temporal and spatial averages with the incoming solar flux). From Fig. 8, the greenhouse effect can be estimated at about 7 W m^{-2} for the standard (mid-latitude) atmosphere and only about 1 W m^{-2} for the polar profile. The relative weakness of the greenhouse effect on Mars compared to that on the Earth is explained by the fact that the CO_2 15-μm band, which is centered

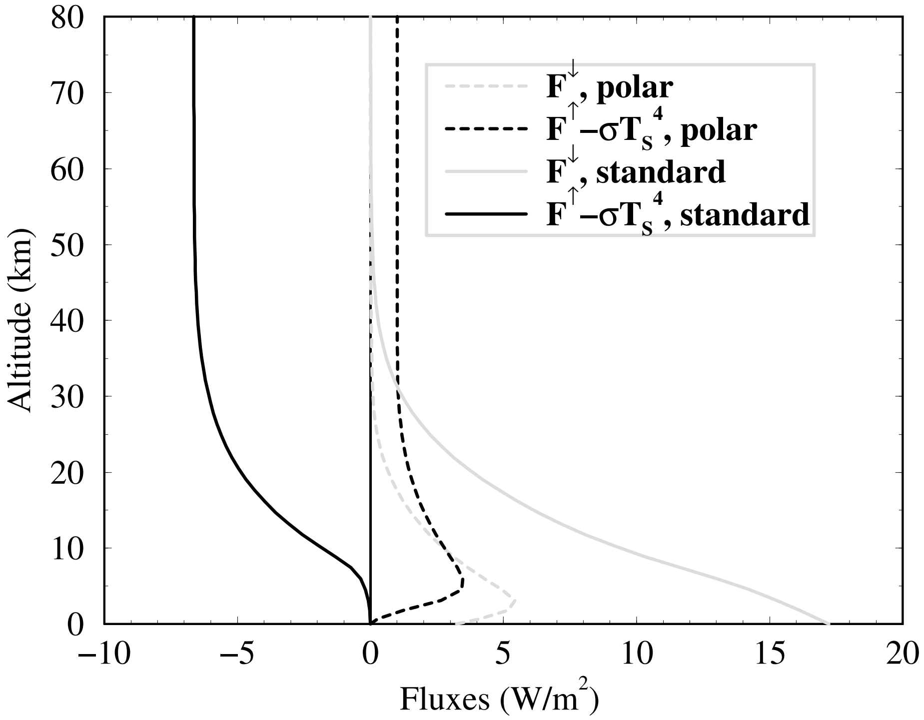

Figure 8: Upward and downward fluxes computed with a line-by-line model. The temperature profiles used for this computation are shown in Fig. 7. The results are from Hourdin (1992).

near the maximum of the Planck function for terrestrial temperatures, is farther from this maximum on Mars, and can only intercept a relatively small part of the radiation emitted by the surface. This is even more the case, of course, for the cooler polar atmosphere.

5.2.2 Water vapour

The effect of water vapor is generally considered to be negligible because the cold Martian atmosphere cannot sustain more than a few tens of precipitable μm of water vapour. In estimating the radiative impact of water vapour on Mars, Savijärvi [1991] used a simple emissivity scheme for the emission by vapour and assumed a relative humidity of 20% in a standard atmosphere. He obtained an increase of the downward flux due to water vapour at the surface of 3.6 W m^{-2}, which compares significantly with the 20 W m^{-2} due to the CO_2 15-μm bandalone. This must be considered as an estimate of the upper limit on the radiative effects of water vapour in the Martian atmosphere, since the standard temperature profile used by Savijärvi [1991] corresponds in fact to summer tropics or midlatitudes, where the humidity is at a maximum due to the warmer temperatures.

5.2.3 Ozone

Ozone is often included as a radiatively active species on Mars, since Kuhn et al. [1979] have shown that it could have a significant effect at the edge of the polar cap. However, it is generally considered to be negligeable for studies of the global Martian climate.

5.2.4 Water vapour, ice, and clouds on Mars

The thin, cold Martian atmosphere generally holds a small amount of water vapour. It is highly variable spatially, and varies temporally on seasonal timescales. The total amount is roughly equivalent to 1 to 2 km^3 of ice, compared with the terrestrial atmosphere which typically holds the equivalent of 13000 km^3 of ice, although the terrestrial stratosphere holds an amount which is more comparable to Mars. Unlike the Earth's stratosphere, however, the cold Martian atmosphere is often close to saturation, allowing the formations of hazes, clouds and frost. Scientific reviews on "the seasonal cycle of water on Mars", focussing on the physical processes that control the variations of abundance of the atmospheric water vapour can be found in Jakosky [1985] and Jakosky and Haberle [1992].

The Mars atmospheric water detector (MAWD) instrument on the Viking Orbiters monitored the spatial and temporal variations of the atmospheric water vapour column abundance for more than 1 Martian year [Jakosky and Farmer 1982]. The overall behavior of atmospheric water vapour as a function of season and latitudes is shown on figure 9. The main feature of this figure is produced by the permanent water ice cap in the north polar region in summer: direct sublimation of water ice onto the cap is the source for the large atmospheric water concentration in northern summer. To a less extent, water vapour could also be supplied to the atmosphere from the regolith [Jakosky 1983] or from the retreating seasonal polar caps. Water vapour is then transported by the atmosphere toward the southern hemisphere. In the South, observations suggest that the permanent polar cap does not lose its covering of CO_2 frost during the summer [Kieffer 1979] and no sublimation of water occurred. In fact the south permanent cap is likely to be an efficient cold trap for "permanently" removing water from the atmosphere.

The year observed by Viking may not be typical, however. Observations of atmospheric water vapour made from Earth since the 1960s [Jakosky and Barker 1984, reviewed by] suggest significant interannual variability which may be tied to the variability of the climate itself or to the possible disappearance of the CO_2 coverage of the south residual cap in some years.

Vertical distribution. Away from the polar caps, there are several pieces of evidence to suggest that water vapour is uniformly mixed within the lowest 1 to 3 atmospheric scale heights, in many case up to the saturation level where water begins condensing [Jakosky and Haberle 1992, see, page 1000,]. In a uniformly mixed atmosphere, saturation is expected to occur at a relatively high level (10-40 km), depending on the

Figure 9: Zonally averaged water vapour column abundance displayed as a function of latitude and seasons, based on Viking MAWD observations, in units of precipitable micrometers. Figure from Jakosky and Haberle (1992), data from Jakosky and Farmer (1982).

local temperature profile and water vapour abundance [Jakosky 1985]. This is consistent with the altitudes of hazes observed at the limb [Jaquin et al. 1986].

Direct observations of the vertical profile of water vapour in the spring equatorial regions were obtained in 1988 by the Phobos solar occultation measurements [Krasnopolsky et al. 1991]. The water vapour mixing ratio was found to be constant up to ~12 km and decreased above that height, suggesting that the atmosphere was saturated there. At ground level, *in situ* measurements relevant to the presence of water vapour were obtained by the two Viking Landers [Ryan et al. 1982, see].

5.2.5 Water ice hazes and clouds

Water ice clouds and hazes are frequently present in the Martian atmosphere. The physical processes that control the formation of the water ice particles in the atmosphere have been studied by various authors [Rossow 1978, Michelangeli et al. 1993, see]. As on the Earth, the occurrence and characteristics of the clouds depend on the abundance and vertical distribution of water in the atmosphere and on the atmospheric temperature (see 5.1.1 and 5.2.4 above). In addition, various processes can locally enhance the condensation of water (e.g. atmospheric waves, diurnal dust cooling, etc...).

Impact on the heat budget Unlike on the Earth, the amount of water condensing in the Martian atmosphere is too small to affect atmospheric thermodynamics through latent heat release [Zurek et al. 1992]. Nevertheless, through their effects on the radiation budget, ice clouds could affect the heating of the atmosphere and surface. Little is known on this effect and most atmospheric models [Pollack et al. 1990, Hourdin et al. 1993, e.g.] have assumed that this effect is negligible, at least on the general circulation. Although they are extensive, the high-altitude hazes are usually much thinner than the airborne dust layer lying below. Furthermore, the discrete ice clouds can be optically thick, but their occurrence is usually quite limited in space and time, and thus should only impact the heat budget locally. Besides, the task of estimating the impact of these clouds on the radiatve budget is not straightforward: a cloud may increase the planetary albedo but tends to decrease the longwave emission to space (if colder than the ground). It thus decreases the amount of solar radiation reaching the surface but increases the downward infrared fluxes. The polar hood is often observed to be both extensive and relatively thick, but it usually occurs near the polar night edge. Lindner [1990] estimated that clouds usually reduce the net radiation flux which strikes the surface except for low solar incidence angles; a common situation at polar latitudes.

5.2.6 Dust

The most prominent aerosol component of the Martian atmosphere is dust. As described in section 5.7.2, winds on Mars can exceed the threshold value for setting particles into motion to create local dust storms, which can, sometime , expand to global proportions. In fact, the spacecraft missions of the 1970s have shown that there is a persistent background dust opacity in the Martian atmosphere. For instance the color of the Martian sky observed by the Viking Landers was controlled by airborne dust. However, this permanent dust opacity seems to be highly variable in time and space.

Dust particles are tracers which can be lifted from and deposited on the surface and directly affect the environmental conditions for a probe. Above all, through their radiative effects, they strongly influence the meteorology by modifying the temperature structure of the atmosphere and alter the CO_2 condensation-sublimation cycle.

A review on the “Martian dust cycle” can be found in chapter 29 of the MARS book [Kahn et al. 1992], althought key articles on this matter have been published since [Martin and Richardson 1993, Korablev et al. 1993, Pollack et al. 1995, Clancy et al. 1995, Chassefiere et al. 1995]. This section summarizes what we know about the martian airborne dust, focusing on its radiative properties and size distribution, its spatial and temporal distribution, and its lifting and transport by the Martian winds.

5.2.7 Microphysical properties of the dust

Over the past 20 years, scientists have analyzed data obtained by various spacecraft to define the key radiative and microphysical properties of airborne dust. Reviewed of these efforts can be found in Murphy et al. [1993], Kahn et al. [1992] and Pollack et al. [1995].

The atmospheric dust particles key properties can be described by the following parameters:

- **The particle shape and size distribution**. The size distribution is characterized for instance by the geometric cross-section weighted mean radius r_{eff} and variance ν_{eff} (Notice that r_{eff} can be very different than other radius-like parameters such as the "modal radius" if the size distribution is large).

- **The dust optical properties**, usually characterized by the imaginary index of refraction n_i and the single scaterring albedo ω_0 at each wavelength.

From this information, one can theoretically calculate the single-scaterring phase function (characterized for instance by the assymetry parameter g) and the extinction coefficient Q_{ext}. In fact, the direct measurement of particle size distribution and shape would require *in situ* sampling of atmospheric particles, which has never been done for Mars. These microphysical properties have only been deduced through radiative transfer calculations and are closely related to the optical properties. In any case, the knowledge of the radiative properties of the dust is of key importance to model the impact of the dust on the meteorology.

Estimating exact and universal values for the dust microphysical properties is not straighforward since they are expected to vary spatially and temporally. In most studies, results are interpreted as best-fit parameters, and not unique values. They are thus strongly model dependent [Chylek and grams 1978, e.g.]. Besides, the problem is compounded by the presence of diurnally varying ground fogs, higher level water-ice hazes, or water ice coating the mineral dust particles [Colburn et al. 1989, Jaquin et al. 1986].

Radiative properties at solar wavelengths

Visible: Measurements of the sky brightness above Viking Lander 1 and 2 have been used to infer the dust single scaterring properties ω_0 and g at visible wavelength (0.49, 0.55, 0.66 μm). The dataset, originally analyzed by the widely cited Pollack et al. [1979] has been recently and more accurately reanalyzed by Pollack et al. [1995]. They found ω_0 increasing from 0.73-0.80 (at 0.49 μm) up to 0.93-0.94 (at 0.66 μm), whith g decreasing from ~ 0.7 to ~ 0.6. They found that the particle were nonspherical. Further analyses suggested that the mean radius r_{eff} was about 1.5-1.9 μm with a large variance ν_{eff} of about 0.5 μm.

Clancy and Lee [1991] used the Viking orbiter infrared thermal mapper (IRTM) emission-phase-function measurements in the solar band (0.3-3μm) Their results are in good agreement with Pollack et al. [1995] ($\omega_0 \sim 0.92$, $g \sim 0.55$, although their study suggested much smaller particles. This could be due to the fact that they used only measurements made at high scaterring angles, which cause them to have a much greater sensitivity to particle shape than particle size [Pollack et al. 1995]. Jaquin et al. [1986] analysis of the Martian limb Viking orbiter observations also supports values of ω_0 above 0.9 and $g \sim 0.6$ in the red ($\sim 0.6\mu$m).

Ultraviolet Martian dust was observed by the Mariner 9 ultraviolet spectrometer (UVS) during the 1971 dust storm. Pang and Ajello [1977] found that the real index of refraction at these wavelength was $\sim$1.8

in the UV with a rather high imaginary (absorption) index n_i increasing with decreasing wavelength from 0.350 μm down to about 0.210 μm and dropping off shortward of this wavelength (n_i ∼0.01 at 0.305 μm, 0.02 at 0.268 μm). They found r_{eff} of the order of 1 μm with $\nu_{eff} \geq 0.2\mu$m. However, Chylek and grams [1978] showed that rather different values (e.g. n_i ∼0.004 at 0.268 μm; $r_{eff} \sim 0.2\mu$m ; $\nu_{eff} \sim 0.9\mu$m) could be obtained from the same dataset if the irregular shape of the particle was taken into account.

Composite spectra at solar wavelengths Ockert-Bell et al. [1994] extended the Pollack et al. [1995] data over the solar wavelengths using the composite spectra of the Martian soil from Mustard and Bell III [1994]. They used this model with r_{eff}=1.85μm and ν_{eff}=0.51μm to simulate the reflectance observed with the Viking IRTM solar channel during the dust storms and obtain very good agreements, except in the morning cases, certainly because of the presence of airborne water ice. They showed that multispectral calculations were essential to obtain accurate results. Such a composite spectrum should thus be used in radiative transfer models to compute, for instance, heating rates and surface fluxes with any accuracy. However, this spectra may not be valid at every wavelengths (for instance, their UV values are very different than the one measured by Pang and Ajello [1977] and Chylek and grams [1978].

Thermal infrared radiative properties

Both Mariner 9 infrared interferometer spectrometer (IRIS) and Viking IRTM showed that the properties of the Martian dust in the infrared strongly vary with wavelength. In particular, dust is characterized by the silicate induced absorption near 9 μm.

Visible/9-μm extinction opacity ratio. A first important diagnostic to analyze and model the Martian dust is the scaling of the dust opacity in the infrared compared to the visible. Martin [1986] compared his IRTM 9 μm opacity determinations over the two Viking Landers sites with the lander solar extinction observations [Colburn et al. 1989]. He determined a visible (0.67 μm) / 9-μm opacity ratio of 2.5. This value is supported by separate analyses of the IRTM emission-phase-function visible and 9-μm sequences. [Clancy et al. 1995]. However note that the comparison of the extinction opacity over the solar band with the extinction opacity integrated over the Planck function corresponding to the thermal emission of Mars would give visible/IR opacity ratio well above 2.5, since dust is less absorbing outside the 9 μm band in the thermal infrared.

Composite spectra in the thermal infrared Toon et al. [1977] fit brightness temperatures models to the Mariner 9 IRIS observations (5-50 μm) of the 1971 global dust storm. They showed that the shape of the observed 9-μm absorption could be reproduced by using the optical properties of a clay mineral sample called montmorillonite and the modified-gamma size distribution with r_{eff}=2.7 μm and ν_{eff}=0.4 μm. Widely used,

r_{eff} μm	ν_{eff} μm	λ μm	Conditions of observation	Sources
1.3	0.2	0.268,0.305	dust storm	Mariner 9 UVS [Pang et al. 1976]
0.2	0.9	0.268,0.305	dust storm	Mariner 9 UVS [Chylek and grams 1978]
1.85	0.5	0.5-0.9	clear	Viking Lander [Pollack et al. 1995]
1.5	0.5	0.5-0.9	dust storm	Viking Lander [Pollack et al. 1995]
1.7	0.25	1.9,3.7	clear	Phobos [Chassefiere et al. 1995]
2.0	0.5	1.9,3.7	clear	Phobos [Chassefiere et al. 1995]
2.7	0.4	~ 9	dust storm	Mariner 9 IRIS [Toon et al. 1977]
1.8	0.8			Clancy et al. [1995]

Table 4: Comparison of the Martian dust size distribution parameters inferred from various spacecraft observations.

the Toon et al. dust model has become a kind of standart Martian dust model. However, this model is not "universal". It predicts absorptions at 20 μm which are not observed, and requires a separate ultraviolet-visible absorbing component to match the observed behavior of the dust in this wavelength region For instance, it predicts a visible/9-μm extinction opacity ratio close to 1.0, much lower than the observed ratio 2.5 [Clancy et al. 1995].

An alternative model has been recently proposed by Clancy et al. [1995] to match the complete ultraviolet-to-30-μm absorption properties of the dust. Their model is based on a smaller (r_{eff}=1.8 μm) broader (ν_{eff}=0.8 μm) particle size distribution coupled with the use of the optical properties of a weathering product of basaltic glass called palagonite. However, their model is not able to match the observed 9-μm absorption in detail.

Dust particle size

The size distribution inferred by the studies described above are summarized in table 4. Another important measurement regarding the dust particle sizes is the Phobos near-infrared (1.9 and 3.7 μm)solar occultation measurement of dust extinction profiles. [Chassefiere et al. 1992, Korablev et al. 1993, Chassefiere et al. 1995]. The effective radius r_{eff} was found to increase from $\sim$0.8 at 25 km up to $\sim$ 1.6μm at 15 km, with ν_{eff} around 0.25 μm. Chassefiere et al. [1995] computed a vertically averaged r_{eff} of about 1.7 μm for ν_{eff} = 0.25, possibly $\sim$2 in the case ν_{eff}=0.4, which is consistant with the Pollack et al. [1995] results. These values were also supported by the Drossart et al. [1991] analysis of the Phobos ISM infrared spectrometer data acquired during the same period.

The decrease of the dust particle size with altitude observed by Phobos is not surprising because of the size-dependent sedimentation (fall speed) rate. Similarly, it was expected that the mean particle size would be higher during high dust opacity periods (dust storms) than during the clear period when reduced dust raising is expected. However, several authors have pointed out that the dust distribution size does not seem to vary during and between the dust storms [Toon et al. 1977, Pollack et al. 1995]. This could be explained if the dust main removing process, unlike sedimentation, is size-independent (eddy mixing or condensation removal), or if local dust storms continually supply fresh material to the atmosphere.

The spatial and temporal distribution of dust is discussed in section 5.7.1.

5.3 THE PLANETARY BOUNDARY LAYER

5.3.1 Structure and Importance of the Planetary Boundary Layer

The planetary boundary layer is of prime importance for understanding and modelling the Martian meteorology and climate. Thermal structure, momentum exchange with the surface, lifting and deposition of dust and water cycle are all controlled by processes occurring in the lowest part of the atmosphere. Moreover, the Planetary Boundary Layer is the environment of surface missions such as landers or rovers. It is also the environment for one of the most crucial phases of a probe entry.

The Planetary Boundary Layer is the region near the surface where turbulent processes are important. This turbulence is created in part by the wind shear on the surface and is also greatly influenced by the static stability, which is defined by the vertical gradient of the potential temperature $\theta = T(p/p_s)^\kappa$ (a quantity conserved by air parcels in adiabatic motions). A stable atmosphere is characterized by the potential temperature increasing with height. If the potential temperature decreases with height (i.e., the temperature decreases faster than the adiabatic lapse rate, which is about 4.5 K km^{-1} on Mars), the buoyancy of an air parcel slightly displaced upward is larger than that of the surrounding atmosphere and the air parcel is advected further upward, away from its original position. In such an atmosphere, the convection generated by this instability rapidly mixes potential temperature and restores a neutral atmosphere, which corresponds to a constant value of the potential temperature. More generally, a less stable atmosphere is more favorable for the creation of turbulence than a more stable atmosphere, which has a larger positive gradient of θ in the vertical.

The height of the Planetary Boundary Layer typically varies between a few kilometres in summer during the day, when the strong heating of the surface creates strong convection, and probably collapses to a few tens of metres in very stable conditions above the cold night surface.

Within the Planetary Boundary Layer one usually distinguishes a surface layer, which typically consists of the first 10% of the Planetary Boundary Layer and is defined as the region where the turbulent heat and momentum fluxes can be considered constant with height. This region is the most important when considering the environment a probe will experience on the surface. The ultimate heat exchange with the solid surface occurs via conduction and molecular viscosity in a very thin layer, which is believed to be about 1 cm thick on Mars.

5.3.2 The Surface Layer at the Viking Sites

The meteorological sensors onboard the Viking Landers gave a unique opportunity to probe the surface layer on Mars.

The thermal and wind structure in the surface layer can be described roughly based on the Monin-Obukhov theory. This theory [see e. g. Panofsky and Dutton 1984] predicts the following expressions for the vertical derivative of wind

$$\frac{du}{dz} = \frac{u_*}{k_a z}\phi_m\left(\frac{z}{L}\right) \tag{1}$$

and for the potential temperature

$$\frac{d\theta}{dz} = \frac{H}{\rho c_p k_a u_* z}\phi_h\left(\frac{z}{L}\right) \tag{2}$$

where

- u is the horizontal wind (its direction is constant in the surface layer)
- z is the altitude above the surface
- u_* is the friction velocity related to the surface stress (or momentum flux) $\tau = \rho u_*^2$
- H is the turbulent heat flux
- $k_a \simeq 0.4$ is the von Karman constant
- L is the Monin-Obukhov length

  $$L = -\frac{u_*^3 c_p \rho T}{k_a g H} \tag{3}$$

  which is positive in an unstable atmosphere ($H < 0$) and negative in a stable atmosphere.
- As just stated, ϕ_m and ϕ_h are assumed to be universal functions and are taken directly from studies of the terrestrial boundary layer. For instance, Tillman et al. [1994] uses functions derived by Dyer [1974]:

$$\phi_m(\zeta) = \begin{cases} 1+5\zeta, & \zeta > 0 \\ (1-16\zeta)^{-1/4}, & \zeta < 0 \end{cases} \tag{4}$$

$$\phi_h(\zeta) = \begin{cases} 1+5\zeta, & \zeta > 0 \\ (1-16\zeta)^{-1/2}, & \zeta < 0 \end{cases} \tag{5}$$

In this theory, $\zeta = z/L$ is a monotonic function of the flux Richardson number $Rf = \zeta/\phi_m(\zeta)$, the ratio of the rate of destruction of turbulence by stratification to the rate of creation of turbulence by wind shear. For neutral conditions, $z/L = Rf = 0$ ($L = \infty$), mechanical turbulence dominates. At the opposite extreme, large values of z/L imply primarily convective turbulence. This is mainly the case during the day on Mars, at least during summer, when the direct insolation of the surface results in very warm surface temperatures. For negative values (especially during the night), L has a simple geometric meaning: at heights large compared to $|L|/10$ convection dominates, whereas mechanical turbulence dominates below.

By introducing the roughness length z_0, below which altitude above the surface the horizontal wind averages to zero, Eqs. 1 and 2 can be integrated vertically to give, for u,

$$u = \frac{u_*}{k_a}\left[\ln\frac{z}{z_0} - \psi_m\left(\frac{z}{L}\right)\right] \tag{6}$$

and for the potential temperature,

$$\frac{\theta - \theta(z_0)}{\theta_*} = \frac{1}{k_a}\left[\ln\frac{z}{z_0} - \psi_h\left(\frac{z}{L}\right)\right] \tag{7}$$

with ψ defined, for both momentum and temperature,

$$\psi = \int_{\zeta_0}^{\zeta}[1-\phi]\,d\zeta/\zeta, \text{ with } \zeta_0 = z_0/L \tag{8}$$

Together, the three Eqs. 3, 6 and 7 allow one to determine the three parameters L, u_* and H by using the temperature and wind measurements recorded by the meteorological arm of the Viking Landers, 1.6 m above the Martian surface, providing that one has an estimate of the roughness length z_0 and of the temperature $\theta(z_0)$. In order to relate this temperature to the surface temperature, T_s, which was measured both by the landers and from infrared retrieval by the orbiters, molecular thermal diffusivity and kinematic viscosity in the first few millimetres above the surface must be taken into account. This retrieval of the characteristics of the surface layer from Viking data was first done by Sutton et al. [1978]. Values for the roughness were estimated from the Viking images to be between 0.1 and 1.0 cm. Sutton et al. [1978] concentrated on the earliest phase of the mission. They found maximum heat fluxs near local noon ranging from 10 to 20 W m^{-2}. Maximum frictional velocities were found in late morning at Viking 1 ($\simeq$ 0.4-0.6 m s^{-1}) and shortly after dawn at Viking 2 ($\simeq$ 0.25-0.35 m s^{-1}).

Tillman et al. [1994] performed a more complete study by using Viking data at various seasons. Estimated values of L, u_* and H are given for different seasons and time of day in Table 5. Moreover, Tillman et al. [1994] computed spectra from the high-frequency data, taken either each 4.8 s or each 15.8 s, for the period listed in this Table. The good agreement between the measured spectra and that computed from the Monin-Obukhov theories tends to confirm that the similarity theory developed on Earth is general enough to be applied on Mars. A best agreement between the observed and modeled spectra is achieved for $z_0 = 1 - 3$ cm.

The characteristics of the Planetary Boundary Layer, which give the mean thermal and dynamics structure in the last few or few tens of metres above the surface, can also be used in addition to derive estimates

L_s	132	15.5			16.0						65.1	
h_i	4.8	11.0	0.67	1.7	11.0	12.0	14.0	21.1	22.1	23.2	12.1	13.1
h_f	5.8	12.0	1.6	2.7	12.0	13.0	15.0	22.0	23.1	24.2	13.1	14.1
L	107	-16	10	11	-46	-48	-83	26	15	14	-8.2	-6.7
u_*	0.21	0.37	0.08	0.10	0.63	0.67	0.74	0.20	0.12	0.11	0.28	0.25
H	-0.22	11.3	-0.23	-0.28	19.9	24.2	20.2	-1.00	-0.47	-0.34	10.6	9.5
U	3.4	4.4	1.2	1.4	7.8	8.4	9.3	2.6	1.8	1.6	3.2	2.9
T_s	194	236	186	184	236	243	245	193	191	189	259	261
T_a	195	214	188	187	213	217	225	197	193	191	233	236

Table 5:

of the wind and temperature [see e. g. Panofsky and Dutton 1984]. Unfortunately, these parameters are known only at the Viking sites and for particular seasons. Those observations must be used in order to tune the Planetary Boundary Layer scheme of the GCM.

5.3.3 Modelling the Atmospheric Boundary Layer

Other than at the Viking Lander sites, the rest of the Planetary Boundary Layer of Mars is poorly observed. In addition, the representation of the Planetary Boundary Layer above the surface layer does not obey simple similarity relations since large-scale dynamics (rotation and pressure gradient effects) are of greater importance as one goes farther from the surface. Note in particular that the wind changes direction in the boundary layer since the balance between Coriolis force and pressure gradient which prevails at the top of the Planetary Boundary Layer is broken by friction. As a consequence, winds have a component in the direction of the low pressure inside the Planetary Boundary Layer.

This region of the Martian atmosphere has been studied through the use of numerical models. Different studies have been performed, but with a very similar approach. Numerical models of the terrestrial Planetary Boundary Layer were adapted for Mars by Haberle et al. [1993] and Savijärvi [1995]. Both studies use a second order closure model in which turbulence is treated as a vertical mixing, the coefficient of which is computed from an estimate of the turbulent kinetic energy in the atmospheric layer, this estimate itself being computed as a balance between creation of mechanical turbulence by the wind shear and destruction by the atmospheric stability. In fact, a similar model is already included in the LMD GCM [Hourdin et al. 1993].

The Planetary Boundary Layer models generally include, in addition to the turbulent mixing, a radiative code, a parametrisation of thermal conduction in the soil and the prescription of the large-scale wind at the top of the Planetary Boundary Layer.

The numerical results can be validated by comparison with the temperature measurements at the Viking sites and with the Viking entry profiles. By tuning parameters, such as the surface thermal inertia of the surface, Savijärvi [1995] has shown that it is possible to reproduce very accurately both the diurnal temperature variations at the surface and at 1.6 m, and the descent temperature in the last 8 km for Viking Lander 1.

5.3.4 Diurnal Variations of the Planetary Boundary Layer

Models predict that the structure of the Martian Planetary Boundary Layer undergoes very strong diurnal variations, especially during summer. During the day convection occurs, initiated by the strong solar heating at the surface. The Viking 1 temperature entry profile, at 16:00 local time, was close to adiabatic in the first few kilometres. This is consistent with results from numerical models which predict active convection during afternoon extending at least up to about 4 km.

During night, the rapid cooling of the surface and surface layer results in a collapse of the Planetary Boundary Layer. At that time, the Planetary Boundary Layer can be less than 100 m high.

This strong diurnal cycle of the structure of the Planetary Boundary Layer is probably attenuated during winter and in very dusty conditions, when the solar radiation reaching the surface is reduced.

Note, however, that except for the Viking 1 entry, the height of the Planetary Boundary Layer is not well constrained by observation [see the discussion Zurek et al. 1992, p. 912] and has not been systematically investigated by numerical models.

5.3.5 Winds in the Planetary Boundary Layer

The surface winds observed by the Viking landers during summer showed a remarkably repeatable diurnal cycle controlled by the local orography, with the wind being predominantly downslope during the night and upslope during the day. Those winds can be roughly reproduced with a 1D model [Haberle et al. 1993] or a 2D model Siili [1994] of the Planetary Boundary Layer.

Models also predict the creation of a low-level nocturnal jet. Haberle et al. [1993] reported the simulation of the creation of a 17 m s^{-1} jet at 100 m above the surface just before dawn, at a time when the surface wind is relatively slight. Such low level jets are currently observed on Earth, for instance on the United States Great Plains [Savijärvi 1991]. The explanation for the creation of those jets was first proposed by Blackadar [1957]: during the day, when convection is active, there is a balance between vertical mixing by convection, pressure gradient and Coriolis forces. The sudden breakdown of convection and consequent collapse of the Planetary Boundary Layer leaves the atmosphere in inbalance. This produces large oscillations (known as inertial oscillations) which can produce large velocities, even larger than the velocity corresponding to geostrophic balance with the pressure field.

As explained by Haberle et al. [1993] the conditions for this nocturnal low-level jet are fulfilled on Mars, especially in summer and for rather clear conditions: the initial force inbalance is large since convection is strong, the collapse of the Planetary Boundary Layer is rapid because of the low thermal inertia of the Martian soil and relatively small greenhouse effect of the Martian atmosphere, and, in the tropics, nights are long enough for the inertial oscillation to have an effect.

This low level jet could be crucial for balloons flying above the Martian surface and possibly for probe entry during the night.

5.3.6 Frost and Snow in the Planetary Boundary Layer

Pollack et al. [1977] have reported on a frequent frosting and fogging around the Viking Lander cameras. Savijärvi [1995] have introduced a simple scheme for hydrology and ice cloud physics in their Planetary Boundary Layer model. The simulation at Viking 1 for the early phase of the mission produces fog which extends up to about 60-80 m during the night and disappears within two hours after sunrise. However the fog remains relatively thin ($\simeq$0.05 g m^{-3} at maximum) resembling in that respect the Earth ice (cirrus) clouds.

5.4 THE GLOBAL CIRCULATION

The first-order effect of solar heating on the global-scale motions of a planetary atmosphere is through its dependence on latitude, which causes the insolation to be greater at low and middle latitudes than at high. If the planet did not rotate at all, then the air at the sub solar point would tend to rise convectively and that at the anti-solar point would tend to fall ; air would migrate from one to the other in a pattern symmetric about the planet- Sun line. Even very slow rotation, however, like that of Venus, tends to distribute the heating around bands of constant latitude faster than typical radiative and dynamical time constants, so that the rotational poles define the main axis of symmetry. In the upper atmosphere of Venus, there is some evidence that both equator-to-pole and subsolar-to-antisolar regimes are present together. In the deep Venusian atmosphere, the time constant for radiative cooling (i.e. the characteristic time in which the atmosphere would cool down if the Sun were removed) is several thousand times the length of even the long Venusian day , so that the Sun appears to the atmosphere to move rapidly overhead and the predominant gradients are equator-to-pole. This is the case also on Earth and Mars, where the time constants are shorter but so also is the length of the day.

The net effect of the basic gradients of temperature with latitude and height expected on each of the terrestrial planets is to tend to force an hemispherical convection cell with rising air at low latitudes moving polewards and falling air at high latitudes moving equatorwards. The rotation of the planet will tilt the wind vectors at an angle to the equator, as observed for example in the prevailing trade winds on Earth or in the migration of cloud patterns on Venus. This basic pattern was inferred by Hadley in the 18th century and is named after him. In fact, in the atmospheres of the terrestrial planets Hadley's circulation is unstable, and multiple cells are formed instead. Within individual cells, the motions are on average smooth flows but at any given time have a variety of wave and chaotic motions superimposed on them. It is this pattern of large scale convection cells and chaotic wavy motions is often called the global (and sometimes general) circulation.

The proceeding sections describe various aspects of the global circulation of the atmosphere of Mars with reference to any observational evidence for those aspects and with a brief assessment of the variability of the phenomena.

5.4.1 Zonal Mean Circulation

The primary source of information about the zonal mean ciculation of the atmosphere of Mars comes from temperature soundings made by the IRIS instrument onboard the Mariner 9 spacecraft [Hanel et al. 1972]. This instrument provided over 21,000 spectra from which the thermal structure can be retrieved with a resolution of one scale height (10 km) up to about 45 km in altitude. This data is reviewed in detail in Zurek et al. [1992]. Unfortunately, the IRTM instrument on the later Viking Orbiters had only a single channel sensitive to atmospheric temperatures [Martin 1986], and hence gave no information on thermal structure in the vertical.

Figure 6, in the section on thermal strcuture, shows retrieved IRIS temperatures over the period $L_s = 43°$–$54°$, which corresponds to northern spring. There are large horizontal temperature gradients in the southern, winter hemisphere, especially between the edge of the polar cap at 60° S and about 30° S. Horizontal temperature gradients in the northern hemisphere are weak, with maximum temperatures of about 220 K over the region between the equator and 60° N. Much of the IRIS data is distributed in a non-uniform manner, in terms of local time of day and latitudinal coverage, so these temperatures are probably not true zonal means. Retrievals were originally hampered by the large quantities of dust in the Martian atmosphere and so are only available for short periods in the data, such as that shown in Fig. 6, though there has been some effort to re-analyse the profiles for periods of high dust [Santee and Crisp 1993].

Dotted curves are also shown in Fig. 6, which give the zonal wind which is implied by thermal wind balance with these temperatures [Pollack et al. 1981]. The principal feature is the strong eastward jet, reaching speeds of up to 120 m/s, which overlies the sharp horizontal temperature gradients near the edge of the polar cap. There are weaker regions of easterlies and westerlies in the summer hemisphere. Unfortunately,

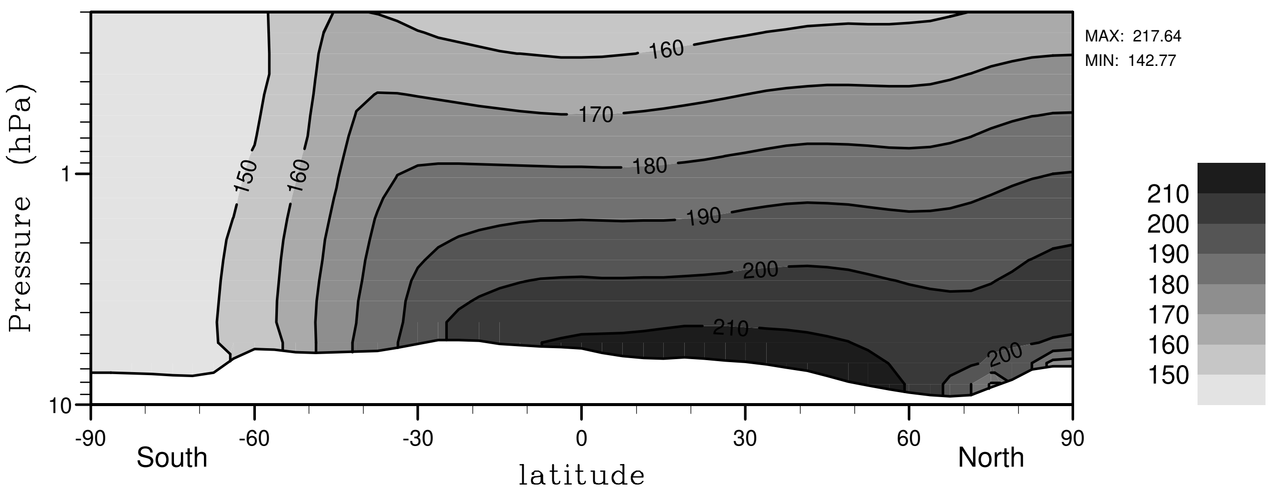

Figure 10: Zonal-mean temperature for the period $L_s = 43°–54°$from the LMD model.

there are few tracers of the atmospheric circulation which can be used to verify these winds directly. The only possibilities are clouds, which are generally low-lying and tied to topographic features, and dust storms, which are restricted to particular seasons and locations. The thermal wind balance is assumed to be accurate to within about ten percent in mid- and high-latitude regions as on Earth. However, the balance breaks down within 20–30°of the equator, where the Coriolis force becomes small, and high in the atmosphere, around 50-60 km upwards, where drag due to breaking gravity waves (see section 5.6.3) may become a dominant term in the force balance. To obtain a wind field in a more complete balance with the zonal mean temperature field, experiments must be conducted with a numerical general circulation model which uses the primitive equations of meteorology and parametrisations of processes which are not resolved explicitly, such as gravity wave drag.

General circulation models [Pollack et al. 1981, Haberle et al. 1993, Hourdin et al. 1993] of the Martian atmosphere are able to reproduce a similar pattern of zonal-mean temperatures and winds for the season corresponding to that shown in Fig.6. For comparsion, zonal-mean temperature and wind from Hourdin et al. [1993] are shown in Figs. 10,11 respectively.

This pattern of winds and temperatures is basically reflected about the equator for northern hemipshere winter, though the circulation is then somewhat stronger owing to the eccentricity of the Martian orbit which results in a shorter, hotter southern hemisphere summer.

The mean meridional circulation of the Martian atmosphere may also be diagnosed from model studies. This circulation is dominated at the solstices by a single, giant Hadley cell with a rising branch at about 30° latitude in the summer hemisphere and a falling branch at about 30° latitude in the winter hemipshere. The Hadley cell rises to about 40 km altitude. This cell is responsible for the bulk of latitudinal atmospheric transport (of heat, momentum, dust and other constituents) in the equatorial regions, until wave motions take over in mid-high latitudes [Haberle et al. 1993, Barnes et al. 1993, 5.5.1]. The meridional circulation on

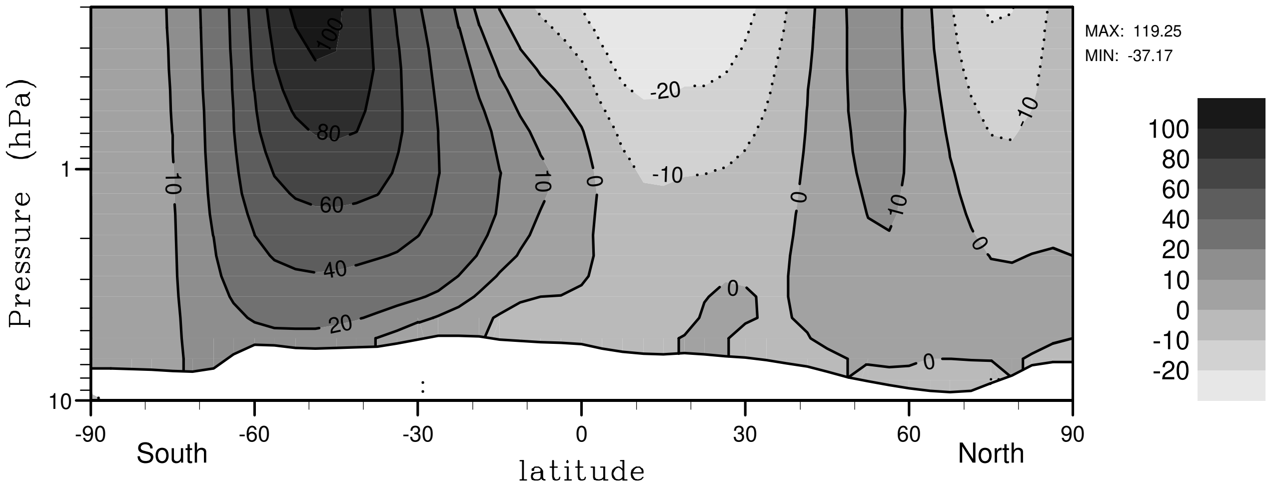

Figure 11: Zonal-mean winds for the period L_s =43°–54°from the LMD model.

Mars tends to be dominated by this single cell for much of the year with shorter periods when two, weaker cells are present close to the equinoxes as the direction of transport in the large cell reverses between summer and winter. The mean meridional circulation taken from the Oxford GCM is shown in Fig. 12 for northern hemisphere winter solstice, and in Fig. 13 for northern hemisphere autumn equinox.

5.4.2 Condensation Flow

As a result of the very low thermal inertia of the Martian surface and the low opacity of the atmosphere at infrared wavelengths, the temperature of the surface undergoes substantial excursions, both during the day and night and between seasons. In particular, at high latitudes during the winter seasons the temperature of the surface, and at higher altitudes in the atmosphere, falls below 148K for long periods of time. This temperature is significant since, at pressures of around 10 hPa (comparable to the mean atmospheric pressure at the surface), CO_2 will condense to form the solid phase (to a good approximation, the condensation temperature follows the Clausius-Clapeyron form given by

$$T_{cond} = \frac{3182.48}{23.3494 - \ln p}$$

where T_{cond} is in K and p is in hPa; see James et al. [1992]). Since the bulk of the atmosphere consists of CO_2, this results in a large fraction of the mass of the atmosphere in the winter hemisphere condensing onto the polar ice cap.

Condensation during winter and the subsequent sublimation in the spring season proceeds at a rate essentially determined by an energy balance between the rate of energy loss, associated with net radiative cooling (or heating) of the surface and atmosphere, and the corresponding energy changes associated with the release of the latent heat of sublimation of CO_2. Observations (e.g. see James et al. [1992]) and

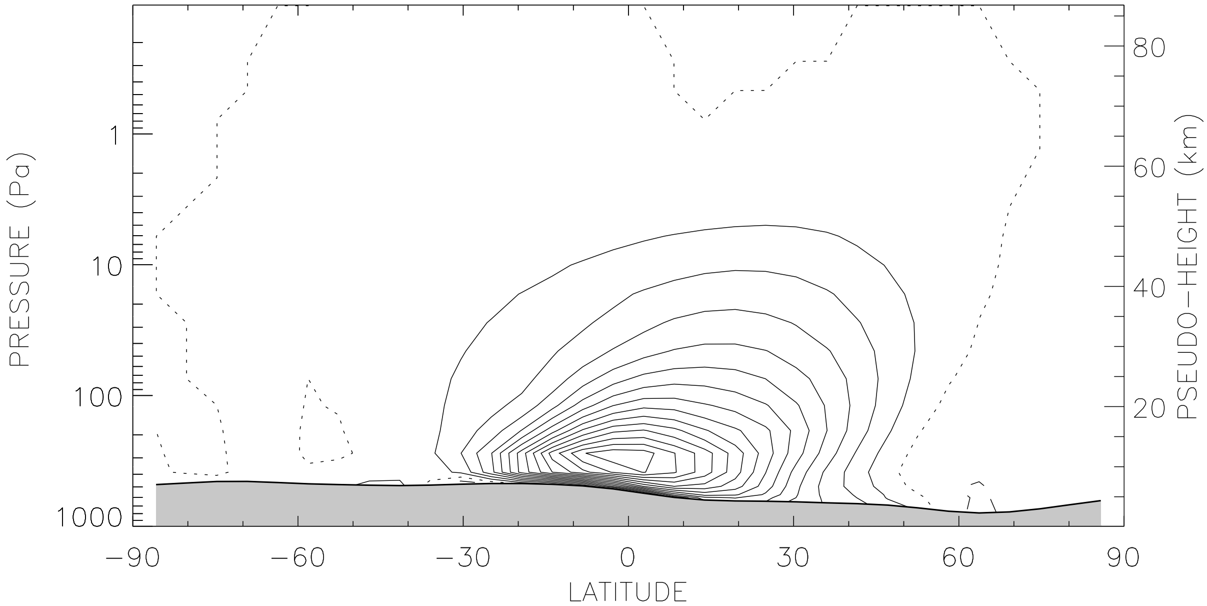

Figure 12: Mean meridional circulation northern hemisphere winter solstice, L_s =270°, from the Oxford model.

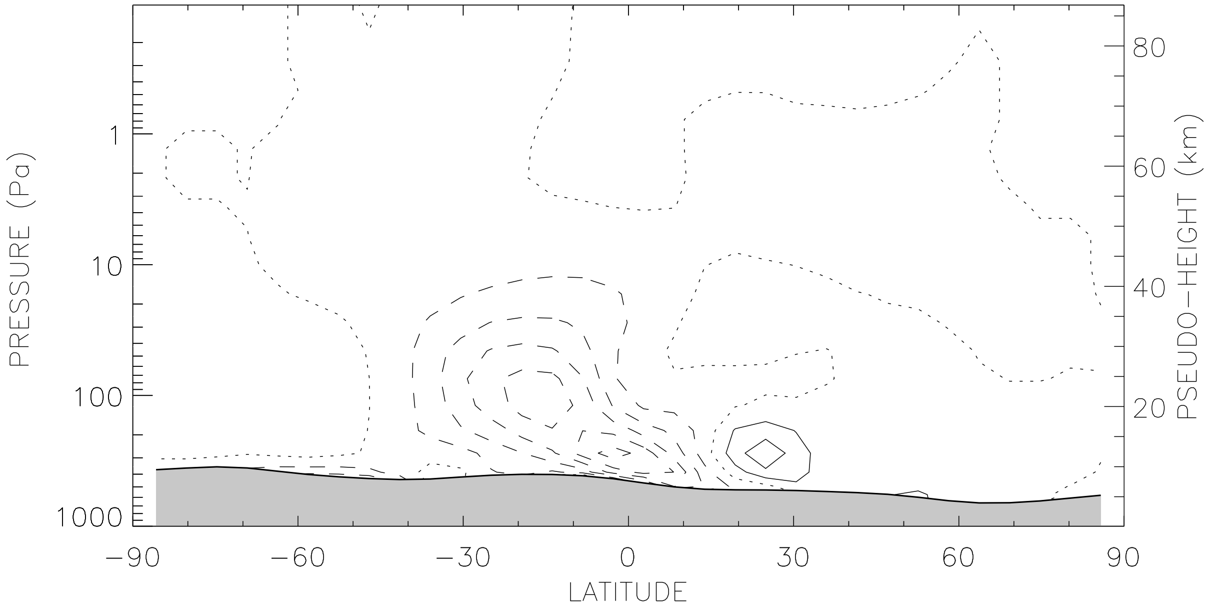

Figure 13: Mean meridional circulation at northern autumn equinox, L_s=180°, from the Oxford model.

modelling studies (Pollack et al. [1990]) suggest that deposition of CO_2 on the polar caps may take place either directly at the surface, via formation of CO_2 frost, or via the formation of clouds of CO_2 condensate in the atmosphere, forming a 'polar hood' cloud during the winter. Deposition in the autumn and winter seasons leads to extensions of the polar ice cover to latitudes as low as 40° S and 55° N respectively for the southern and northern caps, during which around 25-30% of the total atmospheric mass may accumulate in the form of CO_2 ice.

The seasonal loss and release of this quantity of mass during the year leads to substantial transport of atmospheric mass at various times during the year between the northern and southern hemispheres. A substantial fraction ($\sim$ 60 %) of the seasonal pressure variation observed at the Viking landers is apparently due to this direct mass deposition of CO_2 ice, the remainder of the variation being due to meteorological variability associated with changes in the large-scale circulation (Hourdin et al. [1993 1995], Pollack et al. [1993]). The rate of mass deposition leads to an additional component of vertically-averaged north-south wind of up to 20-30 cm s^{-1}, peaking around the edge of the condensing polar cap (Haberle et al. [1993]). Since this mass drift also entails large changes in latitude for mass elements of the atmosphere, this leads to substantial changes in the zonal wind as these mass elements approximately conserve their angular momentum. Thus the subliming CO_2 tends to spiral outwards in an anticyclonic direction as it moves towards lower latitudes, and spirals inwards in a cyclonic direction (in the same sense as the planetary rotation) as it moves to higher latitudes in the opposite hemisphere towards the condensing polar cap. Estimates for the magnitude of this enhancement to the zonal wind suggest values locally around 20 m s^{-1} or even greater (Haberle et al. [1979],Zurek et al. [1992]), peaking around the equinoxes. This may contribute to an enhancement of the occurrence of local dust storms equatorward of the retreating polar cap.

5.5 GLOBAL SCALE WAVE

5.5.1 Planetary Waves

Planetary waves is the name given to global scale atmospheric waves or modes as they are often called. They are zonally asymmetric disturbances in the pressure, temperature and velocity fields with wavelengths greater that about 3000 km. They can be categorised as follows:

Forced Modes: These are waves that are driven by thermal and mechanical displacements of air associated with zonal asymmetries in the surface of the planet e.g. surface topography.

Free Modes: These are waves that correspond to resonant modes of the atmosphere. They are excited by essentially random forcing in much the same way as one might excite a resonant mode in a guitar string by strumming it.

Waves resulting from instabilities: Rapidly rotating atmospheres like that of Mars are can become unstable to infinitesimal disturbances which grow and form waves.

Other forced waves: Waves can also occur via periodic changes in external forcing such as the diurnal cycle in isolation which forces thermal tides.

5.5.2 Forced Stationary Waves

When air is lifted mechanically over mountains or when the air over a mountain is heated more than that in the surrounding valley stationary planetary waves can form. On Mars they generally have horizontal wavelengths greater than approximately 3000 km and are referred to as stationary because of their zero phase speed i.e. their peaks and troughs are fixed in space over the mountain.

On the Earth stationary waves are forced both thermally and mechanically by mountain ranges such as the Rockies and also by diabatic heating changes associated with land-sea contrasts. The waves can influence weather and climate on a regional scale quite considerably by, for instance, modifying the direction of the wind so that it blows from a cold continent rather than from a warm sea and thus reducing the air temperature by several degrees. They also contribute significantly to the heat and momentum transport in middle latitudes, especially in the northern hemisphere.

On Mars large scale topographic features provide the main forcing for stationary waves and given the extent of the topography it is expected that stationary waves will have a greater effect on both regional circulation, and on the global circulation than they do on the Earth. Also large scale differences in surface albedo and thermal inertia which cause regional differences in heating may force stationary waves, although it is generally thought that such forcing will be a second order effect compared to the forcing by the topography.

The linear theory of planetary waves suggests that there are two forms for the vertical structure. The waves can either be trapped in the vertical and have amplitudes that are exponentially decaying with height or they can be vertically propagating with amplitudes that increase with height as the inverse square root of density. The latter solutions are particularly important as the amplitude of a vertically propagating wave may get so large that a form of wave breaking occurs that exerts a force on the mean flow. Such wave breaking, or Rossby wave breaking, is often cited as the mechanism by which the northern hemisphere polar vortex on Earth gets broken up. The edge vortex is said to be distorted in the 'surf zone' and these distortions lead to temperature warmings. In the southern hemisphere on Earth planetary waves are less frequent and the vortex is less disturbed. This leads to colder temperatures within the vortex and, ultimately, the destruction of ozone. Vertically propagating planetary waves in the northern hemisphere on Earth are one of the reasons why the Arctic does not experience and ozone hole.

There is little observational evidence for stationary waves in the Martian atmosphere although are very good reasons to expect that they are present. Conrath [1981] detected a large scale wave structure in Mariner

9 IRIS data at the 0.5-1 mb level at 65°N (suggesting a vertically propagating wave) however the asynoptic nature of the data did not allow a unique identification of the wavenumber and phase speed. Also the data from the Viking IRTM 15 μm channel revealed a large amplitude wave structure at high northern latitudes during the 1977b dust storm, (Martin and Kieffer [1979]). Theoretical models (Webster [1977], Hollingsworth and Barnes [1995]) and GCM simulations (Pollack et al. [1981], Barnes et al. [1993]) have, however, indicated that forced stationary waves may provide and important contribution to the global circulation.

To asses the geographical and temporal variability we must return to theoretical models. Simple linear theory predicts that waves will propagate vertically when the zonal wind is westerly but not too strong. Hence we expect topographically forced stationary waves to be vertically trapped in mid-latitudes during summer and vertically propagating during winter. In the equinoctial seasons we expect vertical propagation in the mid-latitudes of both hemispheres. In low latitude regions we expect waves to be vertically trapped throughout the year.

Hollingsworth and Barnes [1995] used a linear stationary wave model to predict that zonal wavenumber 2 would prevail in the northern hemisphere on Mars while wavenumber 1 would be prevalent in the southern hemisphere. They also noted asymmetries between eastern and western hemispheres causes by wave interference and that the amplitudes of stationary waves are a strong function of dust loading.

5.5.3 Free Modes

Tillman [1988] has shown that during northern mid-summer ($L_s \simeq 150°$) the Viking Lander surface pressure records show transient bursts of oscillations that are consistent with global scale possibly free modes with periods close to but distinct from one sol and half a sol. A similar burst also occured during the onset of both the 1977b and 1982 dust storms. He proposed that the oscillations were due to the diurnal and semi-diurnal Kelvin modes (Hamilton and Garcia [1986], Zurek [1988]) which can be excited by daily variations in solar heating as they have periods close to a sol and half a sol and are thus nearly resonant. The amplitude of the burst was of the order 10 pa at VL1 and persisted for several sols. Other free modes may also be possible. In a theoretical analysis (Zurek [1988]) has suggested that the most likely type of free mode other than the Kelvin mode is a 4 sol period Rossby wave. The superposition of free modes and other atmospheric circulation patterns may produce winds that are strong enough to induce regional or even global dust storms (see section 5.7.2).

5.5.4 Baroclinic Waves

Baroclinic waves form as a result of a fluid instability in the middle latitudes of both Mars and the Earth. The instability releases potential energy stored in the horizontal temperature gradient and causes small amplitude disturbances to grow exponentially and form waves. On the Earth these waves manifest themselves as mid-latitude weather systems with associated warm and cold fronts.

Theoretical analysis Gadian [1978], Barnes [1984] suggests horizontal wavelengths for the most unstable Martian baroclinic waves in the range 3000 km - 15000 km and phase speeds in the range 10-20 m s^{-1}. These theoretical models do not predict the amplitudes of the waves however. For that we must look to the observations and to GCMs.

Baroclinic waves can be seen in the Viking pressure traces, and in particular in the VL2 pressure. The peak to peak amplitude in pressure associated with the waves is approximately 50 pa and the amplitudes of temperature, wind speed are approximately 10 K, 10 m s^{-1} respectively. Barnes [1980 1981] performed cross spectral analysis of the VL2 meteorological variables and showed them to be baroclinic waves. He also inferred wavenumbers and phase speeds that are similar to those predicted by theory. Other possible observational evidence includes visual images from Mariner 9 which showed front like cloud features and the wave feature seen in Mariner 9 IRIS data (Conrath [1981]).

Baroclinic waves are both geographically and temporally variable. It is evident from the Viking series that they do not occur during the summer months in the northern hemisphere and it is expected on theoretical grounds and from GCM experiments that they do not occur in the southern hemisphere during southern winter. Theory does predict there existence in the southern hemisphere during southern winter although GCM simulations (Barnes et al. [1993]) have suggested that they may be absent, or exist with much reduced amplitude compared to the northern winter baroclinic waves. They are generally confined to mid-latitudes and recently it has been suggested by etal. [1995] that they may be geographically distributed in longitude with greater variance and covariance of variables in low lying regions. Such variability may be particularly important when choosing sites for future lander missions.

One interesting aspect of Martian baroclinic waves is their apparent periodic nature compared to aperiodic or chaotic weather systems on the Earth. Collins and James [1995] produced a simulation of periodic baroclinic waves using a simplified GCM of the Martian atmosphere. They concluded that the periodicity of the wave resulted from the maintenance of a finite amplitude baroclinic wave via a balance between the non-linear advective terms and the dissipation of the wave through radiative cooling, which is rapid in the Martian atmosphere. Zonal wavenumber 3 and 4 waves were seen in many of Collins and James [1995] integrations. More recently Collins et al. [1995] have used both the Oxford and LMD versions of the MGCM to simulate more realistic periodic baroclinic waves and used the statistical method of Singular Systems Analysis to compare in detail the simulated waves with those observed by VL2. They found a competition between a zonal wavenumber 1 mode and zonal wavenumber 2 mode that caused switching between different frequencies of oscillations in the modelled and observed time series. They hypothesised that the frequency of such switching was controlled by the diurnal cycle which supplies a small but finite amplitude perturbation to the baroclinic waves.

The SSA technique turns out to be particularly useful in (a) making a detailed comparison of the model

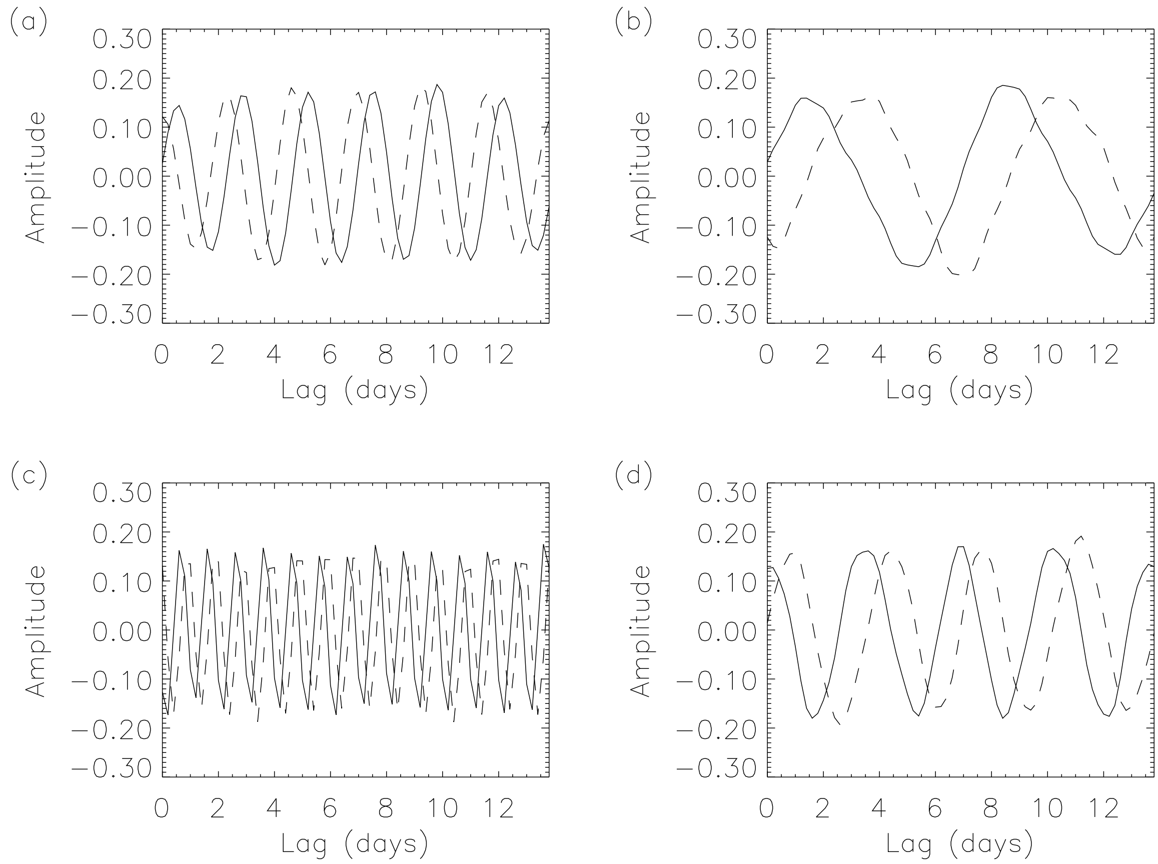

Figure 14: The top 8 eigenvectors from the SSA analysis of the VL2 data. (a) Eigenvector 1 (solid line), Eigenvector 2 (dashed line). (b) Eigenvector 3 (solid line), Eigenvector 4 (dashed line). (c) Eigenvector 5 (solid line), Eigenvector 6 (dashed line). (d) Eigenvector 7 (solid line), Eigenvector 8 (dashed line).

output with the Viking Lander data and (b) in the compression of data via representation in a low dimensional orthonormal basis which is statistically optimal. Figure 14 shows 8 oscillation patterns corresponding to baroclinic waves and the diurnal cycle that have been computed from the VL2 pressure series (for more details see Collins et al. [1995]). These patterns, together with a measure of their amplitude, represent succinctly the major oscillations in the VL2 series and can be used to partially reconstruct the series. For comparison the patterns computed from the Oxford MGCM and the LMD MGCM are show in figures 15 and 16 respectively. The patterns are very similar to those found in the observations (fig. 14(a) and (b)) albeit with some room for improvement in the precise period of the oscillations.

5.5.5 Thermal Tides

Thermal tides are caused by daily variations in solar insolation. The sun heats the surface of the planet which in turn heats the atmosphere via the convective day time boundary layer and cools the atmosphere radiatively at night. Also dust particles in the atmosphere can absorb solar insolation and produce a daily

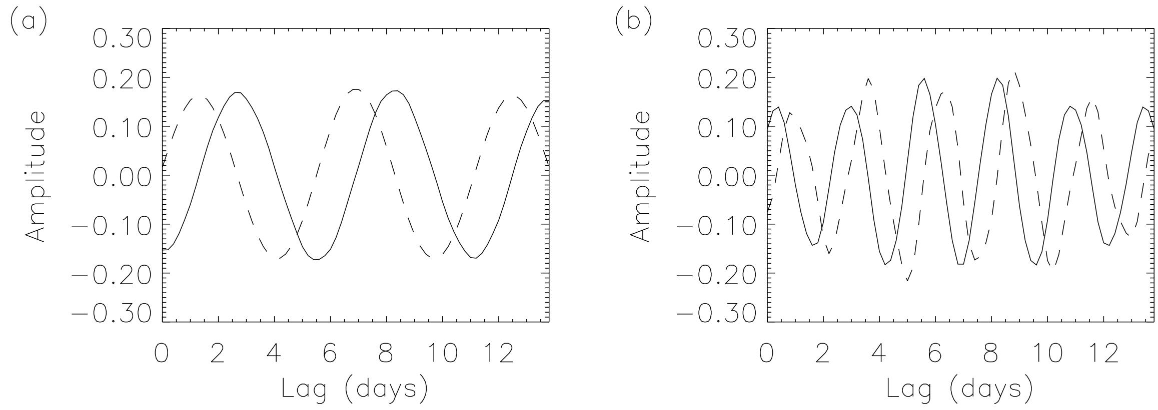

Figure 15: The top 4 eigenvectors computed from the Oxford MGCM. (a) Eigenvector 1 (solid line), Eigenvector 2 (dashed line). (b) Eigenvector 3 (solid line), Eigenvector 4 (dashed line).

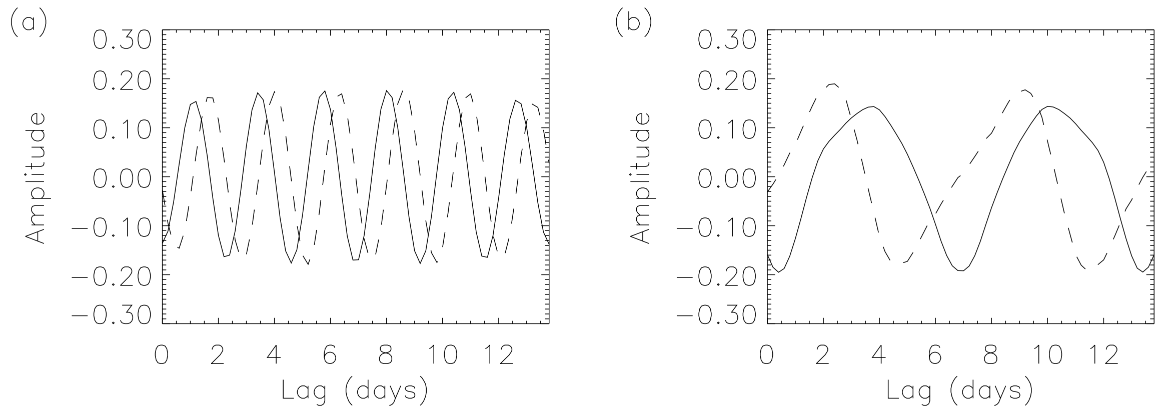

Figure 16: The top 4 eigenvectors computed from the LMD MGCM. (a) Eigenvector 1 (solid line), Eigenvector 2 (dashed line). (b) Eigenvector 3 (solid line), Eigenvector 4 (dashed line).

variation in atmospheric heating. This daily variation in heating can be decomposed into tidal modes Lindzen [1970] to produce a series of waves with frequencies that are integer multiples of 1/sol. By far the largest components of this decomposition in the Martian atmosphere are the diurnal and semi-diurnal tide.

Evidence for thermal tides comes again from the Viking Landers. During their descent phase the landers detected temperature variations consistent with vertically propagating thermal tides and while on the ground they detected diurnal and semi-diurnal oscillations in meteorological variables (Hess et al. [1977], Tillman et al. [1979], Ryan and Henry [1979], Leovy and Zurek [1979], Tillman [1988]). The peak to peak temperature amplitude at VL1 was approximately 20 K and the pressure amplitude was approximately 20 pa during northern summer, that is when the oscillations had their largest amplitude. Other observations come from the Mariner 9 IRIS experiment and the Viking Orbiter IRTM 15μm channel which showed significant daily variations (Conrath et al. [1973], Martin et al. [1979]).

Thermal tides occur in mid-latitudes during the summer months but are virtually ubiquitous throughout the year as one approaches the equator. They are also evident during global dust storms when atmospheric heating via dust absorption rises rapidly. This can be seen in the VL2 pressure series which shows a approximately 50 pa diurnal oscillation in pressure during the 1982 global dust storm. Longitudinal variations in the amplitude of the thermal tide are thought to be significant being caused principally by interactions with the surface topography (Wilson and Hamilton [1995]).

It appears that thermal tides can have a significant effect on zonal mean circulation, especially when the amount of dust in the atmosphere is high. Figure 17 shows the zonal mean zonal wind from a the Oxford MGCM at dust optical depth 2.5. In this case the thermal tides have been suppressed in the model by averaging the insolation over a sol. The season is northern autumn and the pattern of zonal wind shows westerly jets in middle latitudes and weak easterlies in the equatorial belt, a pattern somewhat akin to the annual average zonal wind on the Earth. When the thermal tides are introduced into the model the pattern of zonal wind, shown in fig. 18 is altered radically. At low levels in the equatorial zone a strong westerly jet has formed while at upper levels an easterly jet is evident. At upper levels in middle latitudes the westerly jets 'close off'. The magnitude of the changes is sensitive to the dust amount. Knowledge of such variability in the zonal wind would presumably be important during the decent phase of a lander or during a balloon mission.

5.6 TOPOGRAPHICALLY CONTROLLED FLOWS

The very large amplitude surface topography of Mars exerts a strong influence on the atmospheric circulation on all scales. On the planetary scale, continental scale topographic features give rise to the generation of stationary planetary waves and other large flow features (see Section 5.5.1). On scales around a few hundred kilometres, a range of phenomena are observed which arise from interactions between the large-scale flow,

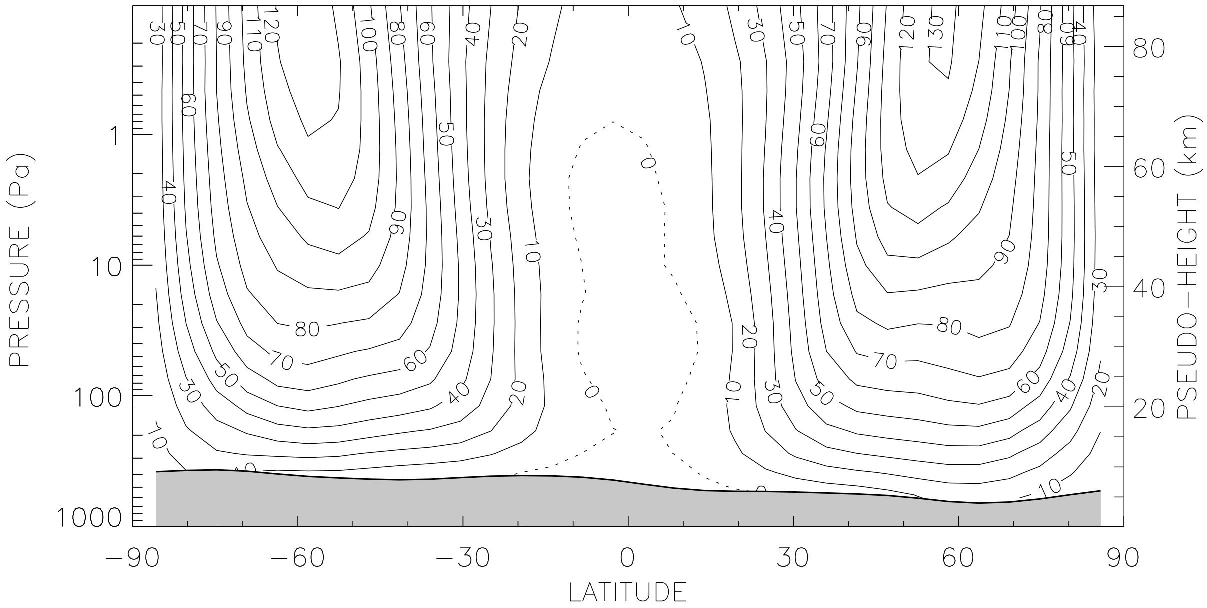

Figure 17: A simulation of zonal mean zonal wind at $\tau = 2.5$ using the Oxford MGCM. The season is northern autumn and the thermal tides have been suppressed.

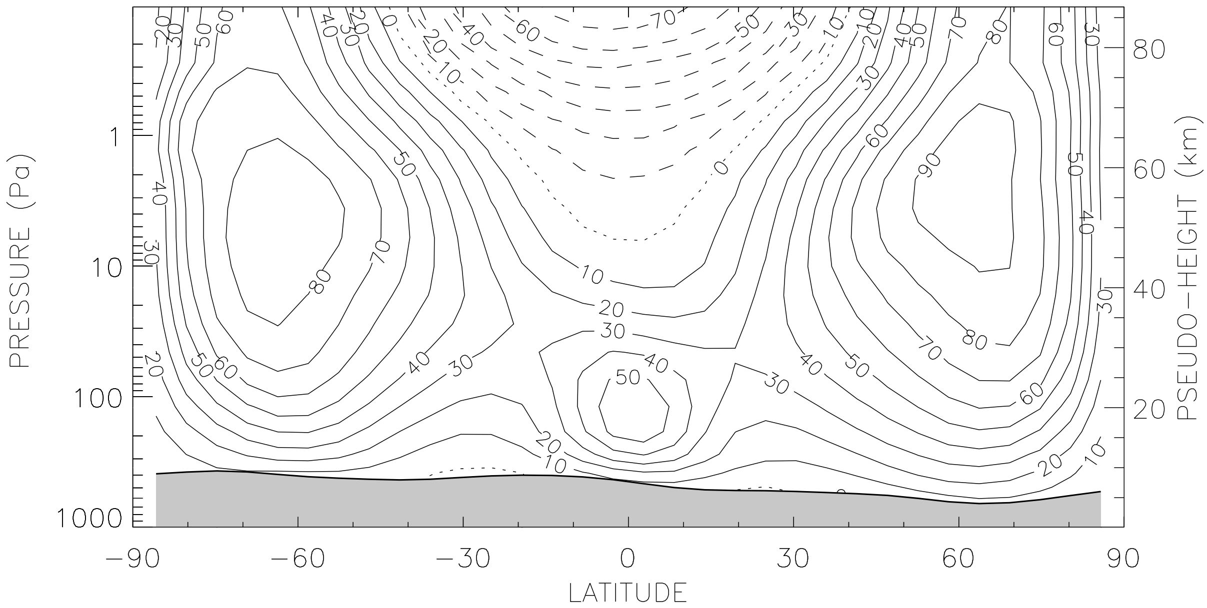

Figure 18: A simulation of zonal mean zonal wind at $\tau = 2.5$ using the Oxford MGCM. The season is northern autumn but in this case the thermal tides have been included.

surface heating and topography, including trapped gravity (or lee) waves, slope winds and low-level jets. In this section we concentrate upon flows controlled by the presence of topography on scales $\sim$ 100 km.

5.6.1 Slope Winds

As found on the Earth, strong heating or cooling of inclined surfaces often leads to the generation of intense local flow in association with progressive density currents [Blumsack 1971], directed either up the slope (for heated surfaces) or down the slope (for night-time cooling). Such anabatic or katabatic drainage flows are largely confined to the boundary layer within a few kilometres of the surface, and vary strongly in their intensity according to the local slope, the time of day, latitude and season. Sources of information on these flows derives partly from direct analysis of the Viking Lander observations of local winds [Hess et al. 1977, Leovy 1982], and from comparison with terrestrial analogues [Stull 1988]. More recently, further information has been obtained from mesoscale model simulations [Ye et al. 1990, Savijarvi and Sili 1993], using methods and parametrization schemes validated against in situ observations both from the Viking landers and from terrestrial field experiments [Savijärvi 1991].

Investigations of the Viking Lander conditions (corresponding to mid-latitude locations with topographic slope $\sim$ 1:600 show generally weaker upslope daytime anabatic flow ($\sim$ 1–2 m s^{-1}) compared with more intense downslope winds ($\sim$ 5 m s^{-1}), peaking around dawn. This is largely because the development of convective activity in the boundary layer strongly mixes momentum in the vertical, which erodes the separate identity of the density current from its surroundings. During the night, however, the convective activity rapidly collapses, and radiative cooling of the underlying surface develops a strongly stratified region close to the surface, within which a strong thermal contrast may develop between air immediately close to the ground and at higher altitudes.

Model studies suggest that the strength of the downslope winds are not strongly sensitive to the length of the slope, but more sensitive to the magnitude of the slope itself. Over steeper slopes ($\sim$ 1:200, such as may be found, for example, near the Arsia Mons site near the equator in the southern hemisphere, which was considered as part of the ESA Marsnet mission proposal) drainage flows may be as strong as 15-20 m s^{-1} in the lowest few hundred metres or so above the topographic slope during the night. Such wind speeds will effectively be superimposed upon any large-scale flow, leading to the possiblity of enhanced dust storm activity donwstream of such sloped regions.

The rapid growth and collapse of convective activity in the boundary layer around dawn and dusk leads to rapid changes in the local flow, including the formation of low-level nocturnal jets ($\sim$ several m s^{-1}; see Section 5.3) and strong vertical wind shear around these times of day. Coriolis accelerations associated with the planetary rotation may also act at mid-high latitudes to deflect the slope wind flow to generate significant flow parallel to the topographic height contours. This may act to reduce the intensity of the drainage flow itself. Thus, for a given topographic slope and no background flow, the most intense drainage flows are expected to occur around latitudes 25–35° [Savijarvi and Sili 1993].

5.6.2 Western Boundary Currents

Another type of strong mesoscale topographically-steered flow also arises because of the underlying planetary rotation, in association with steep, eastward-facing flanks of major topographic features such as the Tharsis Plateau and Arabia. Large-scale circulation patterns driven by the planetary-scale differential heating and condensation flows are modified in the presence of such topography to form concentrated jets which are analogous to the intense western boundary currents, found in the Earth's oceans flowing along their western coasts. In the oceans, these currents carry much of the poleward oceanic heat and mass transport, and are strong sources of instability and eddy formation. In the Earth's atmosphere, a similar phenomenon is observed in association with the Asian monsoon circulation, in which the equator-crossing branch of the circulation forms a concentrated jet in the mid-troposphere which flows adjacent to the uplands along the Horn of Africa [Anderson 1976].

Evidence for such features on Mars derive partly from GCM studies [Joshi et al. 1994 1995] but also from the observed distribution and alignment of bright depositional wind streaks, wave clouds and wind measurements from the Viking Landers [Greely et al. 1992 1993, Joshi et al. 1995]. The strongest examples of these features occur near the equator along the eastern flanks of the Tharsis Plateau and the Arabia/Syrtis uplands around the solstices, when the large-scale meridional circulation in the tropics is dominated by a single equator-crossing Hadley cell. In these conditions, model simulations suggest that the western boundary current flow may take the form of a strong jet, about 500 km wide, which may be as strong as 20 m s^{-1} within the lowest 5–10 km of the atmosphere.

Diurnal variations (e.g. slope winds) superimpose upon the western boundary current flows, leading to strong fluctuations in the strength and direction of the local flow, depending upon the time of day. The strong local winds arising from this interaction may enhance the occurrence of major dust storms during southern hemisphere summer in various preferred locations [Kahn et al. 1992].

5.6.3 Gravity Waves

Gravity waves are small scale waves that are caused by vertical displacements of air. They have horizontal wavelengths in the range 10–100 km and periods in the range 1 hr–1 sol. On Mars it is thought that gravity waves are principally generated by flow over mountains and other rough topography although the there is also the possibility for generation by other mechanisms, for example in regions of atmospheric convection or by frontal motions.

Figure 19: A nocturnal slope flow from Savijarvi and Sili (1993).

Figure 20: A western boundary current from the Oxford MGCM.

Gravity waves can be trapped in the vertical by layers of relatively high static stability air, in which case they form lee waves or under certain conditions they can propagate in the vertical. In the case of vertically propagating waves, the amplitude of the gravity wave increases as the inverse square root of the density and, under certain conditions, the amplitude can become so large that the waves break irreversibly and exert an acceleration on the mean flow. In the terrestrial mesosphere it has been shown that this force is large enough to decelerate the mean flow by several tens of m s^-1 per day and force the atmosphere far from radiative equilibrium [Holton 1983]. In the upper atmosphere of Mars the effect may also be important [Barnes 1990, Joshi et al. 1995].

Observational evidence for trapped gravity waves exists in the form of Mariner 9 visual images of clouds formed by lee waves downstream of mountains [Briggs and Leovy 1974]. Although there is no direct evidence for vertically-propagating gravity waves, the polar warming phenomenon [Barnes and Hollingworth 1987] is a possible indication of gravity wave breaking in the upper atmosphere.

Most of the published general circulation models of the Martian atmosphere (see Section 7.3.1) do not, as yet, have a parametrisation scheme that represents the effects of breaking gravity waves, though schemes have been implemented in simpler models [Barnes 1990, Joshi et al. 1995]. This is despite the fact that the momentum mixing which results from gravity wave breaking may have a significant effect on the circulation. One major problem in the implementation of such a scheme is the lack of observations against which it may be validated. As part of the current project the effects of breaking gravity waves will be assessed, and a scheme will be implemented in the full European general circulation model.

5.7 DUST AND DUST STORMS

5.7.1 Spatial and temporal distribution

The amount of airborne dust carried by the Martian atmosphere is one of the most variable components of the Martian environment, especially on seasonal and interranual time scale. This amount is usually described in term of dust opacity (vertical optical depth). The years observed by Viking were the best studied. First, the Viking lander camera images were used to compute the visible (0.69 μm) optical depth at the two sites over a period of 1.3 Martian years [Pollack et al. 1977]. The complete data set, shown in Fig. 21, is tabulated in Colburn et al. [1989]. The first year was characterized by the occurence of two planet-encircling storms. In spite of the fact that no such storms was observed during the second Viking years, the “background” dust underwent a strong increase during the northern fall and winter seasons comparable to the first year cycle (except for the peak of the dust storms). Northern spring and summer corresponded to low dust opacity periods with visible optical depths near 0.5. Detailed analysis shows that the optical depth in the morning was usually larger than that in the afternoon due to the condensation of water vapor into atmospheric aerosols at night and their evaporation in midday [Colburn et al. 1989].

Figure 21: Complete set of atmospheric vertical optical depths at 0.67 μm (red) measured by (a) Viking Lander 1 (22.27^{o}N, 47.94^{o}W) and (b) Viking Lander 2 (47.67^{o}N, 225.71^{o}W)

Global dust 9-μm extinction opacities maps have been derived from the Viking IRTM data by Martin and Richardson [1993] [Martin 1986, see also]. This valuable dataset shows that the dust loading was also extremely variable in space (especially in latitude during the global dust storm events). Northern spring and summer were globally low opacity periods, althought many local storms increased the optical depth well above 0.5 ($\sim$ 1.3 at 0.69 μm) locally, especially in the northern mid latitudes. See section 5.7.2 for more details on the distribution and the meteorological aspects of these storms. As expected, lower altitudes regions were more shrouded because of the greater path to the surface.

Other years could be very different.On the one hand, great dust storms such as the one observed by Mariner 9 in 1971 and Viking in 1977 seem to be nusual on Mars [Zurek and Martin 1993]. On the other hand, even the low-opacity periods observed by Viking may not be indicative of how clear the atmosphere can become [Clancy et al. 1990]. For instance, the planet observed by Phobos in 1989 in early northern spring was somewhat clearer than the "clearest" one seen by Viking in 1977-1978 [Chassefiere et al. 1995].

Vertical distribution

Vertical profiles of limb reflectance were obtained from the orbit by the TV cameras on Mariner 9 [Anderson and Leovy 1978] and Viking [Jaquin et al. 1986]. They found that the typical atmospheric column often contains one or more discrete, optically thin, ice like layers, above a lower, continuous dust like haze that extends to the surface. The top of the dust haze varied from $\sim$10 km at high latitudes during the clear periods up to ~70 km at low latitudes during the dust storms. In fact, at these low latitudes, the dust remained visible above 40 km all year long. The increase of the dust level at the beginning of the dust storms was gradual, contrasting with the sudden increase in atmospheric opacity seen at the Viking Landers sites. Further analyses suggest that the dust was well mixed during the dust storm periods, unlike during the clear period when the suspended dust was confined in the lower atmosphere.

Based on the results of a simple sedimentation and vertical mixing model, Conrath [1975] estimated the dust mixing ratio q as a function of the pressure level p :

$$q = q_0 \exp[\nu(1 - p_0/p)] \tag{9}$$

where q_0 and p_0 are the surface value of q and p, and ν a constant that determines the pressure below which the mixing ratio rapidly declines. He showed that the equation was consistent with Mariner 9 IRIS data during the decay of the 1971 global dust storm with $\nu = 0.007$. This equation have been used in many atmospheric models [Pollack et al. 1990, Hourdin et al. 1993, e.g.] with a higher value of ν (0.03) though to be typical of clear conditions.

Recently, observations of the relatively clear atmosphere of the equatorial regions of Mars in 1989 has been obtained by the Phobos spacecraft. Estimation of the vertical profile of the dust volume mixing ratio have been published by Korablev et al. [1993] and Chassefiere et al. [1995].

5.7.2 Dust Storms

Absorption by dust is the largest source of radiative heating in the martian atmosphere (see later dust section for more details) and episodic dust storms alter the thermal structure and circulation of the atmosphere to a remarkable degree over periods as long as 100 sols [Kahn et al. 1992, e.g.]. In addition to a background level of dust which is apparently always present in the martian atmosphere (varying between a minimum in northern summer and a maximum in northern winter near perihelion, Kahn et al. [1992]), the occurance, or otherwise, of regional and global dust storms [Gierasch 1979, Zurek 1982, Martin 1984] is a dominant feature in the variability of the martian climate from year to year. Dust storms can be initiated when the surface wind speeds reach of the order of 30 m/s, or more, and dust is lifted into the atmosphere by saltation of surface particles. The circulation is modified in turn by the modifications to the radiative heating induced by the dust and, under certain circumstances, this process may lead to winds which raise more dust and a resulting growth in the size of the storm [Leovy 1979]. Dust storms are loosely classified by their size and range from small-scale dust devils to local, regional and planet-encircling, global or great dust storms.

Dust devils are the smallest-scale dust storms observed, with widths less than about 250 m and vertical scales of about 2 km [Thomas and J. 1985]. About one hundred were observed from the Viking Orbiters, mostly close to the subsolar point (within 20° latitude) and in the summer afternoons, when surface temperature is highest. Such features are too small to represent directly in the current range of martian models.

Local dust storms (defined as affecting regions up to 10^6 km^2) have been observed in all martian seasons, though they are most common within about 30°–40° of the equator and in the southern hemisphere during summer [Capen 1974, Peterfreund and Kieffer 1979]. Winds were observed exceeding 25 m/s at the Viking Lander 1 site at 1.6 m above the ground during a local dust storm at the site [Ryan and Sharman 1981, James and Evans 1981]. Winds of this magnitude are probably great enough to lift more dust from the surface, where it is present, and to cause the storm to grow. During northern winter large dust clouds are also seen in northern mid-latitudes Kahn et al. [1992], caused by strong winds associated with travelling weather systems.

Global or great dust storms [Gierasch 1979, Zurek 1982, Martin 1984] may cover an entire hemisphere, or the whole planet with dust, mixed up to 40–60 km altitude in the atmosphere [Leovy et al. 1973], presumably by a process of growth and coalescence of local dust storms under appropriate conditions. The opacity of the dust clouds during a global storm is high, reaching an optical depth of at least 5 [Hunt 1979]. The observational record indicates that one, or sometimes, two global dust storms may occur in a martian year, though many years are free of global storms. There were two global storms during the first Viking year, none during the second and third and one during the fourth [Leovy 1985]. The past record of martian observations indicates less global storms than were observed during recent spacecraft missions [Zurek and Martin 1993], though this may partly be as a result of variations in observing conditions. Estimates [Zurek and Martin 1993, Martin and Zurek 1993, Martin and Richardson 1993] place the likelihood of a global dust storm occuring in any one martian year at about one in three, though with a large variance. Irregular occurances of global dust storms may be as a result of the intrinsic interannual variability of the martian climate system, and similar variability may be observed in very simple chaotic models [Ingersoll and Lyons 1993]. If the martian atmosphere does indeed exhibit such sensitivity to its initial conditions then prediction in advance of whether an individual year will have a global dust storm or not is almost impossible even with extremely good atmospheric observations and models; the best that can be hoped for is a realistic variability in a statistical sense between years.

The global storms arise mainly during southern spring and summer. This is the time of greatest insolation; perihelion is at L_s=253°, southern summer solstice at L_s=270°. The increased surface heating near the subsolar point enhances atmospheric convection during the day and strengthens topographic winds (see 5.6). Preferred locations for the initialization of storms are regions in low and subtropical latitudes where there are strong gradients in surface albedo and thermal inertia (see Fig. 5), perhaps regional sources of dust and large eastward facing slopes. The last factor may be related to the possible presence of western boundary currents [Joshi et al. 1995] which result in large winds near the surface slopes and may make it easier, in combination with other effects, for the wind to reach speeds at which saltation of surface particles can occur. Initial expansion and coalescence occurs over a few sols until the planet is encircled over a latitude band after about 10 sols. Modelling studies [Haberle et al. 1982, Murphy et al. 1993, Wilson and Hamilton 1995] find that dust is raised up to high altitudes (order 20–60 km) and then transported latitudinally by the Hadley circulation (see section 5.4.1) which may extend over a larger range in latitude in the presence of large quantities of dust Schneider [1983]. Once the dust has obscured most of one, or both, hemispheres, the dust storm will eventually decay on a timescale of about 50–100 sols. This might be because boundary layer turbulence and low-level winds are suppressed by the increased atmospheric stability as a result of radiative heating with larger quantities of dust [Pollack et al. 1979, Leovy 1979]. Diurnal variations in surface temperature and convection are also reduced when the optical depth of the atmosphere is high and less sunlight reaches the surface.

During a martian year about 0.01 kg/m^2 of dust may be raised by dust storms on average over the planet [Kahn et al. 1992]. Though there is certainly evidence of erosion and deposition during the present epoch [Carr 1981] much of the ancient martian terrain is still preserved. Either dust storms were less frequent in the past, or much of the same dust is transported each year by being recycled from equatorial regions to mid-latitudes by great storms and back by mid-latitude storms [Haberle 1986].

The latest results from the Hubble Space Telescope suggest that at present Mars has a colder atmosphere, and therefore must be less dusty, than at the time of the Viking mission. Unfortunately the observational record is too short to determine the range of long-term variability in martian atmospheric dust between years.

5.7.3 Dust Lifting and deposition

Lifting

When wind blows accross a surface covered by loose particles, kinetic energy is transferred to the surface through shear stress. The minimal threshold friction velocity required to initiate particle motion primarily depends on the particles size, which in turn control the aerodynamic properties of the particles and the interparticle forces. Once the particle is in motion, its path depends on the budget between its weight acting downward and the opposite aerodynamic drag.

On Mars, analytical models [White 1979] and wind tunnel simulations [Greeley et al. 1980 1994] have shown that the size particle moved by lowest winds is about 100 μm in diameter. The threshold friction velocity u^* (see section 5.3 for u^* definition) for such particles is typically of the order of 1.5 m s^{-1}, corresponding to a wind velocity at 1.6 meters of the order of 30 m s^{-1} for a surface roughness like at the Viking Lander 1 site. The 100-μm particles are lifted from the surface at a heigth of some tenths of a centimeter, but as the drag is not sufficient to exceed the weigth, they are carried downwind back to the surface (saltation).

Smaller particles require stronger wind to be lifted, but much lower winds can keep them aloft once lifted. In particular, suspended dust on Mars thought to be of the order of one micron in diameter, requires winds way above the maximum winds observed or predicted on Mars to be lifted ($u^* > 4$ m s^{-1}). This is true for dust that settled on smooth, homogeneous surfaces, however, experiments have shown that micron-sized particles on top of small pebbles can be removed by lower, more realistic, friction velocities [Greeley et al. 1994, $u^* \sim 1.3$ m s^{-1},]. The threshold velocities is also lowered by 25 to 40% when the atmosphere is unstable, as occur during surface heating [White and Greeley 1989].

It is likely that larger, saltating sand grains can dislodge the micron-sized particles to set them into suspension, as it commonly occurs on Earth. Within this context, initiation of entrainment for these particles could start as soon as 100-μm particles are lifted ("impact threshold"), but only if such particles are available. In any case, because of the low Martian pressure, extremely high winds are required to lift dust on Mars. The strong winds measured by the Viking Landers during the second global dust storm (peak gusts of 28 m s^{-1} at 1.6 m) did not reach threshold conditions, but came close: movement did occur in sand piles on the top of the Lander, but no movement was observed to occur on the surface. Stronger wind only occured two years later, during the third winter of Lander 1 observations, when bright dust deposits left by earlier dust storms were eroded and when piles of soil artificially created on the ground were modified and in some case removed [Arvidson et al. 1983], unfortunately, the wind sensor was not operating at that time. All these observations are consistent with the experimental and theoretical analyses described above.

The occurence of frequent dust storms on Mars suggests that dust can be lifted efficiently at least in some places, where regional winds can superimpose upon the general circulation to reach the threshold, or when direct heating of the surface cause dust-devil type events (See sections 5.6 and 5.7.2).

Settling and deposition

The sedimentation velocity of the dust particle can be computed using the well-known Stokes expression, corrected to take into account the fact that because of the low Martian pressure, the dust particles can be smaller than the mean free path of the atmospheric molecules [Rossow 1978]. Sedimentation velocity values have been published by Murphy et al. [1990] for spherical and disk shaped particles. Microns-sized particle sedimentation velocity is typically 0.1 cm s^{-1}.

Other processes than sedimentation can transport dust downward. Eddy mixing, especially in the boundary layer, has to be taken into account. Also, at high latitudes during the polar night, the dust particles might be washed out by the atmospheric CO_2 condensation [Forget et al. 1995].

Near the ground, the flux of particles to the surface depends upon Brownian diffusion, inertial impaction and sedimentation as described by Westphal et al. [1987].

5.8 AERONOMY

Aeronomy refers to the study of non-equilibrium processes which occur most prominently at low atmospheric densities. These can be grouped under three main headings:

(1) processes related to the physical separation and escape of atmospheric constituents;

(2) non-LTE radiative transfer processes (LTE stands for local thermodynamic equilibrium, the condition which applies in general when the populations of molecular energy levels are determined by collisions rather than radiative exchange);

(3) dissociation, ionisation, and photochemistry.

For Mars, the most crucial question at present in the area of atmospheric photochemistry is one of the stability of the carbon dioxide atmosphere itself, against dissociation of the CO_2 by solar ultraviolet radiation. In defiance of calculations based on the best available measurements and theory, the dissociation products CO and O_2 appear to be present only in extremely small amounts and it is necessary to postulate some unidentified, but extremely efficient, recombination mechanism for CO_2. Very rapid vertical mixing, and/or an accelerated recombination rate enhanced by catalysis involving hydrogen peroxide, are possible mechanisms which have been proposed. Measurements, as yet unavailable, of the vertical distributions of water vapour and ozone on Mars may provide the answer.

6 POLAR PROCESSES

6.1 POLAR CAPS AND CO_2 ICE

The most striking time-dependent features on Mars, as observed from Earth, are the seasonal polar caps. They appear as white bright features waxing and waning with a seasonal cycle. These caps are composed of CO_2 frost: during the autumn and winter seasons, the local surface and atmospheric temperatures become cold enough to reach the frost point of CO_2, which condenses and forms CO_2 ice deposits on the surface. The resulting latent heat release is the major energy source during these periods. During the spring and summer seasons in either hemisphere, the seasonal CO_2 cap sublimates back into the atmosphere.

In the current epoch, latitudes as low as 50°, or even 40°, can get covered by CO_2 frost in winter. But the influence of the condensation/sublimation cycle is not restricted to high Martian latitudes: every year, as much as 40% of the atmosphere takes part in the seasonal CO_2 cycle, causing large amplitude seasonal fluctuations in the surface pressure which were measured by the Viking Landers. It also affects the Martian climate by creating a strong planetwide atmospheric circulation called the “condensation flow” described in Section 5.4.2.

A review of the Martian seasonal polar caps and of the related carbon dioxide cycle can be found in James et al. [1992] and Forget [1995]. In this section, we focus on the aspects which are relevant for the current Martian environment. Since the condensation phase of the polar caps differs from the sublimation phase in

Vapor pressure curve:	$\exp(23.102 - 3148.0/T)$	mb	Wasburn (1948)
	$\exp(23.230 - 3167.8/T)$	mb	Fanale et al. (1982)
Latent Heat:	5.9×10^5	J kg^{-1}	
CO_2 ice Specific Heat:	$349 + 4.8T$	J kg^{-1} K^{-1}	over 73-198 K
CO_2 ice density:	$\sim 1769 - T$	kg m^{-3}	over 140-170 K

Table 6: The main thermodynamical properties of CO_2 ice relevant for Mars. T is the temperature in Kelvin.

many aspects (physical processes involved, observations available, etc...), they are treated separately.

6.2 THERMODYNAMICAL PROPERTIES OF CO_2 ICE

Carbon dioxide is a linear, symmetric molecule; the solid is cubic. The principal thermodynamical properties of CO_2 ice relevant for Mars studies are summarized in table 6. The radiative properties of CO_2 ice are reviewed below in section 6.3.2 and 6.4.6.

6.3 CONDENSATION OF THE POLAR CAPS

6.3.1 Observations in the Thermal Infrared

Condensation begins in the autumn, when the polar regions are shrouded in continual darkness during the polar night. Almost all that is known about the condensing polar caps has therefore come from Mariner 9 and Viking thermal infrared observations.

These observations gave surprising results. Scientists predicted almost isothermal polar caps at about 145-148 K, in vapor pressure equilibrium with the atmosphere. The Viking Infrared Thermal mapper (IRTM), which was expected to measure such surfaces temperatures with its 11-μm and 20-μm channels found considerable structure with minimum brightness temperatures far below the CO_2 frost point, often below 135 K [Kieffer et al. 1977]. The location and brightness temperatures of these anomalously cold areas were highly variable, sometimes on time scales of days. They were very common in the northern hemisphere at polar latitudes, in contrast to the southern hemisphere where they were less frequent, especially equatorward of 80°S [Forget and Pollack 1993]. In particular, an exceptionally high frequency of occurrence of extremely low brightness temperatures was reached near the north pole immediately after the first phase of the second global dust storm observed by Viking, a few days after the northern winter solstice. The Mariner 9 IRIS spectrometer polar night observations show that these areas exhibit a complex spectral signature, at least in the northern polar region in late winter (the only period and region for which relevant IRIS spectra are available).

Various hypotheses have been suggested to explain these observations [see Kieffer et al. 1977]. Recently, it has been shown that the infrared emission is in fact reduced because of the infrared radiative properties of the CO_2 snow under specific circumstances linked with the precipitation of CO_2 clouds, as described in the next two sections.

6.3.2 Radiative Properties of CO2 Frost in the Thermal Infrared

Recent accurate laboratory measurements by Hansen [1993] indicate that in the spectral regions on either side of the strong 15μm absorption, the CO_2 ice is extremely transparent. Using such laboratory data, the emissivity of pure CO_2 ice deposits have been estimated using radiative transfer models [Warren et al. 1990, Forget et al. 1995]. These models have showed that Martian CO_2 frost could theoretically have an emissivity much lower than unity in the thermal infrared. At any wavelength the primary variable controlling the radiative transfer properties is the snow grain size: the emissivity strongly increases with grain size. Contamination by dust, and especially water ice, can also strongly affect the emissivity especially near their respective absorption bands.

On Mars, outside the observed anomalously low brightness temperatures areas, and especially in early autumn, late winter and spring where no spectral signatures are detected, the Martian polar cap emissivity is likely to be high [Paige 1985, Forget et al. 1995]. According to the models, this would require very large grain sizes, or, more precisely, spectroscopic path lengths on the orders of centimetres, unless the CO_2 ice layer is thin enough that the ground beneath can radiate through, with a high emissivity.

Can the low brightness temperatures be explained by spatial variations in surface emissivity? The observed spectral features in the IRIS and IRTM data can be reproduced by modeled millimetre sized grains CO_2 snow deposits mixed with small amounts of water or dust (Forget *et al.* 1995). The high spatial and temporal variability of the brightness temperatures suggest a scenario based on the different properties of CO_2 snow originating from the atmosphere and ice formed on the ground, as explained below.

6.3.3 Carbon Dioxide Ice Clouds

Atmospheric CO_2 condensation could occur at most altitudes in high latitudes during the autumn and winter seasons [Pollack et al. 1990]. Theoretically, CO_2 ice particles are likely to form clouds in the polar night atmosphere. However, only limited observational evidence of CO_2 clouds exists. The only direct observation was made at relatively low latitudes by the Mariner 6 and 7 infrared spectrometers. Three limb spectra were interpreted as a reflection from thin CO_2 clouds because of characteristic spikes at 4.26 μm [Kieffer et al. 1976, Herr and Pimentel 1970].

Kieffer et al. [1976] first suggested that CO_2 clouds could create the anomalously low IRTM brightness temperatures, among other possibilities. Pollack et al. [1990] showed that the spatial and temporal variabilities of the modeled atmospheric condensation rate were consistent with those exhibited by the low 20 μm brightness temperatures mapped by the Viking IRTM. The fact that the second Viking dust storm was followed by a period of maximum frequency and intensity of low brightness temperature events is consistent with model results: by its radiative effect, dust strongly increases the atmospheric emissivity, its cooling rate, and thus the atmospheric condensation rate [Pollack et al. 1990]. Model calculations indicate that increasing the dust optical depth from 0 to 5 in the winter polar atmosphere produces a transition from a situation in which almost all the carbon dioxide condenses on the ground to one in which it almost all condenses in the atmosphere. It also seems likely that the dust particles can serve as cloud condensation nuclei, along with H_2O ice particles.

CO_2 ice clouds are expected to affect the infrared emission of the polar caps mainly by scattering the radiation emitted by the surface back to the surface, if their particles are not too small [Hunt 1980, Forget et al. 1995]. Non-precipitating CO_2 clouds, composed of particles smaller than a few micrometres should be transparent in the infrared, whereas precipitating CO_2 clouds with particle radii larger than 10 μm should effectively scatter the infrared radiation. The hypothesis of opaque CO_2 clouds emitting higher in the atmosphere in a colder layer [Paige et al. 1990] seems to be incompatible with the observations [Forget et al. 1995].

As for the CO_2 ice deposits, such clouds are able to produce the observed infrared features if the CO_2 ice particles are mixed with small amounts of water or dust [Forget et al. 1995]. In fact, the signatures of CO_2 ice clouds and deposits are rather similar in that they both depend on the fact that intermediate size CO_2 ice grains can be efficient scatterers at infrared wavelengths, whether they are airborne or on the ground. CO_2 ice deposits, composed of much larger grains or nonporous solid ice having directly condensed on the ground or having undergone frost metamorphism, should have an emissivity close to unity, and, in any case, much higher than that of small CO_2 ice particles originating from atmospheric condensation. On the basis of these results, [Forget et al. 1995] suggested that the low brightness temperatures were likely to be created by CO_2 snow falls, and that both falling snow particles and fresh snow deposits could contribute to create the observed features.

6.3.4 Energy Balance of the Condensing Polar Caps

The amount of CO_2 which condenses in the polar caps is controlled by the energy balance of the Martian polar regions: the total net flux of energy into a region at its boundaries must be equal to the rate at which energy is stored inside the region. Since condensation can occur both in the atmosphere and on the surface, the combined atmosphere plus surface column energy balance equation must be considered. To first order, it is

$$C_{CO_2} = [F_{IR}^{\uparrow} - Adv - Cond - (1-A)F_{solar}^{\downarrow}]/L \tag{10}$$

where C_{CO_2} is the total CO_2 condensation rate (kg m^{-2} s^{-1}); L the latent heat of CO_2 (5.9×10^5 J kg^{-1}); $F_{IR}^{\uparrow}$ the thermal infrared flux of the system toward space; Adv the heating rate due to heat transport by the atmosphere to the system (advection); $Cond$ the subsurface heat conduction flux (positive when the subsurface is warmer than the surface); A is the planetary albedo at solar wavelengths; $F_{solar}^{\downarrow}$ the solar flux at the top of the atmosphere. This last term is of course equal to zero at night; most of the condensation cccurs during polar night.

Infrared emission to space: Under typical conditions (i.e. outside the dust storm period), the thermal infrared flux toward space $F_{IR}^{\uparrow}$ is usually the major term in Eq. 10. $F_{IR}^{\uparrow}$ can be determined from spacecraft observations. In particular, the Viking IRTM observations have been used to determine the seasonal evolutions of $F_{IR}^{\uparrow}$ during the first Viking year for the core regions of the residual cap [Paige and Ingersoll 1985], and more recently for the entire seasonal caps during the polar night seasons [Forget and Pollack 1993]. $F_{IR}^{\uparrow}$ was primarily affected by the low brightness temperatures events described in Section 6.3.1, especially in the northern atmosphere [Forget and Pollack 1993].

Polar caps surface temperatures and thermal emission: When the atmosphere is clear, $F_{IR}^{\uparrow}$ is usually close to the infrared flux emitted by the surface. In models, this flux can be computed as $F_{surf\uparrow} = \epsilon\sigma T_{surf}^4$ (with σ, the Stefan-Boltzmann constant, ϵ the spectrally-averaged emissivity, T_{surf} the surface temperature). In spite of the fact that the cap surface temperatures T_{surf} only depend on the local atmospheric pressure, they are poorly-known because of the large uncertainties in the available Martian topographic data used to derive the surface pressure. This is a serious obstacle to modelling and understanding the physics of the caps. Making a direct estimate of the ground ice temperatures from infrared observations is difficult because of the anomalous brightness temperature observed during the polar night and because of the strong emission of the dust particles warmer than the surface cap when the atmosphere is sunlit. Actual "thermodynamic" ground ice temperatures have been estimated at the pole by Paige and Ingersoll [1985], and more recently mapped for the global polar caps by Forget and Pollack [1993]. Interestingly enough, these temperatures seem to be colder than the expected frost point of CO_2 for the topography of the polar regions, which is usually used in the models. In both hemispheres, there is an apparent systematic decrease of the temperature toward the pole, but the southern polar cap is globally 4 K colder than the northern cap. Near winter solstice, temperatures at the pole are about 145.5 K in the north and 141.5 K in the south, corresponding to pressures of respectively 4.3 mbar and 2.3 mbar.

Atmospheric radiative forcing: $F_{IR}^{\uparrow}$ can be affected by the presence of other aerosols such as airborne water ice or dust, and by the absorption and emission of the gaseous atmosphere in the 15-μm band. In the southern hemisphere, model results [Pollack et al. 1990, Hourdin et al. 1995] and available infrared observations [Martin and Kieffer 1979, Martin 1981, Forget and Pollack 1993] suggest that the winter polar atmosphere is approximately isothermal. Its radiative contribution should thus be negligible. This assumption is not valid for the northern autumn and winter seasons observed by Viking during which two global dust storms occurred. The second storm caused a strong increase in the infrared emission measured by all the IRTM channels, especially in the 9 μm and 11 μm channel. This dust storm warming was particularly strong near the cap edge. It decreased with latitude but was still observable in the polar region [Martin 1981]. The second dust storm, and to a lesser extent the first one , were accompanied by a more durable and particularly intense warming of the upper atmosphere in high northern latitudes, thought to be caused by complex atmospheric dynamical processes [Martin and Kieffer 1979, Jakosky and Martin 1987]. Despite the fact that the clear upper Martian atmosphere only radiates in the the 15 μm gaseous CO_2 band, this polar warming considerably increased the total infrared emission toward space of the polar regions [Forget and Pollack 1993].

Atmospheric heat advection: The strong increase of the infrared emission toward space $F_{IR}^{\uparrow}$ during the dust storms does not imply that more CO_2 condensed during these periods: this increase is nothing more than the observable consequence of a much larger advection of energy toward the pole by the atmosphere. In Eq. 10, the observed increase of $F_{IR}^{\uparrow}$ was certainly correlated with a much larger increase of Adv, causing the CO_2 condensation to decrease or even stop during these periods. The heat advected above the caps during the upper atmosphere polar warming events only directly affects atmospheric levels located above the expected level of condensation but it inhibits the condensation rate indirectly by its radiative effect [Martin 1981]. Theoretical studies conducted with atmospheric general circulation models [Pollack et al. 1990, Hourdin et al. 1995] confirm that the heat advection by the atmosphere Adv plays a fundamental role near the cap edge (up to 20-30 Wm^{-2}), especially for enhanced dust loading. This role is probably much smaller near the center of the seasonal cap (a few Wm^{-2}) , as suggested by the heat budget studies by Paige and Ingersoll [1985].

Subsurface conduction: The subsurface conduction $Cond$ accounts for the energy stored in the subsurface material during the year. Thus, it is positive and non-negligible, especially when the caps start condensing, and where the thermal inertia is high. Actual values of the subsurface thermal inertia are poorly-known below the diurnal skin depth on Mars. This uncertainty must be taken into account when modeling the polar caps [Wood and Paige 1992]. The highest thermal inertia should be found on the water ice north residual cap, where the subsurface conduction could reach 20–30 Wm^{-2} [Paige and Ingersoll 1985]. On the other hand, $Cond$ is probably close to zero on the south residual cap where the temperature is constant all year long. This difference between the North and South caps is important in explaining the polar caps asymmetry [Jakosky and Haberle 1990].

Application to polar cap models: Since Leighton and Murray [1966], many models have been developed to simulate the formation of the Martian polar caps by examining their energy balance [Briggs 1974, Davies et al. 1979, Wood and Paige 1992, James and North 1982, Pollack et al. 1990 1993, Hourdin et al. 1993 1995]. Most recent models are able to reproduce the annual variations in atmospheric pressure measured by the Viking landers, but most studies concluded that it was necessary to use artificially low values for the modelled cap emissivities to account for a condensation rate lower than expected. This confirms that in these models major processes have not yet been taken into account or properly treated (e.g. CO_2 clouds and snow, heat advection during the dust storm, upper atmosphere polar warming) and that the available datasets used for the topography and for the seasonal thermal inertia may not be accurate.

6.3.5 Extension, Mass and Thickness of the Polar Caps

Extension: The locations of the polar caps boundaries during their condensation phases and their maximum extensions are not very well known for several reasons. First, since during the autumn and winter seasons, the Martian poles are by definition tilted away from the Sun, and thus from Earth, and so telescopic observations have been difficult to obtain. Moreover, both spacecraft and telescopic observations in the visible are complicated by the near coincidence of the terminator with the edge of the cap. Nevertheless, Viking observations of the south polar cap [Briggs et al. 1977, James 1983] confirm terrestrial observations that the surface frost extends to between -50° and -55° latitude and reaches as far north as -40° latitude in the relatively low-elevation Hellas and Argyre basins which are covered preferentially by the frost, as expected from energy balance considerations (in low altitude regions, higher pressures correspond to higher frost temperatures and thus more infrared energy is emitted).

In the northern hemisphere, observations of the cap boundaries are even more difficult. These regions are usually obscured by clouds during autumn, winter and early spring to latitudes as low as +40°. These clouds, generally referred to as the "polar hood", have been studied for decades by telescopic observers who were able to distinguish them from the ground ice because of their high variability and their higher opacity in images obtained with blue and violet filters. The polar hood has also been observed in details by Mariner 9 and Viking [Briggs and Leovy 1974, Briggs et al. 1977]. The camera onboard Mariner 9 showed that the hood is diffuse at latitude higher than 60°, but that it exhibits complex wave structures at lower latitudes. A southern polar hood also exists but is much less prevalent than the northern one [James et al. 1979].

Analysis of images of the north polar cap acquired with various filters from Earth [James et al. 1987] and by Viking [James 1979 1982] suggest that the cap extends to roughly 55° in late winter. This is supported by the IRTM data analyzed by Christensen and Zurek [1984].

During the late autumn and winter seasons, the second Viking Lander located at 48°N latitude observed thin surface frost deposits [Jones et al. 1979, Wall 1981]. There has been considerable debate about whether the frost was composed of CO_2 or H_2O ice, although the most recent studies have favored a H_2O ice composition [Hart and Jakosky 1986, Svitek and Murray 1990].

Mass: The mass of the polar caps cannot be observed remotely. Nevertheless, the global amount of CO_2 which gets trapped in the seasonal polar caps can be estimated from the seasonal surface pressure variations measured by the Viking Landers. This is not straightforward, since these variations are not only due to condensation and sublimation of atmospheric carbon dioxide in the polar caps, but are also strongly influenced by internal mass redistribution associated with the atmospheric circulation [Talagrand et al. 1991, Hourdin et al. 1993, Pollack et al. 1993]. For this reason, the surface pressure cycle depends on the location on the planet and is not simply related to the global atmospheric mass cycle. Hourdin et al. [1995] used a global circulation model to estimate the local meteorological component and thus the global atmospheric mass budget from the Viking data, with reasonable accuracy except for the fact that global Martian topography is not very well known. Corresponding model results showed that for a consistent total seasonal cap plus atmospheric carbon dioxide budget of about 6.8 mbar, an equivalent pressure up to 1.0 mbar and 1.7 mbar gets trapped every year in the north and south polar cap respectively.

Thickness: The thickness of the CO_2 ice layer is thought to be highly variable [James et al. 1979]: as explained above, the local condensation and sublimation rate depends on latitude and on the local topography, winds, and surface properties. Wind redistribution is also likely to have a significant effect. Using the Viking IRTM data to determine annual radiation budget and infer the annual carbon dioxide frost budget of the Martian north and south residual cap regions, Paige and Ingersoll [1985] calculated that during the winters observed by Viking, there was about 75 g cm^{-2} of CO_2 frost deposited at the north pole and about 110 g cm^{-2} deposited at the south pole. This corresponds to maximum cap thickness of the order of 0.5 and 0.7 m, respectively, in the fully dense state. Such results are consistent with most polar cap models, including the pioneering works by Leighton and Murray [1966] and more recent and sophisticated models [e.g. Hourdin et al. 1995].

6.4 SUBLIMATION OF THE POLAR CAPS

6.4.1 Recession of the North Polar Cap

In spite of the fact that the north polar cap has not been observed in detail because of the polar hood and orbital constraints, there have been many studies focussing on the shape of the cap during recession and on the latitude of the cap edge. These include spacecraft visual imaging data [James 1979; James 1982], infrared data [Christensen and Zurek 1984] and telescopic data [see, Iwisaki et al. 1982; James et al. 1987; James et al. 1994]. These observations indicate that during its recession, the north polar cap remains roughly circular and centered on the geographic pole. To first order, between L_s=330° and L_s=70° the north polar cap boundary can be fitted by Lat=57.7°+0.216L_s [James, personnal communication 1992]. In fact, the cap edge often "pauses" for at least 60 Martian days at about 65° latitude during mid-spring (from roughly L_s=20° to L_s=50°). Interestingly enough, water ice clouds seem to be absent during the "standstill" but reappear when the recession resumes, suggesting that they are associated with water vapor released at the edge of the cap [James et al. 1987]. By the beginning of the summer, the CO_2 north polar cap completely sublimes, exposing an underlying water ice cap which acts as a source for atmospheric water vapor.

6.4.2 Recession of the South Polar Cap

Since the south pole is tilted toward Earth during favorable oppositions, there are relatively high quality data from terrestrial observations for the subliming south polar cap. Moreover, the 1977 spring and summer south polar cap of Mars was monitored in detail by Viking Orbiter 2 [James et al., 1979] and the 1972 summer cap by Mariner 9.

During the first part of the spring (until $\sim L_s$=240°), the perimeter of the cap is roughly circular and centered on the pole [James et al., 1979]. Between L_s=170° and L_s=240° the south polar cap boundary is well approximated by Lat=-55.5°-0.233(L_s-180) [James, personnal communication 1992]. The cap seems to have an annular structure with a bright periphery surrounding a darker ring, which itself encircles a very bright central area: the residual cap, which can almost be distinguished "through" the seasonal frost. The annular structure seems to persist as the cap recedes, suggesting that resurfacing is involved (see Section 6.4.6 about CO_2 frost albedo). During the second part of the spring, the frost between 160° and 300° longitude rapidly sublimes, leading to a very asymmetric cap which, by southern summer solstice, results in a cap center displaced by 6.5° from the geographic pole. After summer solstice, the cap keeps on shrinking slowly and by midsummer most of the changes are in detail rather than in the area covered by ice.

6.4.3 A CO_2 Ice Residual South Polar Cap

Both Mariner 9 [Paige et al. 1990b] and Viking [Kieffer 1979] thermal infrared observations showed that, at least in 1971 and 1977, carbon dioxide survived all year long on the south residual cap. This behavior is surprisingly different from what has been observed in the north where CO_2 completely sublimes by the beginning of summer. The amount of CO_2 currently stored in the south residual cap is unknown. It is a relatively small area and its thickness has not been estimated. A thickness of 1 to 100 m would correspond to 0.6% to 60% of the current atmospheric mass [Kieffer and Zent 1992]. This thickness could be variable from year to year. Comparison of 1972 (Mariner 9) and 1977 (Viking) images of the summer southern cap shows that the residual cap grew during this period [James 1979]. In fact, there is a possibility that CO_2 ice does not always survive at the south pole during summer. In particular, Earth-based measurements made in 1969 showed a factor of 6 more water during late southern hemisphere summer that was seen by Viking. Jakosky and Barker [1984] suggested that the south cap lost its CO_2 ice coverage exposing an underlying water ice residual cap similar to the northern one.

6.4.4 Microphysical State of the CO_2 Frost

Both thermal infrared [Forget et al. 1995] and near infrared [Calvin and Martin 1994] observations of the Martian polar caps suggest that the spectroscopic "grain sizes" of the spring CO_2 snow could be larger than several centimetres. The seasonal cap in spring may be more like glacier ice containing cracks and bubbles, rather than a snow pack with individual grains [Calvin and Martin 1994]. Such large textural scales have also been found for the N_2 ice deposits on Triton. Eluszkiewicz [1993] has examined the microphysical process involved in frost condensation and metamorphism. On Mars, as on Triton, the atmosphere condenses in the near absence of an inert gas and the frost temperature is nearly constant. Thus no "air bubbles" and no thermal cracking are expected. Over the winter, the Martian CO_2 snow could undergo seasonal densification and sintering into a "nonporous, polycrystalline" layer, provided freshly condensed grains are sufficiently small. Such a layer could be slightly transparent. That could explain why the southern residual cap can be distinguished when the seasonal frost is present.

6.4.5 Energy Balance of the Subliming and Residual Polar Caps

As with the condensation rate, the sublimation rate of the CO_2 ice frost is controlled by the energy balance of the polar regions. However, the sublimation phase is different since it only occurs at the polar cap surface. To first order, Eq. 10 in Section 6.3.4 remains valid, although the subliming rate C_{CO_2} will be negative. The net solar flux $(1 - A)F^{\downarrow}_{solar}$ is of course no longer negligible.

Subsurface heat conduction: During the sublimation phase, the surface CO_2 frost remains at a temperature similar to the autumn and winter temperatures. Not much heat should be left stored in the ground. Thus, the subsurface heat conduction $Cond$ is likely to remain positive and very small on average. [Paige and Ingersoll 1985]. However, it could be non negligible locally near the cap edge when contiguous regions are uncovered and warmed by the sun.

Atmospheric heat advection: The advection Adv has been studied theoretically with atmospheric models which have shown that it should play a much smaller role during the cap recession than during the condensation phase [Pollack et al. 1990; Hourdin et al. 1995].

Insolation: The radiative fluxes during the spring and summer seasons are much stronger than during the winter. Therefore, the mass exchange during the sublimation phase is controlled by the local radiative balance. $F^{\downarrow}_{solar}$ is now the key parameter of this balance. It primarily depends upon the local incidence angle, which in turn depends upon the solar longitude L_s and the latitude (and locally upon the slope). Because of the large eccentricity of the Martian orbit, the maximum flux $F^{\downarrow}_{solar}$ at the south pole at southern summer solstice is 1.5 times higher than at the north pole at northern summer solstice. The planetary albedo A is clearly a crucial parameter of the radiative balance. It is highly variable in space and time and its variations are not very well understood. The frost albedo issue is reviewed in Section 6.4.6.

Atmospheric radiative forcing: Both $(1-A)F^{\downarrow}_{solar}$ and $F^{\uparrow}_{IR}$ may be affected by the presence of dust or water clouds in the spring and summer atmosphere. Airborne dust has a non trivial impact on the sublimation rate at sunlit latitudes. On the one hand, it decreases the amount of solar radiation reaching the surface by scaterring and absorbing at visible wavelengths. On the other hand, it increases the downward infrared fluxes because it raises the atmospheric emissivity and warms the atmosphere by absorbing the solar radiation. In Eq. 10, it raises $F^{\uparrow}_{IR}$, but it is likely to decrease the planetary albedo A if the surface albedo is high enough, as is expected on the polar caps. To first order, these competing radiative effects cancel one another during the spring season, although dust should slightly reduce the total radiative flux at the surface and thus the sublimation rate during the cap recession [Davies 1979; Lindner 1990]. However, Pollack et al. [1990] found that the net effect of enhanced dust loading may be a slight increase of the sublimation rate because it enhances the atmospheric heat transport into the polar cap regions. The impact of water ice clouds is also not simple. Lindner [1990] showed that clouds usually reduce the net radiation flux which strikes the surface except for low solar incidence angle, a common situation at polar latitudes. The cloud could then scatter the solar flux down to the surface and increase the surface illumination.

Energy balance of the residual south polar cap: During the year of Viking and Mariner 9 observations, CO_2 frost was stable at the south residual cap throughout the year, but was not stable at the north residual cap. This difference occurred in spite of the fact that both poles receive the same amount of annual insolation, and despite the higher elevation of the south residual polar cap compared to the northern cap, which should thus be more stable. Most theoretical models simulating the energy balance of the polar caps have been unable to preserve CO_2 ice at the south pole, but still obtain agreement with other observations. Paige and Ingersoll [1985] used the solar reflectance and infrared emission measurements obtained by the Viking IRTM to study the radiative balance of the residual polar cap areas. They calculated the annual radiative budgets and infer the annual CO_2 frost budgets. They confirmed the stability of the CO_2 frost near the south pole and showed that the north-south difference was due to very asymmetric behavior during the spring sublimation phase. The CO_2 sublimation rates were then much smaller in the south than in the north, and this was due to the higher albedo of the south residual cap relative to the north cap. This difference in albedo, added to the difference in subsurface heat conduction — which is rather high on the residual north cap and close to zero on the south residual CO_2 cap where the temperature is constant all year long — [Jakosky and Haberle 1990] explains why the north and south residual polar caps are currently so different.

6.4.6 CO_2 Frost Albedo

The optical properties of pure CO_2 at solar wavelength were reviewed by Warren [1986]. New accurate measurements have been obtained recently by Hansen [1992]. Warren et al. [1990] used a model originally developed for terrestrial snow to study the theoretical behavior of the CO_2 frost albedo. Pure CO_2 frost was calculated to have a high albedo at visible wavelengths, strongly decreasing with grain size (e.g. ~0.8,0.6 and 0.4 for grain radii of 0.1 mm, 0.5 mm and 2.0 mm). Dust contamination should lower the albedo, whereas H_2O ice contamination should only increase it slightly.

Observations have shown that the albedo of the Martian polar caps is characterized by strong spatial and temporal variations. However, spacecraft or telescopic observations of the Martian frost albedo are made difficult by the presence of dust or clouds in the atmosphere. Even small optical depths of dust can significantly lower the planetary albedo over a bright surface [Davies 1979]. Several authors have published measurements of the polar caps reflectivity from telescopic observations [Dollfus 1965; Lumme 1976; Lumme and James 1984; James et al. 1994]. Unfortunately, because of the very limited viewing geometries for the caps as seen from Earth, estimating a reliable albedo suitable for heat balance calculation (i.e. hemispherical albedo) is very difficult and model dependent. Lumme and James's [1984] estimates for the south cap in 1971 gave 0.64 at 360 nm (uv filter) and about 0.79 at 620 nm (red). Observations of the spring north polar cap with the Hubble Space Telescope gave values of 0.12–0.15 at 230–330 nm (uv), 0.34 at 413 nm (violet), 0.47 at 502 nm (green), and 0.73 at 673 nm (red) [James et al. 1994]. Similarly, Viking images were obtained through various filters and only included a limited range of viewing geometry. Photometric estimations for the bright portions of the seasonal polar cap led to albedos of 0.55–0.6 at 590 nm (red) and 0.36–0.38 at 440 nm (violet) [James et al. 1979].

The IRTM instrument onboard the Viking Orbiters made some calibrated, broadband (0.3-3 μm), solar reflectance measurements. The data obtained in the vicinity of both residual caps were studied in detail by Paige and Ingersoll [1985] and Paige [1985]. In particular, they calculated the planetary albedo of these regions and found that it is approximately 25% lower in the north than in the south, and that it strongly varied through the summer, appearing to be nearly a linear function of insolation during this time. This could be due to various processes, such as thermal cracking or dust removing processes enhanced by the insolation [Paige, 1985]. The difference between the south and north spring residual cap albedo is usually attributed to a difference in dust contamination, linked with the seasonal dust cycle [Paige and Ingersoll, 1985]. However, if the albedo is controlled by the insolation, this could be explained by Mars being closer to the sun during the southern spring and summer seasons.

The seasonal south polar cap solar reflectance IRTM data were also discussed by Kieffer [1979] and are currently being reanalyzed by Ono and Paige [1995]. Kieffer [1979] did not calculate hemispherical albedo, but analyzed solar reflectances in term of Lambert albedo (reflectance normalized to that expected from an ideal diffuse white horizontal surface). In early spring, the Lambert albedo was found to decrease from ~ 0.5 near the cap edge to ~ 0.35 at -80° latitude, before raising again in the residual cap area. Here again, a possible explanation for this annular structure could be a coupling between albedo and insolation.

6.4.7 Interannual Variability of the Seasonal Polar Caps

The interannual variations in the observed seasonal polar caps could provide a measure of the degree of interannual variability within the Martian climate cycle. In particular, the CO_2 cycle is coupled with the dust and water ice cycle and both of them are thought to be highly variable from year to year on Mars.

South Polar Cap: James et al. [1987] reviewed the interannual variability of the Martian south polar cap recession for which data from many years are available. Several regressions, particularly the fast 1956 regression, were found to differ significantly from the mean. They explored the possibility of correlations with global dust storms and suggested that regressions associated with early spring storms may be slower than those that are not. However, summer global dust storms did not appear to have any systematic effect. The Mariner 9 and Viking missions permitted a detailed comparison of the summer phase of the south cap in 1972 and 1977 [James et al. 1979]. In spite of the fact that the spring regression curves were very similar [James and Lumme, 1982], the summer cap retreat observed by Viking was slower. The general behavior in 1977 was similar to that seen by Mariner 9, but delayed by several weeks. Several icy regions, including the cap outliers, survived the Viking year but totally sublimed in 1972.

North Polar Cap: In the northern hemisphere, less reliable data are available. Slight interannual differences were reported by Iwisaki et al. [1982] and Parker et al. [1983] but better data are probably needed to fully establish the existence and pattern of interannual fluctuations [James 1979; James et al. 1994].

Seasonal pressure variation: In spite of the theoretical and observational evidence for some interannual variability in the seasonal polar caps, the seasonal pressure variations recorded by the Viking Landers over several Martian years were almost perfectly repeatable [Tillman 1988; Paige and Wood 1992]. In particular, the pressure cycle, and thus the global CO_2 cap mass, was not significantly affected by the two global dust storms of the first Viking year. (The jump in pressure observed by VL2 during its first winter was caused by a dynamical effect related to the second Viking global dust storm; Hourdin et al. 1993.)

This puzzling repeatability suggests that dust and dust storms may not have a strong impact on the global polar energy balance, or, more likely that this impact was not very different during these three years.

Figure 22: The revised COSPAR standard atmosphere.

Except for the fact that no global dust storm occurred during the second Martian year, the "background" airborne dust underwent a strong seasonal cycle comparable to the first year cycle [Colburn et al. 1989]. Another explanation might be that the Martian CO_2 cycle is regulated by feedbacks which are still unknown.

7 MODEL ATMOSPHERES

7.1 THE REVISED COSPAR MODEL

The COSPAR revised model [Seiff 1982] consists of a mean and two extreme (cool-low and warm-high) temperature and density profiles based on measurements taken during the entry of the Viking landers. The extreme profiles are smooth envelopes which cover the range of excursions observed. The temperature and density was measured from about 100 km altitude down to the surface, but the COSPAR model profiles have been extended above this region by using a model [Stewart 1987] which specifies the atmospheric state as a function of latitude, local time of day and solar longitude. For the upper atmosphere, a solar longitude (245°) near where the insolation is maximum provides the warm-high envelope and one near where the insolation is a minimum (65°) provides the cool-low envelope. The COSPAR model profiles are not representative of the martian atmosphere as a whole, being based on observations taken at two points in the northern hemisphere summer, where and when the Viking landers entered the atmosphere, but are at least based on the only *in situ* observations available.

Figure 23: Mars GRAM density profiles with added random perturbations.

7.2 MARS GLOBAL REFERENCE ATMOSPHERE MODEL

The Mars Global Reference Atmosphere Model (Mars-GRAM) (see e.g. Justus and James [1992]) is a model of the temperature, pressure, density, wind speed and wind direction on Mars that is used for science, engineering and educational purposes. The model uses empirical formulas for temperature and pressure that are based on published measurements taken during the Viking and Mariner 9 missions. Winds are deduced via thermal wind balance (see section 5.4.1). It includes representations of seasonal variations, diurnal variations, the CO_2 cycle, tidal motions, mountain waves and regional and global dust storms. The representations however are of incredibly coarse resolution, for example the surface terrain heights are stored on a 10°latitude by 20 °longitude grid and are represented by only two significant figures. Also assumptions such as thermal wind balance, which breaks down as one approaches the equator are suspect. A much better representation of the Martian atmosphere can be obtained using a Global Circulation Model.

7.3 GLOBAL CIRCULATION MODELS

Basic Concept:

Global or general circulation models are a widely used tool in weather forecasting, climate forecasting and meteorological research. The basic idea is to produce a simulation of an atmosphere by solving the partial differential equations (PDEs) that govern the motion of the atmosphere subject to initial and boundary conditions. Although in principal it is possible to solve the equations exactly, there is no computer in the world that is powerful enough to do this. Also the initial conditions i.e. the state of an atmosphere at any particular time and the boundary conditions e.g. the surface albedo, cannot be known exactly. Hence one must approximate the system of PDEs and initial and boundary conditions in order to make the problem tractable. This approximation gives limitations on the performance of a GCM. Such limitations, which afflict all GCMs, are described below.

7.3.1 Limitations

Dynamical formulations:

The motion of and adiabatic, frictionless planetary atmosphere can be described using the Naiver-Stokes equations of fluid motion. When modelling an atmosphere however, it is appropriate to solve an approximate form of these equations namely the primitive equations (see e.g. Holton [1979]). Such an approximation is necessary, for instance, as sound waves which have phase speeds in excess of several hundred ms^{-1} would require the time step over which the model is iterated to be very small. The primitive equations exclude sound waves so the model time step can be lengthened.

Discretisation:

Once one has the primitive equations it is necessary to discretise them onto a grid of points in the horizontal and vertical. This discretisation may be done any number of ways (see e.g. Haltiner and Williams [1979]) but inevitably it introduces errors into the solution of the PDEs. Firstly the equations of motion have many conservation properties e.g. the conservation of angular momentum, whereas many discretisation methods do not carry over these properties into the numerical scheme. (In fact it is interesting to note that both the GCMs proposed for use in this study do have numerical schemes that conserve angular momentum and this has been shown by Hourdin [1989] to be very important when simulating the Martian atmosphere). Secondly the number of points onto which the equations are discretised, or the resolution in both the horizontal and the vertical, will affect the accuracy of the simulation. In general the greater the resolution the greater the accuracy, although there is no reason why this should always be the case. Also there is a trade-off between the resolution and the length of time for which the model is integrated. It is sometimes better to integrate the GCM for a longer period of time, or to run the model many times using different initial conditions (Monte Carlo simulations) than to invest all ones computer resources into the highest spatial resolution.

Parametrisation:

Because the equations of motion are represented on a finite number of grid points there are a number of processes e.g. turbulent eddies generated near the surface, that are not explicitly resolved. However these processes can be important in providing an accurate simulation as there may be a significant transfer of heat or momentum from so called sub-grid scale processes into the resolved scales of the GCM. Also effects such as the heating and cooling of the atmosphere due to radiative processes must be accounted for. Representing such things in a GCM falls under the general heading of parametrisation. Parametrisation schemes are often based on empirical formulas or idealised models and simulations of the terrestrial atmosphere are often very sensitive to the 'tunable parameters' that such schemes present. The development of parametrisation schemes for Martian GCMs is hampered by the lack of observations to fit empirical formulas hence terrestrial formulas are often substituted directly. The development of accurate parametrisation schemes is a severe limitation to successful simulations of the atmospheres of both the Earth and of Mars.

The above gives a summary of the limitations suffered by all GCMs of the Martian atmosphere. All the Martian GCMs in existence are summarised in table 7 and a brief description of each is given below.

7.3.2 The NASA Ames GCM

The development of the NASA Ames GCM can be traced through the papers of Leovy and Mintz [1969], Pollack et al. [1981], Pollack et al. [1990], Haberle et al. [1993], and Barnes et al. [1993]. Based on the two level UCLA GCM it has been continuously developed to its present state in which is used to perform multi-annual simulations at moderate resolution (see table) with sophisticated parametrisation schemes representing most of the major physical processed on Mars (again see table). It has been used in many studies of Martian atmosphere, notably in the ares of the global circulation, baroclinic waves, the CO_2 cycle and also to a certain extent in mission planning. It is the grandfather of Martian GCMs.

7.3.3 The LMD GCM

The development of the LMD GCM started with the work of Hourdin [1992] who modified the radiation scheme from the Earth based LMD GCM to work under Martian conditions. The LMD model was the first self consistent GCM to produce a simulation of an entire year of the Martian atmosphere. It is now frequently integrated for several Martian years at reasonably high resolution (see table). Notable work using the LMD GCM has been on the annual pressure cycle (Hourdin et al. [1993]), the sensitivity of the GCM (Hourdin et al. [1995]) and on baroclinic wave dynamics (Collins et al. [1995]).

GCM	NASA Ames	LMD	Oxford AOPP	GFDL	Euro-MGCM
Dynamics	Grid point, Arakawa and Lamb [1977]	Grid point, Sadourny and Laval [1984]	Spectral, Hoskins and Simmons [1975]	Grid point, Kurihari and Holloway [1967]	Grid Point and Spectral
Horizontal Resolution (lat x long)	$7.5° \times 9°$ and $5° \times 6°$	$7.5° \times 11.25°$ and $3.75° \times 5.625°$	T21, T31, T42	$5° \times 6°$	T31 $3.75° \times 3.75°$
Vertical Coordinate	$\sigma = p/p_*$	σ	σ	hybrid	σ
Vertical Levels	13	15	10 & 20	16 &40	20
Radiation: CO_2	see Pollack et al. [1979]	Hourdin [1992]	Hourdin [1992]	Goody and Belton [1967]	Hourdin [1992]
Radiation: Dust	Pollack et al. [1979]	Pollack et al. [1979]	Pollack et al. [1979]	Haberle et al. [1982]	Pollack et al. [1979]
Dust distribution	fixed	fixed	fixed	fixed	fixed
Condensation Flow	yes	yes	yes	no	yes
Default Orography	Consortium	Consortium	DTM	DTM	DTM
Surface Albedo and Thermal Inertia	Consortium	Consortium + Paige and Keegan [1994] + Paige et al. [1994]	Consortium + Paige and Keegan [1994] + Paige et al. [1994]	Consortium	Consortium + Paige and Keegan [1994] + Paige et al. [1994]
Gravity wave drag	no	no	no	no	yes

Table 7: Summary of current GCMs

7.3.4 The Oxford GCM

The Oxford GCM started with the development of the Simplified GCM (SGCM) jointly at Reading and at Oxford in 1990. The SGCM was essentially a spectral primitive equation solver with linear parametrisations of radiation and friction in the form of Newtonian cooling and Rayleigh friction. The SGCM was used to study western boundary currents (Joshi et al. [1994 1995]) and baroclinic waves (Collins and James [1995]). Towards the end of 1993 the LMD physics package was interface to Reading/Oxford dynamical code to produce the Oxford AOPP GCM. This has now been running for 2 years and has been used to study baroclinic waves (Collins et al. [1994 1995]) and to generate data for use in assimilation studies (Lewis and Read [1994]).

7.3.5 The GFDL GCM

The GFDL Mars model is still currently under development (for instance it lacks a CO_2 condensation/sublimation scheme). It has at its core the GFDL 'Skyhi' model that has been in existence for a number of year and has been used in many studies (e.g. Hamilton et al. [1995]). Wilson and Hamilton [1995] briefly describes the model as presents some plots of the model climatology and some results concerning the diurnal cycle.

8 CONCLUSIONS

This document summarises everything that is currently known about the environment of Mars. In the next stage of the project we will produce a numerical model of the Martian atmosphere which draws on this information to produce a realistic simulation of the atmosphere, and we will use this model to produce a database of statistics of the atmosphere. Please see the model and database user and software requirement documents for more information.

References

D. L. T. Anderson. The loe-level jet as a western boundary current. *Mon. Weather Rev.*, 104:907–921, 1976.

E. M. Anderson and C. B. Leovy. Mariner 9 television limb observations of dust and ice hazes in mars. *J. Atmos. Sci.*, 35:723–734, 1978.

Akio Arakawa and Vivian R. Lamb. Computational design of the basic dynamical processes of the ucla general circulation model. *Methods in Computational Physics*, 17:173–265, 1977.

R. E. Arvidson, E. A. Guinness, H. J. Moore, J. Tillman, and S. D. Wall. Three mars years: Viking lander 1 imaging observations. *Science*, 22:463–468, 1983.

J. R. Barnes. Time spectral analysis of the midlatitude disturbances in the Martian atmosphere. *J. Atmos. Sci.*, 37:2002–2015, 1980.

J. R. Barnes. Linear baroclinic instability in the martian atmosphere. *J. Atmos. Sci.*, 41:1536–1550, 1984.

J. R. Barnes. Possible effect of breaking gravity waves on the circulation of the middle atmosphere of Mars. *J. Geophys. Res.*, 95:1401–1421, 1990.

J. R. Barnes, J. B. Pollack, R. M. Haberle, R. W. Zurek, C. B. Leovy, H Lee, and J. Schaeffer. Mars atmospheric dynamics as simulated by the NASA/Ames general circulation model II. Transient baroclinic eddies. *J. Geophys. Res.*, 98(E2):3125–3148, 1993.

Jeffey R. Barnes and Jeffrey L. Hollingworth. Dynamical modeling of a planetary wave mechanism for a Martian polar warming. *Icarus*, 71:313–334, 1987.

Jeffrey R. Barnes. Midlatitude disturbances in the Martian atmosphere: A second Mars year. *J. Atmos. Sci.*, 38(2):225–234, 1981.

A. K. Blackadar. Boundary-layer wind maxima and their significance for the growth of nocturnal inversions. *Bull. Am. Meteorol. Soc.*, 1957.

S. L. Blumsack. On the effects of topography on planetary atmospheric circulation. *J. Atmos. Sci.*, 28: 1134–1143, 1971.

S. W. Bougher and R. E. Dickinson. Mars, mesosphere and thermosphere. i. global mean heat budget and thermal structure. *J. Geophys. Res.*, 94:7325–7337, 1988.

G. A Briggs. The nature of the residual Martian polar caps. *Icarus*, 23:167–191, 1974.

G. A. Briggs and C. B. Leovy. Mariner 9 observations of the Mars north polar hood. *Bull. Am. Meteorol. Soc.*, 55:278–296, 1974.

Geoffrey Briggs, Kenneth Klaasen, Thomas Thorpe, and John Wellman. Martian dynamical phenomenon during June-November 1976: Viking orbiter imaging results. *J. Geophys. Res.*, 82:4121–4149, 1977.

Wendy M. Calvin and Terry Z. Martin. Spatial variability in the seasonal south polar cap of Mars. *J. Geophys. Res.*, 99(E10cd):21,143–21,152, 1994.

M. H. Campbell and J. Ulrichs. Electrical properties of rocks and their significance for lunar radar observations. *J. Geophys. Res.*, 74:5867–5879, 1969.

C. F. Capen. A martian yellow cloud - july 1971. *Icarus*, 22:345–362, 1974.

C. F. Capen and V. W. Capen. Martian north polar cap, 1962-1968. *Icarus*, 13:100–108, 1970.

M. H. Carr. *The Surface of Mars*. Yale Univ. Press, 1981.

E. Chassefiere, J. E. Blamont, V. A. Krasnopolsky, O. I. Korablev, S. K. Atreya, and R. A. West. Vertical structure and size distributions of Martian aerosols from solar occultation measurements. *Icarus*, 97:46–69, 1992.

E. Chassefiere, P. Drossart, and O. Korablev. Post-Phobos model for the altitude and size distribution of dust in the low Martian atmosphere. *J. Geophys. Res.*, 100:5525–5539, 1995.

E. J. Christensen. Martian topography derived from occultation, radar, spectral , and optical measurements. *J. Geophys. Res.*, 80:2909–2913, 1975.

P. R. Christensen. Regional dust deposites on mars: Physical properties, age and history. *J. Geophys. Res.*, 91:3533–3545, 1986.

P. R. Christensen and H. J. Moore. The Martian surface layer. In *Mars*, pages 686–729, Tucson, AR, 1992. University of Arizona Press, Tucson.

P. R. Christensen and R. W. Zurek. Martian north polar hazes and surface ice: Results from the Viking survey/completion mission. *J. Geophys. Res.*, 89:4587–4596, 1984.

S. F. S. Chun, K. D. Pang, J. A. Cutts, and J. M. Ajello. Photocatalytic oxidation of organic compounds on mars. *Nature*, 274:875–876, 1978.

P. Chylek and G. W. grams. Scattering by nonspherical particles and optical properties of martian dust. *Icarus*, 36:198–203, 1978.

R. T. Clancy and S. W. Lee. A new look at dust and clouds in the mars atmosphere: Analysis of emission-phase-function sequences from global viking irtm observations. *Icarus*, 93:135–158, 1991.

R. T. Clancy, S. W. Lee, G. R. Gladstone, W. W. McMillan, and T. Rousch. A new model for Mars atmospheric dust based upon analysis of ultraviolet through infrared observations from Mariner 9, Viking, and Phobos. *J. Geophys. Res.*, 100:5251–5263, 1995.

R. T. Clancy, D. O. Muhleman, and G. L. Berge. Global changes in the 0-70 km thermal structure of the Mars atmosphere derived from 1975 to 1989 microwave co spectra. *J. Geophys. Res.*, 95:14543–14554, 1990.

D. S. Colburn, J. B. Pollack, and R. M. Haberle. Diurnal variations in optical depth at Mars. *Icarus*, 79: 159–189, 1989.

M. Collins and I. N. James. Regular baroclinic transient waves in a simplified global circulation model of the martian atmosphere. *J. Geophys. Res.*, 100(E7):14421–14432, 1995.

M. Collins, S. R. Lewis, and P. L. Read. Regular and irregular baroclinic waves in a martian general circulation model: A role for diurnal forcing? *Adv. Space. Res.*, 16(6):3–7, 1994.

M. Collins, S. R. Lewis, P. L. Read, and F. Hourdin. Baroclinic wave transitions in the martian atmosphere. Submitted to *Icarus*, 1995.

B. Conrath, R. Curran, R. Hanel, V. Kunde, W. Maguire, J. Pearl, J. Pirraglia, J. Welker, and T. Burke. Atmospheric and surface properties of Mars obtained by infrared spectroscopy on Mariner 9. *J. Geophys. Res.*, 78:4267–4278, 1973.

B. J. Conrath. Thermal structure of the Martian atmosphere during the dissipation of dust storm of 1971. *Icarus*, 24:36–46, 1975.

B. J. Conrath. Planetary-scale wave structure in the martian atmosphere. *Icarus*, 48:246–255, 1981.

D. W. Davies, C. B. Farmer, and D. D. LaPorte. Behavior of volatile in Mars' polar areas : a model incorporating new experimental data. *J. Geophys. Res.*, 82:3815–3822, 1979.

Donald W. Davies. Effect of dust on the heating of mars's surface and atmosphere. *J. Geophys. Res.*, 84: 8289–8293, 1979.

Audouin Dollfuss. Etude de la planète Mars de 1954 à 1958. *Ann. Astrophys*, 28:722–747, 1965.

G. S. Downs, Goldstein R. M., R. R. Green, and E. Reichley. Martian topography and surface properties as seen by radar: The 1971 opposition. *Icarus*, 18:8–21, 1973.

G. S. Downs, P. E. Reichley, and R. R. Green. Radar measurements of martian topography and surface properties: The 1971 and 1973 oppositions. *Icarus*, 26:273–312, 1975.

P. Drossart, J. Rosenqvist, S. Erard, Y. Langevin, J. P. Bibring, and M. Combes. Martian aerosol properties from the *Phobos*/ISM experiment. *Ann. Geophys.*, 9:754–760, 1991.

A. J. Dyer. A review of the flux profile relationships. *Boundary-layer Meteorol.*, pages 363–372, 1974.

Janusz Eluszkiewicz. On the microphysical state of the Martian seasonal caps. *Icarus*, 103:43–48, 1993.

Hollingsworth etal. Storm track paper. Submitted to nature, 1995.

F. Forget. Mars CO_2 ice polar caps. In M. Festou B. Schmitt, C. De Bergh, editor, *Solar system ice*. Kluwer Academic, 1995.

F. Forget and J. B. Pollack. Impact of the CO_2 and H_2O clouds of the Martian polar hood on the polar energy balance. *Bull. Am. Astron. Soc.*, 25:1070, 1993.

François Forget and James B. Pollack. Thermal infrared observations of the Martian polar caps : CO_2 ice temperatures and energy budget. Submitted to J. Geophys. Res., 1995.

François Forget, James B. Pollack, and Gary B. Hansen. Low brightness temperatures of Martian polar caps : CO_2 clouds or low spectral emissivity ? In press (*J. Geophys. Res*), 1995.

A. M. Gadian. The dynamics of and the heat transfer by baroclinic eddies and large-scale stationnary topographically forced long waves in the Martian atmosphere. *Icarus*, 33:454–465, 1978.

P. J. Gierasch. Martian dust storms. *Rev. Geophys.*, 12:730–734, 1979.

P. J. Gierasch and R. M. Goody. A study of the thermal and dynamical structure of the Martian lower atmosphere. *Planet. Space Sci.*, 16:615–646, 1968.

R. M. Goody and M. J. S. Belton. Radiative relaxation times for mars. *Planet. Space Sci.*, 15:247–256, 1967.

R. Greeley, M. Lacchia, B. White, R. Leach, D. Trilling, and J. Pollack. Dust on Mars: new values for wind threshold. In *XXV Lunar Planet. Sci. Conf.*, pages 467–468, 1994.

R. Greeley, R. Leach, B. R. White, J. Inversen, and J. B. Pollack. Threshold windspeeds for sand on mars: Wind tunnel simulations. *Geophys. Res. Lett.*, 7:121–124, 1980.

R. Greely, N. Lancaster, S. Lee, and P. Thomas. *Martian aeolian processes, sediments and features.* Univ. Arizona Press, 1992. In Mars, H. H. Kieffer et al. eds.

R. Greely, A. Skypeck, and J. B. Pollack. Martian aeolian reatures and deposits: Comparisons with general circulation models. *J. Geophys. Res.*, 98:3183–3196, 1993.

R. M. Haberle. The climate of mars. *Scientific American*, 254:54–62, 1986.

R. M. Haberle and B. M. Jakosky. Atmospheric effects on the remote determination of thermal inertia of Mars. *Icarus*, 90:187–204, 1991.

R. M. Haberle, C. B. Leovy, and J. B. Pollack. A numerical model of the martian polar cap winds. *Icarus*, 39:151–183, 1979.

R.M. Haberle, H. C. Houben, R. Hertenstein, and Herdtle T. A boundary layer model for Mars : comparison with Viking Lander and entry data. *J. Atmos. Sci.*, 50(11):1544–1559, 1993.

Robert M. Haberle, Conway B. Leovy, and J. B. Pollack. Some effects of global dust storms on the atmospheric circulation of Mars. *Icarus*, 50:322–367, 1982.

Robert M. Haberle, J. B. Pollack, J. R. Barnes, R. W. Zurek, C. B. Leovy, J. R. Murphy, H. Lee, and J. Schaeffer. Mars atmospheric dynamics as simulated by the NASA/Ames general circulation model I. the zonal-mean circulation. *J. Geophys. Res.*, 98(E2):3093–3124, 1993.

G.J. Haltiner and R.T. Williams. *Numerical prediction and dynamical meteorology.* John Wiley, 1979.

K. Hamilton and R. R. Garcia. Theory and observations of the short-period-normal mode oscillations of the atmosphere. *J. Geophys. Res.*, 91:11867–11875, 1986.

K. Hamilton, R. J. Wilson, J. D. Mahlman, and L. J. Umscheid. 1995. *J. Atmos. Sci.*, 52:5–43, 1995.

R. Hanel, R. Conrath, W. Hovis, V. Kunde, P. Lowman, W. Maguire, J. Pearl, J. Pirraglia, C. Prabhakara, B. Schlachman, and G. Levin. Investigation of the Martian environment by infrared spectroscopy on Mariner 9. *Icarus*, 17:423–442, 1972.

G. B. Hansen. The spectral absorption of CO_2 ice from 0.18 to 4.8 microns. *Bull. Am. Astron. Soc.*, 24:978, 1992.

G. B. Hansen. The spectral absorption of CO2 ice in the thermal infrared. *Bull. Am. Astron. Soc.*, 25(3): 1034, 1993.

Helen M. Hart and Bruce M. Jakosky. Composition and stability of the condensate observed at the Viking lander 2 site on Mars. *Icarus*, 66:134–142, 1986.

K. C. Herr and G. C. Pimentel. Evidence for solid carbon dioxide in the upper atmosphere of Mars. *Science*, 166:496–499, 1970.

S. L. Hess, R. M. Henry, C. B. Leovy, J. A. Ryan, and J. E. Tillman. Meteorological results from the surface of Mars: Viking 1 and 2. *J. Geophys. Res.*, 82:4559–4574, 1977.

J. L. Hollingsworth and J. R. Barnes. Forced, stationary planetary waves in mars' winter atmosphere. *J. Atmos. Sci.*, 99:999–999, 1995.

J. R. Holton. The influence of gravity wave breaking on the general circulation of the middle atmosphere. *J. Atmos. Sci.*, 40:791–799, 1983.

James R. Holton. *An introduction to dynamic meteorology*, volume 23 of *Internal geophysics series*. Academic Press, second edition, 1979.

B. J. Hoskins and A. J. Simmons. A multi-layer spectral model and the semi-implicit method. *Q. J. R. Meteorol. Soc.*, 101:637–655, 1975.

F. Hourdin, Phu Le Van, F. Forget, and O. Talagrand. Meteorological variability and the annual surface pressure cycle on Mars. *J. Atmos. Sci.*, 50:3625–3640, 1993.

Frédéric Hourdin. Adaptation du modèle de circulation général du LMD aux conditions Martiennes. stage de DEA "Astrophysique et Téchniques spatiales" Université Paris 7, 1989.

Frédéric Hourdin. A new representation of the CO_2 15μm band for a Martian general circulation model. *J. Geophys. Res.*, 97(E11):18,319–18,335, 1992.

Frédéric Hourdin, François Forget, and Olivier Talagrand. The sensitivity of the Martian surface pressure to various parameters: a comparison between numerical simulations and Viking observations. *J. Geophys. Res.*, 100:5501–5523, 1995.

Frédéric Hourdin and Olivier Talagrand. Superrotation of planetary atmospheres: a numerical study. submitted to J. Atmosph. Sci., 1994.

B. G. Hunt. The influence of the earth's rotation rate on the general circulation of the atmosphere. *J. Atmos. Sci.*, 36:1392–1408, 1979.

G. E. Hunt. On the infrared radiative properties of CO2 ice clouds: Applications to Mars. *Geophys. Res. Lett.*, 7:481–484, 1980.

A. P. Ingersoll and J. R. Lyons. Mars dust storms: Interannual variablity and chaos. *J. Geophys. Res.*, 98 (E6):10951–10961, 1993.

K. Iwisaki, Y. Saito, and T. Akabane. Martian north polar cap : 1979-1980. *J. Geophys. Res.*, 87:10265–10269, 1982.

B. M. Jakosky. The role of seasonal reservoirs in the mars water cycle. ii. coupled models of the regolith, the polar caps, and atmospheric transport. *Icarus*, 55:19–39, 1983.

B. M. Jakosky. The seasonal cycle of water on mars. *Space Sci. Rev.*, 41:131–200, 1985.

B. M. Jakosky and E. S. Barker. Comparison of ground-based and Viking Orbiter measurements of Martian water vapor : variability of the seasonal cycle. *Icarus*, 57:322–334, 1984.

B. M. Jakosky and C. B. Farmer. The seasonal and global behavior of water vapor in the Mars atmosphere: complete global results of the Viking atmospheric vater detector experiment. *J. Geophys. Res.*, 87(B4): 2999–3019, 1982.

B. M. Jakosky and R. M. Haberle. Year-to-year instability of the Mars south polar cap. *J. Geophys. Res.*, 95:1359–1365, 1990.

Bruce M. Jakosky and Robert M Haberle. The seasonal behavior of water on Mars. In *Mars*, page pp. 969. University of Arizona Press, Tucson, 1992.

Bruce M. Jakosky and Terry Z. Martin. Mars: North-polar atmospheric warming during dust storms. *Icarus*, 72:528–534, 1987.

P. B. James. Condensation phase of the Martian south polar cap. *Bull. Am. Astron. Soc.*, 15:846–847, 1983.

P. B. James, R. T. Clancy, S. W. Lee, L. J. Martin, R. B. Singer, Smith E., R. A. Kahn, and R. W. Zurek. Monitoring Mars with the Hubble space telescope : 1990-1991 observations. *Icarus*, 109:79–101, 1994.

P. B. James and N Evans. A local dust storm in the chryse region of mars. *Geophys. Res. Lett.*, 8:903–906, 1981.

P. B. James, H. H. Kieffer, and D. A. Paige. The seasonal cycle of carbon dioxide on Mars. In *Mars*, pages pp. 934–968, Tucson, 1992. University of Arizona Press, Tucson.

P. B. James and G. R. North. The seasonal CO_2 cycle on Mars : An application of an energy balance climate model. *J. Geophys. Res.*, 87:10271–10283, 1982.

Philip B. James. Recession of Martian north polar cap : 1977-1978 Viking observations. *J. Geophys. Res.*, 84:8332–8334, 1979.

Philip B. James. Recession of Martian north polar cap : 1979-1980 Viking observations. *Icarus*, pages 565–569, 1982.

Philip B. James, Geoffrey Briggs, Jeffrey Barnes, and Andrea Spruck. Seasonal recession of Mars' south polar cap as seen by Viking. *J. Geophys. Res.*, 84(B6):2889–2922, 1979.

Philip B. James, Hugh H. Kieffer, and David A. Paige. The seasonal cycle of carbon dioxide on Mars. In *Mars*, pages pp. 934–968. University of Arizona Press, Tucson, 1992.

Philip B. James, Maurice Pierce, and Leonard J. Martin. Martian north polar cap and circumpolar clouds: 1975-1980 Telescopic observation. *Icarus*, 71:306–312, 1987.

F. Jaquin, P. Gierash, and R. Kahn. The vertical structure of limb hazes in the martian atmosphere. *Icarus*, 68:442–461, 1986.

K.L. Jones, R. E. Arvidson, E. A. Guiness, S. L. Braggs, S. D. Wall, C. E. Carlston, and D. G. Pidek. One Mars year : Viking lander imaging observations. *Science*, 204:799–806, 1979.

M. M. Joshi, B. N. Lawrence, and S. R. Lewis. Gravity wave drag in three-dimension atmospheric models of mars. Accepted for publication in JGR, 1995.

M. M. Joshi, S. R. Lewis, P. L. Read, and D. C. Catling. Western boundary currents in the atmosphere of Mars. *Nature*, 367:548–551, 1994.

M. M. Joshi, S. R. Lewis, P. L. Read, and D. C. Catling. Western boundary currents in the atmosphere of Mars. *J. Geophys. Res.*, 999:999–999, 1995.

C. G. Justus and B. James. Additions to mars global reference atmospheric model (mars-gram). Technical Report NASA CR-190212, Grant No. NAG8-877, Final Yech. Report, 29 Apr 1991 - 28 Apr 1992, 1992.

R. A. Kahn, T. Z. Martin, R. W. Zurek, and S. W. Lee. *The Martian dust cycle.* University of Arizona Press, Tucson, Tucson, AR, 1992.

H. H. Kieffer. Mars south polar spring and summer temperatures: a residual co_2 frost. *J. Geophys. Res.*, 84:8263–8288, 1979.

Hugh H. Kieffer, S. C. Chase, E. D. Miner, Frank Don. Palluconi, Guidoa Münch, Gerry Neugebauer, and Terry Z. Martin. Infrared thermal mapping of the martian surface and atmosphere: First results. *Science*, 193:780–786, 1976.

Hugh H. Kieffer, T. Z. Martin, R. Peterfreund, Bruce M. Jakosky, Ellis D. Miner, and Frank Don Palluconi. Thermal and albedo mapping during the Viking primary mission. *J. Geophys. Res.*, 82:4249–4291, 1977.

H. P. Klein. The viking biological experiment on mars. *Icarus*, 34:666–674, 1978.

H. P. Klein. The viking mission and the search for life on mars. *Rev. Geophys. Space. Phys.*, 17:1655–1662, 1979.

O. I. Korablev, V. A. Krasnopolsky, A. V. Rodin, and E. Chassefiere. Vertical structure of the Martian dust measured by the solar infrared occultations from the Phobos spacecraft. *Icarus*, 102:76–87, 1993.

V. A. Krasnopolsky, O. I. Korablev, A. A. Moroz, A. A. Krysko, J. E. Blamont, and E. Chassefiere. Infrared solar occultation sounding of the Martian atmosphere by the Phobos spacecraft. *Icarus*, 94:32–44, 1991.

W. R. Kuhn, S. K. Atreya, and S. E. Postawko. The influence of ozone on Martian atmospheric temperature. *J. Geophys. Res.*, 84(B14):8341–8342, 1979.

Y. Kurihari and J. L. Holloway. Numerical integration of a nine-level primitive equations model formulated by the box model. *Monthly Weather Rev.*, 95:509–530, 1967.

R. R. Leighton and B. C. Murray. Behavior of carbon dioxide and other volatiles on Mars. *Science*, 153: 136–144, 1966.

C. B. Leovy. Martian meteorological variability. *Adv. Space Res.*, 2:19–44, 1982.

C.B. Leovy, R.W. Zurek, and J.B. Pollack. Mechanisms for Mars dust storms. *J. Atmos. Sci.*, 30:749–762, 1973.

Conway Leovy. The general circulation of Mars : Model and observations. *Adv. Geophys*, 28a:327–346, 1985.

Conway Leovy and Yale Mintz. Numerical simulation of the atmospheric circulation and climate of Mars. *J. Atmos. Sci.*, 26:1167–1190, 1969.

Conway B. Leovy. Martian meteorology. *Ann. Rev. Astron. Astrophys.*, 17:387–413, 1979.

Conway B. Leovy and Richard W. Zurek. Thermal tides and Martian dust storms: direct evidence for coupling. *J. Geophys. Res.*, 84(B6):2956–2968, 1979.

S. R. Lewis and P. L. Read. An operational data assimilation scheme for the martian atmosphere. *Adv. Space. Res.*, 16(6):9–13, 1994.

G. F. Lindal, H. B. Hotz, D. N. Sweetnam, Z. Shippony, J. P. Brenkle, G. V. Hartsell, R. T. Spear, and W. H. Micheal. Viking radio occultation measurements of the atmosphere and topography on Mars. *J. Geophys. Res.*, 84:8443–8456, 1979.

B. L. Lindner. The Martian polar cap : radiative effects of ozone, clouds and airborne dust. *J. Geophys. Res.*, 95:1367–1379, 1990.

B. L. Lindner. The hemispherical asymmetry in the Martian polar caps. *J. Geophys. Res.*, 98:3339–3344, 1993.

Richard S. Lindzen. The application and aplicability of terrestrial atmospheric tidal theory to Venus and Mars. *J. Atmos. Sci.*, 27:536–549, 1970.

K Lumme. On the surface brightness and geometric albedo of some Martian areas. *Icarus*, 29:69, 1976.

Kari Lumme and Philip B. James. Some photometric properties of the Martian south polar cap region during the 1971 apparition. *Icarus*, 58:363–376, 1984.

Leonard J. Martin and Richard W. Zurek. An analysis of the history of dust activity on Mars. *J. Geophys. Res.*, 98(E2):3221–3246, 1993.

T. Z. Martin. Mean thermal and albedo behavior of the Mars surface and atmosphere over a Martian year. *Icarus*, 45:427–446, 1981.

T. Z. Martin. Clearing the martian air: The troubled history of dust storms. *Icarus*, 57:317–321, 1984.

Terry Z. Martin. Thermal infrared opacity of the Mars atmosphere. *Icarus*, 66:2–21, 1986.

Terry Z. Martin and Hugh H. Kieffer. Thermal infrared properties of the Martian atmosphere, 2, the 15μm band measurements. *J. Geophys. Res.*, 84(B6):2843–2852, 1979.

Terry Z. Martin, Alan R. Peterfreund, Ellis D. Miner, Hugh H. Kieffer, and Garry E. Hunt. Thermal infrared properties of the Martian atmosphere, 1, global behavior at 7, 9, 11 and 20 μm. *J. Geophys. Res.*, 84: 2381–2842, 1979.

Terry Z. Martin and Mark I. Richardson. New dust opacity mapping from Viking infrared thermal mapper data. *J. Geophys. Res.*, 98(E6):10,941–10,949, 1993.

M. B. McElroy, T. Y. Kong, and Y. L. Yung. Photochemistry and evolution of mars' atmosphere, a viking perspective. *J. Geophys. Res.*, 82:4379–4388, 1977.

D. V. Michelangeli, O. B. Toon, R. M. Haberle, and J. B. Pollack. Numerical simulations of the formation and evolution of water ice clouds in the Martian atmosphere. *Icarus*, 100:261–285, 1993.

H. J. Moore, R. E. Hutton, G. D. Clow, and C. R. Spitzer. Physical properties of the surface materials of the viking lander sites on mars. *U.S. Geol. Survey. Prof. Paper*, 1389:222, 1987.

J. R. Murphy, R. M. Haberle, O. B. Toon, and J.B. Pollack. Martian global dust storms: Zonally symmetric numerical simulations including size dependent particle transport. *J. Geophys. Res.*, 98:2929–2945, 1993.

James R. Murphy, Robert M. Haberle, and James B. Pollack. Numerical simulations of the decay of Martian dust storms. *J. Geophys. Res.*, 95(B9):14,629–14,647, 1990.

J. F. Mustard and J. F. Bell III. New composite reflectance spectra of Mars from 0.4 to 3.14 μm. *Geophys. Res. Lett.*, 21:353–356, 1994.

M.E. Ockert-Bell, J. B. Pollack, and J.F. Bell. Wavelength dependance of the radiative properties of Martian atmospheric dust. *Bull. Am. Astron. Soc.*, 26:1130, 1994.

A.M. Ono and D. A. Paige. Martian polar frosts. Abstract for the "Solar System Ice" international symposium, Toulouse, France, 1995.

J. Oro and G. Holzer. The photolytic degredation and oxidation of organic compounds under simulated martian conditions. *J. Mol. Evol.*, 14:153–160, 1979.

Tobias Owen, K. Biemann, D. R. Rushneck, J. E. Biller, D. W. Howarth, and A. L. Lafleur. The composition of the atmosphere at the surface of Mars. *J. Geophys. Res.*, 82:4635–4639, 1977.

D. A. Paige, J. E. Bachman, and K. D. Keegan. Thermal and albedo mapping of the polar regions of Mars using viking thermal mapper observations 1. North polar region. *J. Geophys. Res.*, 99:25959–25991, 1994.

D. A. Paige and A. P. Ingersoll. Annual heat balance of Martian polar caps: Viking observations. *Science*, 228:1160–1168, 1985.

David A. Paige. The annual heat balance of the Martian polar caps from Viking observations. PhD thesis, Calif. Inst. of Technol., Pasadena, 1985.

David A. Paige, K. E. Herkenhoff, and B. C. Murray. Mariner 9 observations of the south polar cap of Mars : evidence for residual CO_2 frost. *J. Geophys. Res.*, 95(B2):1319–1335, 1990.

David A. Paige and K. D. Keegan. Thermal and albedo mapping of the polar regions of mars : 2. south polar region. *J. Geophys. Res.*, 99:25993–26013, 1994.

David A. Paige and Stephen E. Wood. Modeling the Martian seasonal CO_2 cycle: 2. interannual variability. *Icarus*, 99:15–27, 1992.

F. D. Palluconi and H. H. Kieffer. Thermal inertia mapping of Mars from 60^{o}S to 60^{o}N, volume = 45, year = 1981. *Icarus*, 45:415–426, 1981.

K. D. Pang and J. M. Ajello. Complex refractive index of martian dust: Wavelength dependence and composition. *Icarus*, 30:63–74, 1977.

K. D. Pang, J. M. Ajello, C. W. Hord, and W. S. Egan. Complex refractive index of martian dust: Mariner 9 ultraviolet observations. *Icarus*, 27:55–67, 1976.

Hans A. Panofsky and John A. Dutton. *Atmospheric turbulence*. John Wiley and Sons, New York, 1984.

D. C. Parker, C. F. Capen, and J. D. Beish. Exploring the martian artic. *Sky & Telescope*, 65:218–220, 1983.

Alan R. Peterfreund and Hugh H. Kieffer. Thermal infrared properties of the Martian atmosphere: 3. local dust clouds. *J. Geophys. Res.*, 84(B6):2853–2863, 1979.

L. K. Pleskot and E. D. Miner. Time variability of Martian bolometric albedo. *Icarus*, 50:259–287, 1982.

J. B. Pollack, R. M. Haberle, J. R. Murphy, J. Shaeffer, and H. Lee. Simulation of the general circulation of the Martian atmosphere II: seasonnal pressure variations. *J. Geophys. Res.*, 98(E2):3149–3181, 1993.

J. B. Pollack, M. E. Ockert-Bell, and M. K. Shepard. Viking Lander image analysis of Martian atmospheric dust. *J. Geophys. Res.*, 100:5235–5250, 1995.

James B. Pollack, David Colburn, Ralph Kahn, June Hunter, Van Camp Warren, C. E. Carlston, and M. R. Wolf. Properties of aerosols in the martian atmosphere, as infered from Viking lander imaging data. *J. Geophys. Res.*, 82:4479–4496, 1977.

James B. Pollack, David S. Colburn, F. Michael Flasar, Ralph Kahn, C. E. Carlston, and D. Pidek. Properties and effects of dust particles suspended in the Martian atmosphere. *J. Geophys. Res.*, 84(B6):2929–2945, 1979.

James B. Pollack, Robert M. Haberle, J. Schaeffer, and H. Lee. Simulations of the general circulation of the Martian atmosphere, I, Polar processes. *J. Geophys. Res.*, 95:1447–1473, 1990.

James B. Pollack, Coneway B. Leovy, Paul W. Greiman, and Yale Mintz. A Martian General Circulation Model experiment with large topography. *J. Atmos. Sci.*, 38:3–29, 1981.

J.B. Pollack and Y. L. Yung. Origin and evolution of planetary atmospheres. *Ann. Rev. Earth Plan. Sci.*, 8:425–487, 1980.

William B. Rossow. Cloud microphysics: Analysis of the clouds of Earth, Venus, Mars, and Jupiter. *Icarus*, 36:1,50, 1978.

J. A. Ryan and R. M. Henry. Mars atmospheric phenomena during major dust storms as measured at the surface. *J. Geophys. Res.*, 84:2821–2829, 1979.

J. A. Ryan and R. D. Sharman. Two major dust storms, one mars year appart: Comparisons from viking data. *J. Geophys. Res.*, 86:3247–3254, 1981.

J. A. Ryan, R. D. Sharman, and R. D. Lucich. Mars water vapour, near-surface. *J. Geophys. Res.*, 87: 7279–7284, 1982.

R. Sadourny and K. Laval. January and july performance of the LMD general circulation model. In A.Berger and C.Nicolis, editors, *New perspectives in Climate Modeling*, Elsevier, pages 173–197. Elsevier, Amsterdam, 1984.

Michelle Santee and David Crisp. Thermal structure and dust loading of the Martian atmosphere during late southern summer: Mariner 9 revisited. *J. Geophys. Res.*, 98:3261–3279, 1993.

H. Savijärvi. Radiative fluxes on a dustfree Mars. *Contrib. Atmos. Phys.*, 2:103–112, 1991.

H. Savijarvi and T. Sili. The martian slope winds and the nocturnal pbl jet. *J. Atmos. Sci.*, 50:77–88, 1993.

Hannu Savijärvi. Mars boundary layer modeling : diurnal moisture cycle and soil properties at the Viking lander 1 site. *Icarus*, 117:120–127, 1995.

E. K. Schneider. Martian great dust storms: Interpretive axially symmetric models. *Icarus*, 55:302–331, 1983.

A. Seiff. Post-Viking models for the stucture of the summer atmosphere of Mars. *Adv. Space. Res.*, 2:3–17, 1982.

Alvin Seiff and Donn B. Kirk. Structure of the atmosphere of Mars in summer mid-latitudes. *J. Geophys. Res.*, 82:4364–4378, 1977.

Tero Siili. *Numerical studies of some surface-induced mesoscale phenomena in the Martian atmosphere.* PhD thesis, Helsinki University of Technology, 1994.

Richard A. Simpson, John K. Harmon, Stanley H. Zisk, T. W. Thompson, and Duane O. Muhleman. Radar determination of Mars surface properties. In *Mars*, pages pp. 652–685. University of Arizona Press, Tucson, 1992.

Ian Stewart. Revised time dependent model of the martian atmosphere for use in orbit lifetime and sustenance studies. Technical Report JPL PO NQ-802429, Univ. Colorado, 1987. Final Report.

R. B. Stull. *An Introduction to Boundary Layer Meteorology.* Kluwer Academic, 1988.

Jordan L. Sutton, Conway B. Leovy, and James E. Tillman. Diurnal variations of the Martian surface layer meteorological parameters during the first 45 sols at two Viking lander sites. *J. Atmos. Sci.*, 35:2346–2355, 1978.

Thomas Svitek and Bruce Murray. Winter frost at Viking Lander 2 site. *J. Geophys. Res.*, pages 1495–1510, 1990.

O. Talagrand, F. Hourdin, and F. Forget. The LMD Martian general circulation model: Results about the annual pressure cycle. *Bull. Am. Astron. Soc.*, 23:1217, 1991. Oral presentation at the 23rd annual DPS meeting (Palo Alto, California).

C. H. Tang, T. I. S. Boak III, and M. D. Grossi. Bistatic radar measurements of electrical properities of the martian surface. *J. Geophys. Res.*, 82:4305–4315, 1977.

P. C. Thomas and Gierasch P. J. Dust devils on mars. *Science*, 230:175–177, 1985.

James E. Tillman. Mars global atmospheric oscillations: Annually synchronized transient normal-mode oscillations and the triggering of global dust storms. *J. Geophys. Res.*, 93(D8):9433–9451, 1988.

James E. Tillman, Robert M. Henry, and Seymour L. Hess. Frontal systems during passage of the Martian north polar hood over the Viking lander 2 site prior to the first 1977 dust storm. *J. Geophys. Res.*, 84 (B6):2947–2955, 1979.

James E. Tillman, Lars Landberg, and Soren E. Larsen. The boundary layer of Mars : fluxes stability, turbulent spectra and growth of the mixed layer. *J. Atmos. Sci.*, 51(12):1709–1727, 1994.

O. B. Toon, J. B. Pollack, and C. Sagan. Physical properties of the particles composing the Martian dust storm of 1971-1972. *Icarus*, 30:663–696, 1977.

Stephen D. Wall. Analysis of condensates formed at the Viking 2 lander site : the first winter. *Icarus*, 47: 173–183, 1981.

S. G. Warren. Optical constants of carbon dioxide ice. *Appl. Opt.*, 25:2650–2674, 1986.

S. G. Warren, W. J. Wiscombe, and J. F. Firestone. Spectral albedo and emissivity of CO_2 in Martian polar caps: model results. *J. Geophys. Res.*, 95:717–741, 1990.

P. J. Webster. The low-latitude circulation of mars. *Icarus*, 30:626–649, 1977.

D.L. Westphal, O. B. Toon, and T. N. Carlson. A two-dimensional numerical investigation of the dynamics and mycrophysics of saharian dust storms. *J. Geophys. Res.*, 92:3027–3049, 1987.

B. R. White. Soil transport by winds on mars. *J. Geophys. Res.*, 84:4643–4651, 1979.

B. R. White and R. Greeley. Martian dust threshold measurements: Simulation under heated surface conditions. *LPI tech. Rep.*, 8901:60–61, 1989.

R. J. Wilson and K. Hamilton. Comprehensive model simulations of thermal tides in the martian atmosphere. Submitted to JAS, 1995.

S. E. Wood and D. A. Paige. Modeling the martian seasonal CO_2 cycle: fitting the Viking lander pressure curves. *Icarus*, 99:1–14, 1992.

S. S. C. Wu. A method of defining topographic datums of planetary bodies. *Annales de Geophysique*, 1: 147–160, 1981.

Z. J. Ye, M. Segal, and R. A. Pielke. A comparitive study of daytime thermally induced upslope flow on mars and earth. *J. Atmos. Sci.*, 47:612–628, 1990.

R. W. Zurek. Martian great dust storms: An update. *Icarus*, 50:288–310, 1982.

R. W. Zurek. Free and forced modes in the martian atmosphere. *J. Geophys. Res.*, 93:9452–9462, 1988.

R. W. Zurek, J. R. Barnes, R. M. Haberle, J. B. Pollack, J. E. Tillman, and C. B. Leovy. Dynamics of the atmosphere of Mars. In *Mars*, pages 835–933, Tucson, AR, 1992. University of Arizona Press, Tucson.

Richard W. Zurek and Leonard J. Martin. Interannual variability of planet-encircling dust storms on Mars. *J. Geophys. Res.*, 98(E2):3247–3259, 1993.